



**UNIVERSIDADE FEDERAL DE PERNAMBUCO  
DEPARTAMENTO DE FÍSICA – CCEN  
PROGRAMA DE PÓS-GRADUAÇÃO EM FÍSICA**

## **TESE DE DOUTORADO**

**TRANSIÇÕES DE FASE E TERMODINÂMICA EM SISTEMAS QUASE-  
UNIDIMENSIONAIS DE ROTORES E SPINS QUÂNTICOS**

por

**Antônio Sandoildo Freitas Tenório**

Tese apresentada ao Programa de Pós-Graduação em Física do Departamento de Física da Universidade Federal de Pernambuco como parte dos requisitos para obtenção do título de Doutor em Física.

**Banca Examinadora:**

Maurício Domingues Coutinho Filho (Orientador-UFPE)  
Renê Rodrigues Montenegro Filho (Co-orientador - DF - UFPE)  
Ernesto Carneiro Pessoa Raposo (DF - UFPE)  
Antônio Murilo Santos Macêdo (DF - UFPE)  
Fernando Jorge Sampaio Moraes (DF - UFPB)  
Lindberg Lima Gonçalves (DEMM - UFC)

Recife - PE, Brasil  
Dezembro - 2009

Tenório, Antônio Sandoildo Freitas.

Phase transitions and thermodynamics of quasi-one-dimensional quantum rotor and spin systems / Antônio Sandoildo Freitas Tenório. - Recife : O Autor, 2009.

xix, 134 folhas: il. fig.

Tese (doutorado) - Universidade Federal de Pernambuco. CCEN. Física, 2009.

Inclui bibliografia e apêndice.

1. Magnetismo. 2. Rotores quânticos. 3. Transições de fase (física estatística).

I. Título.

538

CDD (22.ed.)

FQ 2010-001



Universidade Federal de Pernambuco  
Departamento de Física – CCEN  
Programa de Pós-Graduação em Física  
Cidade Universitária - 50670-901 Recife PE Brasil  
Fone (+55 81) 2126-8449/2126-8450 - Fax (+55 81) 3271-0359  
<http://www.df.ufpe.br/pg> e-mail: [posgrad@df.ufpe.br](mailto:posgrad@df.ufpe.br)

---

## Parecer da Banca Examinadora de Defesa de Tese de Doutorado

---

**Antônio Sandoildo Freitas Tenório**

### TRANSIÇÕES DE FASE E TERMODINÂMICA EM SISTEMAS QUASE- UNIDIMENSIONAIS DE ROTORES E SPINS QUÂNTICOS

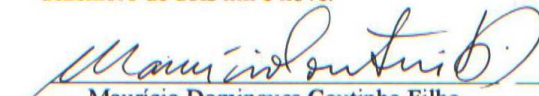
A Banca Examinadora composta pelos Professores Maurício Domingues Coutinho Filho (Presidente e Orientador), Renê Rodrigues Montenegro Filho (Co-orientador), Ernesto Carneiro Pessoa Raposo, Antônio Murilo Santos Macêdo, todos do Departamento de Física da Universidade Federal de Pernambuco, Fernando Jorge Sampaio Moraes, do Departamento de Física da Universidade Federal da Paraíba e Lindberg Lima Gonçalves, do Departamento de Engenharia Metalúrgica e de Materiais da Universidade Federal do Ceará, consideram o candidato:


☒ Aprovado

☐ Reprovado

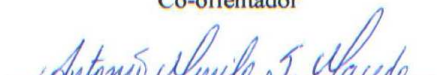
☐ Em exigência

Secretaria do Programa de Pós-Graduação em Física do Departamento de Física do Centro de Ciências Exatas e da Natureza da Universidade Federal de Pernambuco em catorze de dezembro de dois mil e nove.

  
Maurício Domingues Coutinho Filho  
Presidente e Orientador

  
Renê Rodrigues Montenegro Filho  
Co-orientador

  
Ernesto Carneiro Pessoa Raposo

  
Antônio Murilo Santos Macêdo

  
Fernando Jorge Sampaio Moraes

  
Lindberg Lima Gonçalves

## DEDICATION

I Dedicate this dissertation to my wife Maria Barros de Araújo Tenório, for her unwavering support through thick and thin.

To my children Antônio Sandoildo Freitas Tenório Filho, Ana Angélica Barros Tenório, and Maria Catarina Barros Tenório, big-time fans of their old man.

To my grandchildren Laura Natália Freitas Cavalcante Tenório (Lalaka), Marcos Antônio Tenório Ferro (Caquinho) and, last but not least, toddling Maria Eduarda Tenório Guerra Camboim (Duduka). That they never plod their way through life as a banking employee as did their granddaddy, so help me God.

An excerpt I came across in one of Nobel-Prize-winner Knut Hamsun's novels, in a serendipitous reading session, around 1971:

"Es ist nicht leicht sich auf die Menschen zu verstehen und zu erklären, wer klug und wer verrückt ist. Gott bewahre uns alle davor, dass wir durchschaut werden."

Any free translation whatsoever is misleading.

## IN MEMORIAM

José Duarte Tenório (my father),  
Antônia Freitas Tenório (my mother),  
José Samuel Freitas Tenório (my brother), and  
Feliciano Pessoa de Moura (my brother-in-law),  
who left us to be with God.

## ACKNOWLEDGMENTS

First and foremost I am thankful to JESUS, NOSSA SENHORA, SANTA MADRE PAULINA, FREI DAMIÃO, FREI GALVÃO, and my PADRINHO CÍCERO, for everything in this life, good and almost good.

I am deeply grateful to professor Maurício Domingues Coutinho Filho, my supervisor, adviser, friend; a man endowed with great competence and vast knowledge of Physics.

I am grateful from the bottom of my heart to professor René Rodrigues Montenegro Filho, a computer virtuoso besides being a knowledgeable physicist, for his invaluable support, on a daily basis, always a reliable friend, without whom this dissertation would not be.

I am grateful to Fernando Antônio Nóbrega Santos for being helpful whenever needed.

I am grateful to João Liberato de Freitas for his invaluable support.

I am grateful to my lab colleagues Karlla, Fernanda, and Eglânio, for their bits of help, which added up to a lot.

I am grateful to all teachers and employees of Departamento de Física, who somehow have taken part in this project.

I am grateful to my wife and my children, always a source of strength and inspiration that have prodded me along.

To CAPES, CNPq, Finep, and Facepe for the indispensable financial support.

## Abstract

We start by presenting the ground state phase diagram of  $q = 1/2$  quantum-rotor chains with the  $AB_2$  topology and with competing interactions (frustration) calculated through cluster variational mean-field approaches. We consider two interaction patterns, named  $F_1$  and  $F_2$  models, between the quantum-rotor momentum and position operators, which follow exchange patterns of known one-dimensional spin-1/2 systems with a ferrimagnetic state in their phase diagrams. The spin-1/2  $F_1$  model is known as the diamond chain and is experimentally related to the azurite compound, while the spin-1/2  $F_2$  model was recently shown to present a frustration-induced condensation of magnons. We provide a detailed comparison between the quantum-rotor phase diagrams, in single- and multi-site mean-field approaches, and known results for the spin-1/2 models, including exact diagonalization (ED) and density matrix renormalization group (DMRG) data for these systems, as well as phase diagrams of the associated classical models.

Finally, we turn to the thermodynamics of ferrimagnetic alternating spin-1/2 spin-5/2 chains whose study raises great interest both in the theoretical and the experimental fields nowadays. Results concerning the magnetic susceptibility, magnetization and specific heat of two types of chains were obtained through the finite-temperature Lanczos method (FTLM), which were then compared with experimental data as well as theoretical results from semiclassical approaches and spin-wave theories. The ground state is also explored through ED calculations.

Keywords: quantum rotors, spins, magnetism, phase transitions.

## Resumo

Iniciamos com a apresentação do diagrama de fases do estado fundamental de rotores quânticos com  $q = 1/2$  situados em cadeias com topologia  $AB_2$  e dotadas de interações competitivas (frustração). Os resultados são obtidos mediante técnicas de campo médio variacional sobre conjuntos de sítios (*cluster variational mean-field approaches*). Consideramos dois modelos de interação, denominados modelos  $F_1$  e  $F_2$ , entre os operadores de momento e de posição do rotor quântico, os quais seguem padrões de troca de sistemas de spins  $1/2$  conhecidos com um estado ferrimagnético em seus diagramas de fase. O modelo  $F_1$  de spin  $1/2$  é conhecido como cadeia tipo losango (diamond chain) e está experimentalmente relacionado à azurita, enquanto que para o modelo  $F_2$  de spin- $1/2$ , mostrou-se recentemente que este apresenta condensação de mágnons induzida por frustração. Tecemos comparação detalhada entre os diagramas de fase do rotor quântico, nas metodologias de campo médio em um único sítio e em muitos sítios, incluindo dados de diagonalização exata (sigla em inglês: ED) e de grupos de renormalização da matriz de densidade (sigla em inglês: DMRG), e resultados conhecidos para os modelos de spin  $1/2$  como também diagramas de fases de modelos clássicos associados.

Finalmente, tratamos da termodinâmica de duas cadeias ferrimagnéticas alternadas com spins  $1/2$  e  $5/2$ , cujo estudo atualmente tem despertado grande interesse nos campos tanto teóricos como experimentais. Os resultados referentes à susceptibilidade magnética, magnetização e calor específico das cadeias são obtidos através do método de Lanczos para temperaturas finitas (sigla em inglês: FTLM), que são então comparados com os dados experimentais como também com resultados teóricos de metodologias semiclássicas e teorias de ondas de spins. O estado fundamental das



cadeias também é estudado mediante diagonalização exata (sigla em inglês: ED).

Palavras-chave: rotores quânticos, spins, magnetismo, transições de fases.

# Contents

ACKNOWLEDGMENTS . . . . .	v
<b>1 Introduction</b>	<b>2</b>
<b>2 Quantum rotors on the AB<sub>2</sub> chain with competing interactions</b>	<b>4</b>
2.1 Introduction . . . . .	4
2.2 Outline of the theory and methods . . . . .	18
2.3 Quantum rotors on the AB <sub>2</sub> chain: single-site variational mean-field approach on the unit cell . . . . .	22
2.4 Quantum rotors on the AB <sub>2</sub> chain: the double-cell variational mean- field approach . . . . .	36
2.4.1 Frustration F <sub>1</sub> . . . . .	40
2.4.2 Frustration F <sub>2</sub> . . . . .	45
2.5 Summary and conclusions . . . . .	58
<b>3 Ground state and thermodynamics of alternating quantum spin chains</b>	<b>61</b>
3.1 Introduction . . . . .	61
3.2 Theoretical models and methods . . . . .	68

---

3.3	Static properties of an alternating isotropic chain of quantum spins	
	1/2 and classical spins . . . . .	72
3.3.1	Free energy . . . . .	73
3.3.2	Two-spin correlations . . . . .	74
3.3.3	Evaluation of the classical correlations . . . . .	75
3.3.4	Evaluation of correlations comprising quantum spins . . . . .	78
3.3.5	Magnetic susceptibility . . . . .	79
3.4	Alternating spin-1/2 spin-5/2 ferrimagnetic chains - ground state and	
	thermodynamics . . . . .	83
3.4.1	Ground states - ED results . . . . .	83
3.4.2	Thermodynamic quantities . . . . .	89
3.5	Summary and conclusions . . . . .	106
<b>A</b>	<b>Appendix</b>	<b>108</b>
A.1	The Basis of monopole harmonics states . . . . .	108
A.2	Finite-temperature Lanczos method (FTLM) . . . . .	113
A.2.1	Overview . . . . .	113
A.2.2	Adjusting FTLM . . . . .	118
	<b>Bibliography</b>	<b>120</b>

# List of Figures

- 2.1 MF phase diagram of  $\hat{H}'_{rot}$  as a function of the couplings  $J$  and  $K$  at  $MZ = 4$ ,  $g = 1$ , and  $\alpha = 1$ ;  $Z$  is the coordination number of the lattice. Thin lines represent second-order transitions while thick lines are first order. The quantized ferromagnetic phases  $QF_l$  have magnetic moment per site  $l$ ; there is an infinite sequence of such phases for all integer  $l > 0$  at larger values of  $K$ , and only the first two are shown. The phases have the following ground-state expectation values, up to a global  $O(3)$  rotation: gapped quantum paramagnet (GP):  $\langle \hat{L}_\mu \rangle = 0$ ,  $\langle \hat{n}_\mu \rangle = 0$ ; quantized ferromagnet ( $QF_l$ ):  $\langle \hat{L}_z \rangle = l$ ,  $\langle \hat{n}_z \rangle \neq 0$ ;  $\langle \hat{L}_{x,y} \rangle = 0$ ,  $\langle \hat{n}_{x,y} \rangle = 0$ ; Néel ( $N$ ):  $\langle \hat{L}_\mu \rangle = 0$ ,  $\langle \hat{n}_z \rangle \neq 0$ ,  $\langle \hat{n}_{x,y} \rangle = 0$ ; canted ( $C$ ):  $\langle \hat{L}_{x,z} \rangle \neq 0$ ,  $\langle \hat{n}_{x,z} \rangle \neq 0$ ,  $\langle \hat{L}_y \rangle = 0$ ,  $\langle \hat{n}_y \rangle = 0$  (reproduced from Ref. [47]). . . . . 14
- 2.2 Illustration of the QR chains with three rotors per unit cell  $i$ :  $A_i$ ,  $B_{2i-1}$ , and  $B_{2i}$ . Full lines indicate antiferromagnetic exchange couplings ( $J_1 \equiv 1$ ) which give rise to the ferrimagnetic ground state, while dashed lines represent exchange couplings ( $J \geq 0$ ) which frustrate the magnetic order: (a) frustration pattern  $F_1$  and (b) frustration pattern  $F_2$ . . . . . 23

2.3	Frustration $F_1$ . Two-point MF momentum products [(a) $M \equiv 0$ , (c) $M \equiv 1$ ] between the indicated rotors and MF energy curve [(b) $M \equiv 0$ , (d) $M \equiv 1$ ], where we have drawn straight (full) lines to show that at $J = 1$ the system steers away from the linear regime that prevails for $J \leq 1$ and so a phase transition takes place. Full and dashed lines in (a) and (c) indicate the results of the classical vector model. Dashed lines in (b) and (d) are guides to the eye. . . . .	28
2.4	Frustration $F_2$ . Same as in Fig. 2.3. . . . .	29
2.5	Two-point MF momentum products for frustration $F_1$ . Here an inappropriate choice of the parameters $g = \alpha = 1$ and a Hilbert space truncated at $\ell = 1/2$ was made. One cannot make any physical pattern out of the plots. . . . .	30
2.6	Two-point MF momentum products for frustration $F_1$ . Here we show a choice of the parameters $g = \alpha = 1$ with a Hilbert space truncated at $\ell = 6.5$ . The momenta are scaled up to the highest $\ell$ . . . . .	31
2.7	Classical vector configuration. The angle $\theta$ is the unique order parameter. . . . .	34
2.8	Two-point MF momentum products for frustration $F_1$ . Here we show a choice of the parameters $g = \alpha = 1$ with a Hilbert space truncated at $\ell = 5.5$ . $M = 10$ in the frustration coupling and $M = 1$ elsewhere. The system behaves just like the one depicted in Fig. 2.3, but the transition takes place at $J_t \approx 1.8$ , i.e., with a shift to the right hinted at by Eq. (2.38). . . . .	35

2.9	Illustration of the ground states found for the spin-1/2 diamond chain[57] as $J$ is increased from 0. (a) The ferrimagnetic (FERRI) state. (b) The tetramer-dimer (TD) state, where rectangles represent singlet tetramers and ellipses singlet dimers. (c) The dimer-monomer (DM) state. There are two first-order phase transitions: at $J = 0.909$ (FERRI/TD) and $J = 2$ (TD/DM). . . . .	41
2.10	Spin-1/2 diamond chain: ED results for the correlation functions between spins at a central cluster of a system with 28 sites. Dashed lines are guides to the eye. . . . .	42
2.11	Spin-1/2 diamond chain: ED results for the (a) average ground-state energy and (b) rescaled total spin of a system with 28 sites. Phase transitions occur at $J = 0.88$ and $J = 2.0$ , both of first order. Dashed lines are guides to the eye. . . . .	43
2.12	QR momentum correlations calculated by using the double-cell variational MF approach for frustration $F_1$ . One notices the phase sequence $FERRI \leftrightarrow TD \leftrightarrow DM$ , with first-order transitions at $J = 0.68$ and $J = 2$ . Dashed lines are guides to the eye. . . . .	46
2.13	Quantum rotors by using the double-cell variational MF results for frustration $F_1$ : (a) the energy plot ( $E_0 = 1962$ ) shows cusps at the first-order transition points $J = 0.68$ and $J = 2.0$ ; (b) expectation value of the total angular momentum per unit cell. Dashed lines are guides to the eye. . . . .	47

2.14	Quantum rotors with frustration $F_1$ : average singlet density per unit cell for the momenta of the B sites at the same unit cell. One can make out the three phases: FERRI, TD, and DM, as well as pertinent transitions. Dashed lines are guides to the eye. . . . .	48
2.15	QR momentum correlations calculated by using the double-cell variational MF approach for frustration $F_2$ . One can distinguish three major phases: FERRI, CANTED, and the decoupled AF chain ladder system, with transitions occurring around $J = 0.35$ and $J = 0.75$ . Dashed lines are guides to the eye. . . . .	49
2.16	Quantum rotors by using the double-cell variational MF results for frustration $F_2$ : (a) energy and (b) expectation value of the total angular momentum per unit cell. The inset shows details of the phase transition around $J = 0.35$ . Dashed lines are guides to the eye. . . . .	50
2.17	Illustration of the major QR ground states for frustration $F_2$ : (a) FERRI; (b) CANTED; (c) AF, which is composed of two decoupled 1D systems: a linear chain (A sites) and the two-legged ladder (B sites). . . . .	52
2.18	Quantum rotors with frustration $F_2$ : average singlet density per unit cell for the momentum correlations at B sites along the same rung of the ladder. The inset shows details of the phase transition around $J = 0.36$ . . . . .	54

2.19	(a) Pitch angle for the quantum spin-1/2 model calculated through ED, DMRG, and for the minimum energy configuration of the classical vector model with two order parameters: $q$ (pitch angle) and $\theta$ (canting angle). The transition points estimated in Ref. [59] are indicated. (b) Momentum dot products ( $i = 1, 2$ , and $l$ denotes the unit cell) in the minimum energy configuration of the classical vector model. . . . .	57
3.1	Temperature dependence of $\chi_m T$ for the first bimetallic chain (CuMnDTO) [93, 94], where $\chi_m$ is the molar susceptibility and $T$ is the temperature. Squares represent experimental points, and the full line is a plot of Eq. (3.35). A minimum occurs at $T = 130K$ . Reproduced from Seiden[141]. . . . .	66
3.2	Schematic representation of the Hamiltonian and ground-state magnetic order of the (a) sS and (b) ssS alternating chains. In Seiden's paper [141] the larger spin (longer arrow) is a classical quantity, the other one being quantum. . . . .	82
3.3	One-magnon bands of the sS chain. Full lines are spin-wave results from Ref. [143], while dashed lines are guides to the eyes. $S^z = S_G - 1$ for the lower band, while $S^z = S_G + 1$ for the upper one. Inset: Size dependence of the antiferromagnetic gap $\Delta$ , which is estimated to be $\Delta = 4.9046J$ in the thermodynamic limit. . . . .	85



- 3.4 One-magnon bands of the ssS chain with  $J' = 1.7J$ . Dashed lines are guides to the eyes.  $S^z = S_G - 1$  for the lower band, while  $S^z = S_G + 1$  for the upper one. Inset: Size dependence of the antiferromagnetic gap  $\Delta$ , which is estimated to be  $\Delta = 3.88J$  in the thermodynamic limit. . . . . 86
- 3.5 Magnetization per cell  $M$  normalized by its saturation value  $M_{sat} = 3g\mu_B$  as a function of applied magnetic field  $B$  in units of  $J/g\mu_B$  at  $T = 0$  for the sS chain. We have set  $J = 44.8K$  (see Subsection 3.4.2, Fig. 3.10). The first plateau ends at  $b_c = g\mu_B B_c/J \approx 4.9$  which implies that  $B_c \sim 150$  T. On the other hand, the saturation field  $B_S = Jb_S/g\mu_B \sim 200$  T. . . . . 87
- 3.6 Magnetization per cell  $M$  normalized by its saturation value  $M_{sat} = 3.5g\mu_B$  as a function of applied magnetic field  $B$  in units of  $J/g\mu_B$  at  $T = 0$  for the ssS chain with  $J' = 1.7J$  (see Subsection 3.4.2, Fig. 3.11). The first plateau ends at  $b_c = g\mu_B B_c/J \approx 3.9$  which implies that  $B_c \sim 400T$ . On the other hand, the saturation field  $B_S = Jb_S/g\mu_B \sim 600T$ . . . . . 88

- 3.7 Magnetization per mol for the sS chain as a function of the applied magnetic field  $B$  for  $T = 4.2$  K. Experimental data of the compound CuMnDTO from Ref. [94, 141]. FTLM for a system with  $N = 16$ ,  $J = 44.8$  K and  $g = 1.93$ . Quantum paramagnet: fitting of the FTLM data to the magnetization per mol of a quantum paramagnet (Brillouin function) with total spin  $S$ . Taking  $g = 1.93$ , the best fit implying  $S = 15.8$ . The inset serves the purpose of showing how the finite temperature modifies the field-induced Lieb-Mattis ferrimagnetic ground state. . . . . 89
- 3.8 FTLM results for the magnetization normalized by its value at  $T = 0$  ( $M(T = 0) = 1.5$  per cell) for the ssS chain as a function of the normalized applied magnetic field at  $T = 0.1J$ . The system size is  $N = 18$ . Quantum paramagnet: fitting of the FTLM data to the expected curve for a quantum paramagnet (Brillouin function) with total spin  $S$ , the best fit implying  $S = 8.74$ . The inset serves the purpose of showing how the finite temperature modifies the field-induced Lieb-Mattis ground state. . . . . 90
- 3.9 Product of the susceptibility per site  $\chi$  and the temperature  $T$  for the sS chain with  $N = 16$ . In the inset we present the derivative of this curve in the temperature range in which its minimum,  $T_{min} = 2.9J$ , is found. . . . . 92

- 3.10 Product of the molar susceptibility  $\chi_m$  and temperature  $T$  as a function of  $T$  for the sS chain. Experimental data for the compound CuMnDTO from Ref. [141]. Semiclassical susceptibility according to Eq. (3.35):  $J = 59.7$  K,  $S = 2.5$  and  $g = 1.9$ . FTLM results for a system with  $N = 16$ , the best fit to the experimental data implies  $J = 44.8$  K and  $g = 1.90$ . . . . . 93
- 3.11 Product of the susceptibility per site  $\chi$  and the temperature  $T$  for the ssS chain with  $N = 18$ . (a) The numerical data, for the indicated values of  $J'/J$ , are compared with the experimental data for the compound MnNN from Ref. [111] by arbitrarily defining  $J = 100$ K, in order to enhance graph readability. (b)  $\chi T$  for  $J' = 1.7J$  and its derivative, shown in the inset. The minimum of this curve is found at  $T_{min} = 1.7J$ . . . . . 94
- 3.12 Product of the molar susceptibility  $\chi_m$  and temperature  $T$  as a function of  $T$  for the ssS chain. Experimental data of the MnNN compound from Ref. [111]. Semiclassical susceptibility according to Eq. (3.38):  $J = 144$  K,  $J' = 248$  K,  $S = 2.5$  and  $g = 2.0$ . FTLM results for a system with  $N = 18$ , the best fit to the experimental data implies  $J = 150$  K and  $J' = 255$  K, while  $g(= 2.0)$  is not taken as a fitting parameter. . . . . 95
- 3.13 Specific heat per site as a function of temperature  $T$  for sS and the ssS, with  $J' = 1.7J$ , chains. The full lines are the respective Schottky specific heats (Eq. (3.41)). Dashed lines are guides to the eye. . . . 97

- 3.14 Specific heat per site as a function of temperature  $T$  of the sS chain, for various intensities of the applied magnetic field, as indicated. The height position wanders to the right and then back to the left. . . . . 98
- 3.15 (a) Specific heat per site as a function of temperature  $T$  of the sS chains, for various intensities of the applied magnetic field. The full lines represent the respective Schottky specific heat. (b) Schottky  $\delta_B$  (Eq. (3.41)) and chain  $\Delta_B$  gaps as functions of the applied field (Eq. (3.43)). At  $B/(J/g\mu_B) \approx 3.5$ , we find that  $\delta_B \approx \Delta_B$ . . . . . 99
- 3.16 Product of the susceptibility per site  $\chi$  and the temperature  $T$  squared for the ferromagnetically coupled linear chain in the low temperature region,  $T < J$ . Spin-wave result up to second order in  $T/J$  from Ref. [147]. The temperature range  $T < 0.1J$  for which the spin-wave result is almost exact is shown in the inset. The FTLM calculations were made on spin-1/2 ferromagnetic linear chains. . . . . 102
- 3.17 Product of the normalized susceptibility  $\chi$  per unit cell and the temperature  $T$  squared. FTLM data were obtained for the indicated system sizes. The semiclassical result comes from Eq. (3.35). Modified spin-wave results up to second order in  $T/J$  from Ref. [149]. The FTLM result for  $0.5 < \frac{T}{J} < 0.9$  is fitted to a function of the form  $[\frac{5}{3} + a_0(\frac{T}{J})^{\frac{1}{2}} + a_1(\frac{T}{J})]$  and  $a_0$  and  $a_1$  are estimated to be 1.28 and 0.69, respectively. Experimental results were normalized by taking  $J = 59.7$  K ( $g = 1.9$ ) and  $J = 44.8$  K ( $g = 1.85$ ), which must be compared with the semiclassical and FTLM results, respectively. . . . 104

- 3.18 Product of the susceptibility per site  $\chi$  and the temperature  $T$  squared for the sS chain. Inset: Temperature region  $0 < (T/J) < 2$ . Best fit, in the region  $T > 0.8J$ , to a function as  $a_0 + a_1x^{0.5} + a_2x + a_3x^{1.5} + a_4x^2 + a_5x^{2.5}$ , with  $x = T/J$ , implies  $a_0 = 1.73$ ,  $a_1 = 0.12$ ,  $a_2 = -1.83$ ,  $a_3 = 2.40$ ,  $a_4 = -0.65$  and  $a_5 = 0.06$ ; while if the fitting function is  $a_0 + a_1x + a_2x^2 + a_3x^3 + a_4x^4 + a_5x^5$ , the best parameters are  $a_0 = 1.4211$ ,  $a_1 = 0.0289$ ,  $a_2 = 0.4255$ ,  $a_3 = -0.0623$ ,  $a_4 = 0.0046$  and  $a_5 = -0.0001$ . . . . . 105
- A.1 The behavior of the product of the susceptibility per site  $\chi$  and the temperature  $T$  of the ssS chain with  $N = 18$  and  $J = 1.5J'$ . The number of states  $M$  taken in each random sampling is 50 and the total number of random samples  $R$  is indicated in the figure. Each curve is the result of one running of the FTLM algorithm with the indicated parameters, thus there are 10, 5, 2 and 1 runnings in figures (a), (b), (c) and (d), respectively. The precise value of  $\chi T$  for this system size as  $T \rightarrow 0$ ,  $\lim_{T \rightarrow 0} \chi T = 5/3$ , is indicated by the symbol  $\diamond$ . The inset of (a) and (b) show the region near the minimum of the curve, while the inset of (c) and (d) show the region near  $T = 0$ . . . . 119

# Chapter 1

## Introduction

This dissertation is composed of two main chapters where we treat correlated subjects.

In Chapter 2, we present the idea of quantum rotors and their importance in current research. We then study the ground state phase diagram of  $q = 1/2$  quantum-rotor chains with the  $AB_2$  topology and with competing interactions (frustration) calculated through cluster variational mean-field approaches. A detailed comparison is provided which emphasizes the similarities between the quantum-rotor phase diagrams, in single- and multi-site mean-field approaches, and known results for the spin-1/2 models, including exact diagonalization and density matrix renormalization group data for these systems, as well as phase diagrams of the associated classical models. The main results of this chapter were condensed in the article published by Physical Review B [155].

In Chapter 3, we finally turn to the thermodynamics of ferrimagnetic alternating spin-1/2 spin-5/2 chains whose study raises great interest both in the theoretical

and the experimental fields nowadays. We start out with a brief review showing the relevance of the pertinent materials in decades of intensive research in the area of molecular magnetism. Then results concerning the magnetic susceptibility, magnetization and specific heat of two types of chains are obtained through the finite-temperature Lanczos method (FTLM). These are compared with experimental data as well as theoretical results from semiclassical approaches and spin-wave theories. Work is still being done until we have produced material enough that may warrant the submission of a new article on the subject.

In the end of each chapter we present the respective summary and conclusions.

## Chapter 2

# Quantum rotors on the $AB_2$ chain with competing interactions

### 2.1 Introduction

Rotors are tridimensional rigid objects such as a top or a gyroscope (which may have freedom in all three axes) used to explain rotating systems as well as for maintaining and measuring orientation, based on the principles of angular momentum. To determine their orientation in space three angles are required (the Euler angles, for instance). Special among these is the linear rotor, which consists of two point masses located at fixed distances from the center of mass. The object is three-dimensional, but requires only two angles to describe its orientation. The quantum version of this model is a useful point of departure for the study of the rotational transitions of diatomic molecules (zeroth-order model). A more accurate description of the energy of the molecule would accordingly include possible variations in bond length due to rotations or anharmonicity in the potential due to vibrations. As will be seen shortly



below, this model and its ad hoc variations exhibit interesting physics and lends itself admirably to the understanding of sundry other physical systems, far outreaching its basic use for the study of the rotational energy of diatomic molecules.

We now provide a first glimpse of the quantum mechanics of the quantum linear (rigid) rotor (QLR). This is indeed the case of the spherical rotor, where the three components of the moment-of-inertia tensor are equal (a symmetric rotor or top has two equal components and the asymmetric one boasts three different components. The symmetric top can be analytically addressed by using Wigner D-matrices; the asymmetric case does not have an exact solution. The rotational energy depends on the moment of inertia,  $I$ , in the center-of-mass reference frame,

$$I = \mu R^2 \quad (2.1)$$

where  $\mu$  is the reduced mass of the molecule and  $R$  is the distance between the two atoms. In addition to its usefulness, the QLR is a very simple model and one case where the Schrödinger equation can be solved analytically. In a field-free space, the Hamiltonian operator is given in terms of spherical coordinates and reads

$$\hat{H} = \frac{\hbar^2}{2I} \hat{\mathbf{L}}^2 = -\frac{\hbar^2}{2I} \left[ \frac{1}{\sin \theta} \frac{\partial}{\partial \theta} (\sin \theta \frac{\partial}{\partial \theta}) + \frac{1}{\sin^2 \theta} \frac{\partial^2}{\partial \phi^2} \right], \quad (2.2)$$

where  $\hbar$  is Planck's constant divided by  $2\pi$ , and  $\theta$  and  $\phi$  are the polar and azimuthal angles, respectively. The eigenvalue equation becomes

$$\hat{H}Y_l^m(\theta, \phi) = \frac{\hbar^2}{2I} l(l+1)Y_l^m(\theta, \phi), \quad (2.3)$$

where the notation  $Y_l^m(\theta, \phi)$  stands for the set of the spherical harmonics. The

energy spectrum is given by the eigenvalues

$$E_l = \frac{\hbar^2}{2I}l(l+1), \quad (2.4)$$

and is independent of  $m$  (magnetic quantum number). The energy is indeed  $(2l+1)$ -fold degenerate, because functions with fixed  $l$  (azimuthal quantum number) and  $m = -l, -l+1, \dots, l$  have the same energy. Quantum rotors may be seen as existing almost freely or coupled by intrinsic potentials (dipole interactions, etc) or acted upon by potentials inherent in the host medium. In many cases, the quantum planar rotor (QPR), i.e., endowed with only one degree of freedom, is used.

The very simple idea of the quantum rotor presented so far can be viewed as a fundamental model closest to the natural entity it may be bound to represent: the molecule. Systematic studies on the rotation of molecules supported by the quantum theory date back to Dennison [1], and Kronig and Rabi [2], who provided matrix and wave-mechanics analytical solutions to the rigid rotator (symmetrical top), both within a year or so of the respective fledgling quantum theory formulations. Later, an important study by Pauling [3] discussed the wave equation for a diatomic molecule in a crystal and tried to provide experimental interpretation of the results.

The microscopic dynamics of quantum rotors has been ever since extensively studied in view of its enormous physical and chemical interest and has always been a source of new physics. Real physical systems like molecular cryocrystals, adsorbed monolayers of diatomic molecules such as  $\text{H}_2$ ,  $\text{HD}$ ,  $\text{D}_2$ ,  $\text{N}_2$ ,  $\text{CO}$ , and  $\text{F}_2$  can be described by the QLR model [4–6]. The QLR manifests also nontrivial quantum properties such as quantum orientational ordering [6, 7], quantum orientational melting [4, 6, 8, 9], reentrant behavior [10], and discontinuity points on the phase diagram [11]. In the latter it is reported evidence for the novel phase behavior in

quantum rotors: at zero temperature, instead of an end critical point of the liquid-gas type, the phase transition line in a certain range of crystal fields displays two critical points with a discontinuity ("hole") between them. By endowing the QLR with an intrinsic angular momentum (spin) it is possible to study the unusual thermodynamics and magnetic properties of molecular crystals containing magnetically active molecules or molecular groups [12].

The notion of quantum rotors can also be advantageously applied to the understanding of interstitial oxygen impurities in crystalline germanium, where oxygen atoms are quantum-mechanically delocalized around the bond center position [13, 14]. Also the correlated dynamics of coupled quantum rotors ( $\text{Ge}_2\text{O}$  units) carrying electric dipole moments is used to gain insight into the peculiar and non-trivial low-temperature properties of doped germanium [15]. The rotation of oxygen impurities around the Ge-Ge axis has been experimentally observed by phonon spectroscopy [16]. While the rotation of oxygen impurities in Ge is weakly hindered by an azimuthal potential caused by the host lattice, several materials are known to show a free rotation of molecules. An example is ammonia groups in certain Hofmann clathrates  $\text{M}(\text{NH}_3)_2\text{M}'(\text{CN})_4\text{-G}$  [17–19], usually abbreviated as  $\text{M-M'-G}$ , where M and M' are divalent metal ions and G is a guest molecule. Nearly free uniaxial quantum rotation of  $\text{NH}_3$  has been observed for the first time in  $\text{Ni-Ni-(C}_6\text{D}_6)_2$  by inelastic neutron scattering [17]. It is also known that the phase II [20] of solid methane as well as methane hydrates [21] show almost free rotation of  $\text{CH}_4$  molecules. A surprising variation of the linewidth has been observed for  $\text{Ni-Ni-(C}_{12}\text{H}_{10})_2$  [22], which can be interpreted as a novel line-broadening mechanism based on rotor-rotor couplings [23]. The linewidths of methane in hydrates show inhomogeneous broadening owing to the dipolar coupling with water molecules [24]. The

theory of the damped rotation of methyllike atomic groupings and more complex molecules such as benzene rings is developed through the use of hindered (N-fold) quantum rotors in contact with a thermal bath [25, 26].

Arrays of surface-mounted quantum rotors with electric dipole moments are of particular interest because dipole-dipole interactions can be controlled and even designed to yield a specific behavior such as ferroelectricity. Ordered two-dimensional arrays of dipole rotors yield either ferroelectric or antiferroelectric ground states, depending on the lattice type, while disordered arrays are predicted to form a glass phase [27, 28]. These facts prop up the role of quantum rotors as a fundamental element of molecular machines, an old and new field of endeavor of both synthetic chemistry and nanotechnology [29–33].

The kicked rotor has played a central role in the research of both classical and quantum chaos (which is defined as the quantum behavior of a system whose classical counterpart is chaotic). A kicked rotor is formed by a particle revolving in a fixed circular orbit and subject to an instantaneous force (a kick) that is applied periodically. The driven rotor is operated on by pulses of any form (generally strong). Despite its apparent simplicity, the quantum kicked rotor has very remarkable dynamical properties [34–38]. Since its experimental realization in 1995 [39], a great number of studies have been produced involving dynamical localization, quantum transport, ratchets, chaos-assisted tunneling, and classical and quantum resonances. Quantum resonances in turn have been used in understanding fundamental aspects of quantum chaos such as quantum stabilization or measurements of gravitation [37]. High-order quantum resonances have also been observed recently both with laser-cooled atoms and a Bose-Einstein condensate [40–42].

We now move up a notch toward a more elaborated rotor model that finds

applications specially in the study of quantum phase transitions, the main goal of this work as far as quantum rotors and spin systems are concerned. So, we present another glimpse of the quantum mechanics involved [43]. Each rotor can be constructed as a particle constrained to move on the surface of an  $N$ -dimensional sphere. Here we treat our Euclidean space as having ( $N > 1$ ) dimensions, a quite natural extension nowadays. We thus have the so-called  $O(N)$  quantum rotor model. The orientation of each rotor is represented by an  $N$ -component unit vector  $\hat{\mathbf{n}}_i$  satisfying:

$$\hat{\mathbf{n}}^2 = 1. \quad (2.5)$$

The caret notation should be reminiscent of the fact that the rotor orientation is a quantum operator, while  $i$  indexes the site whereupon the rotor resides. For the time being, it will be considered an infinite number of such rotors placed on the sites of a  $d$ -dimensional lattice. Each rotor possesses a linear momentum  $\hat{\mathbf{p}}_i$  and constraint (2.5) obliges it to be tangent to the surface of the  $N$ -dimensional sphere

$$\hat{\mathbf{n}} \cdot \hat{\mathbf{p}} = 0. \quad (2.6)$$

The rotor position and momentum obey the canonical commutation relations:

$$[\hat{n}_\alpha, \hat{p}_\beta] = i\hbar\delta_{\alpha\beta}. \quad (2.7)$$

It seems more convenient to work with the  $N(N - 1)$  components of the angular momentum tensor:

$$\hat{L}_{\alpha\beta} = \hat{n}_\alpha \hat{p}_\beta - \hat{n}_\beta \hat{p}_\alpha. \quad (2.8)$$

Their commutation relations follow directly from Eqs. (2.7) and (2.8). Of foremost

importance is the  $N = 3$  case. The angular momentum can be more conveniently expressed as

$$\hat{L}_\alpha = (1/2)\epsilon_{\alpha\beta\gamma}\hat{L}_{\beta\gamma}, \quad (2.9)$$

or alternatively

$$\hat{L}_\alpha = -i\hbar\epsilon_{\alpha\beta\gamma}\hat{n}_\beta\frac{\partial}{\partial\hat{n}_\gamma}, \quad (2.10)$$

where  $\epsilon_{\alpha\beta\gamma}$  stands for the Levi-Civita tensor (totally antisymmetric tensor, with  $\epsilon_{123} = 1$ ). Obviously the constraint Eq. (2.6) carries through to

$$\hat{\mathbf{n}} \cdot \hat{\mathbf{L}} = 0. \quad (2.11)$$

Accordingly, the commutation relations between operators standing on the same site follow:

$$\begin{aligned} [\hat{L}_\alpha, \hat{L}_\beta] &= i\hbar\epsilon_{\alpha\beta\gamma}\hat{L}_\gamma, \\ [\hat{L}_\alpha, \hat{n}_\beta] &= i\hbar\epsilon_{\alpha\beta\gamma}\hat{n}_\gamma, \\ [\hat{n}_\alpha, \hat{n}_\beta] &= 0; \end{aligned} \quad (2.12)$$

operators situated on different sites commute. The rotor dynamics is governed by its kinetic energy term, which may be expressed as

$$\hat{H}_K = \frac{1}{2I}\hat{\mathbf{L}}^2 \rightarrow \frac{g}{2}\hat{\mathbf{L}}^2, \quad (2.13)$$

where  $I$  is the moment of inertia and we have introduced a coupling  $g$ . The Hamiltonian  $\hat{H}_K$  can be diagonalized for general values of  $N$  by making use of group theory. For  $N = 3$ , the eigenvalues were already shown through Eq. (2.3) and Eq.

(2.4). Interesting effects show up when a potential energy term coupling the rotors together is added. Then we construct the Hamiltonian, which has been object of intensive study:

$$\hat{H}_{rot} = \frac{g}{2} \sum_i \hat{\mathbf{L}}_i^2 + J_{ij} \sum_{\langle ij \rangle} \hat{\mathbf{n}}_i \cdot \hat{\mathbf{n}}_j, \quad (2.14)$$

where the notation  $\langle ij \rangle$  indicates the sum over nearest neighbors, and  $J_{ij}$  represent couplings between the respective rotor orientations. A generalization thereof, with the addition of novel couplings, will be considered shortly.

Quantum transitions of models based on Eq. (2.14) and its Ising-model counterpart have been extensively studied for decades. A review of the theoretical investigations as well as their experimental connotations can be found in the book by Sachdev [43]. The effort to understand the model goes on and every now and then rich and interesting phase diagrams unfold, which yield invaluable insights into the real physical systems. So, quantum rotors have been studied and their phase diagram investigated through renormalization group techniques [44], the dynamics and thermodynamics of interacting one-dimensional quantum rotors with emphasis on equilibrium and non-equilibrium properties have been explored through a mean-field (MF) model [45], the quantum phase transitions of a site-diluted two-dimensional O(3) rotor model have been worked out through Monte Carlo simulations [46], just to mention a few additional important studies.

Dating back to a work by Sachdev and Senthil [47] there exists a generalization of the Hamiltonian in Eq. (2.14). In its most general terms, it is given by

$$\hat{H}'_{rot} = \frac{g}{2} \sum_i [\hat{\mathbf{L}}_i^2 + \alpha(\hat{\mathbf{L}}_i^2)^2] + \sum_{\langle ij \rangle} [J_{ij} \hat{\mathbf{n}}_i \cdot \hat{\mathbf{n}}_j + K_{ij} \hat{\mathbf{L}}_i \cdot \hat{\mathbf{L}}_j + M_{ij}(\hat{\mathbf{n}}_i \cdot \hat{\mathbf{L}}_j + \hat{\mathbf{n}}_j \cdot \hat{\mathbf{L}}_i)], \quad (2.15)$$

where for O(3) rotors the three-component unit position vector (operator) and

the canonically conjugate angular momentum (operator) are explicitly given by  $\hat{\mathbf{n}} = (\hat{n}_x, \hat{n}_y, \hat{n}_z)$ ,  $\hat{\mathbf{L}} = (\hat{L}_x, \hat{L}_y, \hat{L}_z)$ , respectively, and the couplings  $g$ ,  $\alpha$ ,  $J$ ,  $K$  e  $M$  are all positive. The introduction of the couplings  $K$  and  $M$  in Eq.(2.15) enriches the model and yields novel results in relation to systems modeled by the Hamiltonian of Eq. (2.14). A fundamental property of  $\hat{H}'_{rot}$  is that the three charges ( $\mu = x, y, z$ )

$$\hat{Q}_\mu = \sum_i \hat{L}_{i\mu}, \quad (2.16)$$

commute with it, and are therefore conserved. A quartic term, with coefficient  $g\alpha$ , is inserted and acts as an inhibitor of contributions of unimportant high-energy states. For in-depth considerations of the model, a knowledge of the pertinent discrete symmetries may afford one a vantage point. In this respect, the model boasts time-reversal symmetry, and for the special case  $M = 0$ , spatial inversion (parity) is also present. Time-reversal symmetry is realized by the transformations:

$$\tau : \hat{L}_\mu \rightarrow -\hat{L}_\mu, \quad \hat{n}_\mu \rightarrow \hat{n}_\mu, \quad (2.17)$$

and parity by

$$\pi : \hat{L}_\mu \rightarrow \hat{L}_\mu, \quad \hat{n}_\mu \rightarrow -\hat{n}_\mu. \quad (2.18)$$

The MF phase diagram of  $\hat{H}'_{rot}$  was then reproduced in Fig. 2.1, where all the phases are duly described. The figure shows, for instance, that the distinction between the GP and the N phases can only be made through the value of  $\langle \hat{n}_z \rangle$ , which happens to be zero in the former and nonzero in the latter phase. This phase diagram exemplifies the case of rotors with  $q = 0$ , that is, rotors whose minimum angular momentum is zero. We see that there is a gap to all excitations. The phase



diagram for  $q = 1/2$  rotors, that is, rotors whose minimum angular momenta has the value  $l = 1/2$  bears a close resemblance with the one presented here, except for one important difference: it does not possess an energy gap (the GP phase is absent), as is reasonable to expect so. The momentum-state tower of each rotor is not limited (only the first two  $QF_l$  phases are shown), and this fact leads to the interpretation of a rotor as an effective quantum degree of freedom for the low energy states of a small number (even, when  $2q$  is pair, and odd, if  $2q$  is odd) of closely coupled electrons. In this work we shall relinquish this interpretation and adopt a simpler one: we will attempt to "lure" each rotor into representing just a single spin posed on each site. The more precise meaning of  $q$  shall be addressed in a short while.

The connection between  $O(N)$  quantum-rotor (QR) and spin models on  $d$ -dimensional lattices has proved very useful in the context of phase transitions [43, 48]. About three decades ago, Hamer, Kogut and Susskind [49] mapped two-dimensional  $O(N)$  Heisenberg models ( $N = 2, 3$  and  $4$ ) onto the corresponding [(1+1) spatial and time dimensions] nonlinear-sigma or QR models. The critical behavior was then inferred using strong-coupling expansion (high-temperature,  $g = kT/J \rightarrow \infty$ , where  $J$  is the spin coupling): a Kosterlitz-Thouless transition for the  $O(2)$  model and a prediction of critical points at zero coupling (Padé continued) for both  $O(3)$  and  $O(4)$  models. On the other hand, by mapping  $O(3)$  antiferromagnetic (AF) Heisenberg chains onto nonlinear sigma models in the semiclassical weak-coupling limit ( $g = 2/S, S \rightarrow \infty$ ), Haldane [50] suggested that the ground state of chains with integral spins are gapped, while those with half-integral spins are gapless. Moreover, Shankar and Read [51] precisely clarified the distinction between gapped AF spin models, characterized by the  $\theta = 0 \bmod 2\pi$  topological term, and gapless models for which  $\theta = \pi \bmod 2\pi$ , including the connection of the latter with a Laplacian

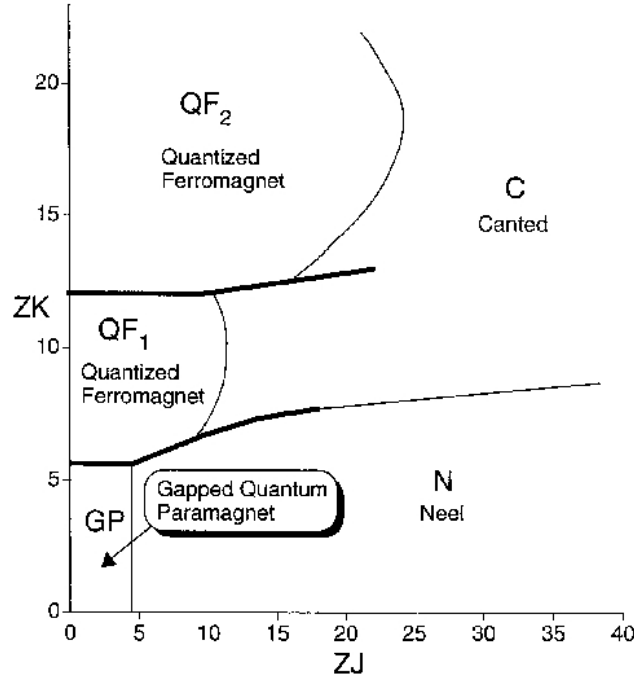


Figure 2.1: MF phase diagram of  $\hat{H}'_{rot}$  as a function of the couplings  $J$  and  $K$  at  $MZ = 4$ ,  $g = 1$ , and  $\alpha = 1$ ;  $Z$  is the coordination number of the lattice. Thin lines represent second-order transitions while thick lines are first order. The quantized ferromagnetic phases  $QF_l$  have magnetic moment per site  $l$ ; there is an infinite sequence of such phases for all integer  $l > 0$  at larger values of  $K$ , and only the first two are shown. The phases have the following ground-state expectation values, up to a global  $O(3)$  rotation: gapped quantum paramagnet (GP):  $\langle \hat{L}_\mu \rangle = 0$ ,  $\langle \hat{n}_\mu \rangle = 0$ ; quantized ferromagnet ( $QF_l$ ):  $\langle \hat{L}_z \rangle = l$ ,  $\langle \hat{n}_z \rangle \neq 0$ ;  $\langle \hat{L}_{x,y} \rangle = 0$ ,  $\langle \hat{n}_{x,y} \rangle = 0$ ; Néel ( $N$ ):  $\langle \hat{L}_\mu \rangle = 0$ ,  $\langle \hat{n}_z \rangle \neq 0$ ,  $\langle \hat{n}_{x,y} \rangle = 0$ ; canted ( $C$ ):  $\langle \hat{L}_{x,z} \rangle \neq 0$ ,  $\langle \hat{n}_{x,z} \rangle \neq 0$ ,  $\langle \hat{L}_y \rangle = 0$ ,  $\langle \hat{n}_y \rangle = 0$  (reproduced from Ref. [47]).

minimally coupled to the monopole potential [52]. In fact, by putting the model on a lattice and adopting a nontrivial procedure, which ended up with the inclusion of the  $\theta = \pi$  term into the known theory, they worked out the discretized version of the sigma model, whose action reads

$$S = - \int_0^\beta d\tau \sum_j \left\{ \frac{[\partial_\tau \mathbf{n}(j)]^2}{2g^2} - \frac{i}{2} (-1)^j \mathbf{A}(\mathbf{n}(j)) \cdot \frac{d\mathbf{n}}{d\tau} + \frac{1}{2g^2} [\mathbf{n}(j) - \mathbf{n}(j+1)]^2 \right\}, \quad (2.19)$$

where  $\mathbf{n} = \mathbf{n}(\tau)$  is the unit position vector,  $g$  is a coupling constant,  $\mathbf{A}(\mathbf{n})$  (with  $\nabla_{\mathbf{n}} \times \mathbf{A} = \mathbf{n}$ ) is the vector potential, and  $j$  labels the lattice sites. A remarkable result in Eq. (2.19) arises from its second term. It tells us of a particle that at each site is constrained to move on a unit sphere acted upon by the field of a unit monopole. Further, masslessness (gaplessness) at  $\theta = \pi$  for all nonzero  $g$  is inferred, and this leads to the mapping of the sigma model onto the spin-1/2 nearest-neighbor antiferromagnetic Heisenberg chain. The angular part of the Laplacian  $\hat{\mathbf{L}}^2$  (see Eq. (29) in the cited article) is constructed and can easily be linked (by setting  $q = 1/2$  and using  $m \rightarrow -i\frac{\partial}{\partial\phi}$ ) to the ordinary differential equation for the  $\theta$ -dependent part of the monopole harmonics [52], namely:

$$[l(l+1) - q^2] \Theta_{q,l,m} = \left[ -\frac{1}{\sin\theta} \frac{\partial}{\partial\theta} (\sin\theta \frac{\partial}{\partial\theta}) + \frac{1}{\sin^2\theta} (m + q \cos\theta)^2 \right] \Theta_{q,l,m}, \quad (2.20)$$

which is a direct evaluation of the operator  $[\hat{\mathbf{r}} \times (\hat{\mathbf{p}} - Ze\hat{\mathbf{A}})]^2$  acting on the  $Y_{q,l,m}(\theta, \phi)$  - the so-called monopole harmonics. Here  $2q$  is any integer (positive, negative, or zero) and is directly related to the monopole strength. We will provide further treatment of this subject in appendix A.1. Following the above developments, Sachdev and Senthil [43, 47] have presented a quite general MF and renormalization-group analysis of quantum phase transitions in magnets with the aid of the generalized

QR modeled by the Hamiltonian that was already introduced in Eq. (2.15). In particular, they showed that, under certain conditions, one can establish a mapping of double-layer antiferromagnets onto quantum rotors which sheds intuitive light on the way in which a quantum rotor can be used as an effective representation of a pair of antiferromagnetically coupled spins.

Still in a similar context, a single-site MF approximation was used to study an effective Hamiltonian for spin-one bosons in an optical lattice in the presence of a magnetic field [53]. Further, a QR description of the Mott-insulator transition in the Bose-Hubbard model within a functional-integral approach has also been elaborated in order to include particle number fluctuation effects [54]. Low-dimensional bosonic systems described in terms of the (disordered) Hubbard model can effectively be studied through equivalent QR models, such as carried out by Alet and Sorensen [55] by way of a wormlike cluster Monte Carlo algorithm. Pushing the theory far afield, Levin *et al.* found that the rotor model on the 3D cubic lattice can exhibit low-energy excitations which behave like massless U(1) gauge bosons and massless Dirac fermions [56].

In this chapter we focus our attention on the study of the ground-state phase diagram of generalized quantum rotors on the frustrated AB<sub>2</sub> chain, modeled by a Hamiltonian similar to that defined by Eq. (2.15). The (rotor) AB<sub>2</sub> chain is depicted in Fig. 2.2. The quantum rotors at each site are constrained, through sufficiently high values of the coupling  $g$  (and the coupling  $\alpha$  of the quartic term in the angular momentum), to mostly retain states with the minimum value of the angular momentum, i.e.,  $\ell = 1/2$ , as the frustration parameter  $J$  is varied, thus enabling us to make a direct comparison with the corresponding quantum *spin-1/2* AB<sub>2</sub> chains. In this manner, each rotor can be viewed as approximately

representing only one spin  $1/2$  localized on the respective site. We analyze two types of frustration, as illustrated in Fig. 2.2, and try to interpret the derived phase diagrams in light of the ones of previous works on frustrated quantum spin- $1/2$  chains (or mixed spin- $1/2$ -spin-1 chains) with the  $AB_2$  topology [57–62]. Instead of attempting to formalize a specific (and probably rather complex) mapping between the rotor and the spin models, we have opted to treat the rotor chain numerically by using a cluster variational MF theory. In this way we were able to derive the rotor phase diagrams of both frustration cases. We also supplemented our analysis with exact diagonalization via the Lanczos algorithm (ED) [63] and density matrix renormalization group (DMRG) [64] of finite-size spin- $1/2$  chains.

With respect to spin systems, as a motivation on the experimental side, the compound  $Cu_3(CO)_2(OH)_2$ , a natural mineral that is best known by the name azurite [65], has been successfully explained by the distorted diamond chain model [61], i.e., a system with three spin- $1/2$  magnetic sites per unit cell and frustrated ferrimagnetic state. Also, along with the study on the effect of frustration [57–62], for  $J = 0$  this class of models shares its phenomenology and unit-cell topology with quasi-one-dimensional compounds, such as the line of trimer clusters present in copper phosphates [66, 67] and the ferrimagnet PNNBNO, which is the abbreviation of the organic triradical 2-[3', 5'-bis(*N-tert*-butylaminoxyl)phenyl-4,4,5,5-tetramethyl-4,5-dihydro-1*H*-imidazol-1-oxyl 3-oxide [68]. The modeling of the ferrimagnetic phase [69] has been mainly undertaken in the context of other models such as Hubbard [70],  $t - J$  [71], Ising [72], classical [72] and quantum Heisenberg [73], including magnetic excitations [74, 75], and the quantum spherical model [76]. The occurrence of new phases induced by hole-doping of the electronic band [77] has also been carried out. More recently, a topological approach to describe the frustration- and field-induced

phase transitions exhibited by the infinite-range XY model on the AB<sub>2</sub> chain, including noncollinear spin structures, was adopted [78]. Also, a functional-integral formalism suitable to describe the strong-coupling regime below half-filling of the AB<sub>2</sub> Hubbard chains was published [79].

Finally, this chapter is organized as follows. In the next section we describe our specific QR system which is modeled by the Hamiltonian  $\hat{H}'_{rot}$  of Eq. (2.15) imposed on the AB<sub>2</sub> chain for particular values of the couplings. We also provide a glimpse of the numerical methods deployed. In an appendix, we present an overview of the monopole harmonics and derive the matrix elements of the operators acting on the single-site Hilbert space represented by these functions. In Sec. 2.3 we use single-site variational MF theory to study the rotor models, for the two frustration cases, and discuss the shortcomings of this semiclassical approach. Then in Sec. 2.4 we adopt a multi-site (two-unit cell) variational MF Hamiltonian, which provides a substantial improvement on the treatment of quantum fluctuation effects, particularly in connection with the case of frustrated interaction between quantum rotors on B sites at the same unit cell. Then we treat the respective spin-1/2 systems by making use of ED and DMRG techniques in order to pave the way for a direct comparison between rotors and spins. Finally we report our conclusions in Sec. 2.5.

## 2.2 Outline of the theory and methods

Quantum rotors can be classified according to their minimum angular momentum [47, 52]: rotors with  $q = 0$  have zero minimum angular momentum, which can be made to correspond to an even number of Heisenberg spins in an underlying spin model. Free rotors with  $q = 0$  have Eq. (2.2) as eigenvalue equation: the eigenstates

are just the spherical harmonics and the eigenvalues are given by Eq. (2.4). On the other hand, we also have rotors with  $q \neq 0$ , where  $q$  is chosen to have one of the values:  $1/2, 1, 3/2, \dots$ . They have in turn Eq. (2.20) as eigenvalue equation. As we have just seen above, this arises naturally from the theory and the rotor with  $q = 0$  may be considered a particular case of a more general rotor (where  $2q$  could be any integer, including zero), which will be clarified in Appendix A.1. Quantum rotors with half-integer values of  $q$  are duly suited to refer to an odd number of underlying spins-1/2 (at least one spin remains unpaired).

We shall focus on ( $q = 1/2$ )-quantum rotors in view of the stated objective of comparing our results with those of the referred chains of spin-1/2 operators. From now on we set  $\hbar \equiv 1$ . For a general  $q$ , the angular momentum operator is now given by

$$\hat{L}_\mu = -\epsilon_{\mu\nu\lambda} \hat{n}_\nu \left[ i \frac{\partial}{\partial \hat{n}_\lambda} + q A_\lambda(\hat{n}) \right] - q \hat{n}_\mu, \quad (2.21)$$

which incorporates the effect of a Dirac monopole at the origin of  $n$  space. As before, Greek letters stand for the Cartesian components  $x, y, z$  (summation over repeated indices is subtended and  $\epsilon_{\mu\nu\lambda}$  is the Levi-Civita tensor). The vector potential  $\hat{\mathbf{A}}$  may be conveniently chosen to satisfy [52] (see also Eq. (2.19))

$$\epsilon_{\mu\nu\lambda} \partial A_\lambda / \partial \hat{n}_\nu = \hat{n}_\mu. \quad (2.22)$$

It is quite a simple task to show that the commutation relations (Eq. (2.12)) are all verified for the case of  $\hat{\mathbf{L}}$  defined by Eq. (2.21). The appropriate Hilbert space is made up of *angular section* states, which are eigenstates of Eq (2.20), for which

the following are true [52]:

$$\hat{\mathbf{L}}^2|q, l, m \rangle = l(l+1)|q, l, m \rangle, \quad \hat{L}_z|q, l, m \rangle = m|q, l, m \rangle, \quad (2.23)$$

and the usual ladder operators ( $\hat{L}_\pm = \hat{L}_x \pm i\hat{L}_y$ ) satisfy

$$\hat{L}_\pm|q, l, m \rangle = \sqrt{(l \mp m)(l \pm m + 1)}|q, l, m \pm 1 \rangle. \quad (2.24)$$

Here  $l = q, q+1, q+2, \dots$ , and  $m = -l, -l+1, \dots, l$ . The  $|q, l, m \rangle$  are the eigensections also called *monopole harmonics*. An important constraint follows immediately from Eq.(2.21):

$$\hat{\mathbf{n}} \cdot \hat{\mathbf{L}} = -q. \quad (2.25)$$

Thus, we shall consider the quite general frustrated O(3) QR Hamiltonian for the quantum rotors placed on the sites of a chain with the AB<sub>2</sub> topology:

$$\begin{aligned} \hat{H}_R = & \frac{g}{2} \sum_i [(\hat{\mathbf{L}}_i^2 + \alpha(\hat{\mathbf{L}}_i^2)^2)] + \sum_{\langle ij \rangle} [\hat{\mathbf{n}}_i \cdot \hat{\mathbf{n}}_j + \hat{\mathbf{L}}_i \cdot \hat{\mathbf{L}}_j + M(\hat{\mathbf{n}}_i \cdot \hat{\mathbf{L}}_j + \hat{\mathbf{n}}_j \cdot \hat{\mathbf{L}}_i)] + \\ & \sum_{(i,j) \in F_1 \text{ or } F_2} [J(\hat{\mathbf{n}}_i \cdot \hat{\mathbf{n}}_j + \hat{\mathbf{L}}_i \cdot \hat{\mathbf{L}}_j) + M(\hat{\mathbf{n}}_i \cdot \hat{\mathbf{L}}_j + \hat{\mathbf{n}}_j \cdot \hat{\mathbf{L}}_i)]. \end{aligned} \quad (2.26)$$

This is nevertheless a special case of the more general Hamiltonian given by Eq. (2.15), where the restrictions on the couplings  $J_{ij}, K_{ij}, M_{ij}$  are already taken into account and explicitly shown in Eq. (2.26). A word about the special notation used here is in order. The index  $i$  labels the sites of the AB<sub>2</sub> chain; in the second summation,  $\langle ij \rangle$  indexes nearest-neighbor couplings between rotors on distinct sublattices (A and B sublattices) which, except for  $M$ , are all set to unity (see Fig. 2.2, illustrated by the full lines); in the third summation  $(i, j)$  indexes nearest-



neighbor couplings between rotors on the same sublattice which, except for  $M$ , are set to  $J(\geq 0)$ . Here we shall study two frustration patterns, namely,  $F_1$  and  $F_2$ . In  $F_1$ , only frustrated interactions ( $J$  and  $M$ ) between rotors at the B sites of the same unit cell are present, as illustrated in Fig. 2.2 (a) (red dashed lines), whereas for  $F_2$  we consider *all* nearest-neighbor intra- and intercell interactions, as illustrated in Fig. 2.2 (b) (red and green dashed lines). In order to isolate the effect of the coupling  $M$  in the two above-referred cases, we take either  $M = 0$  or  $M = 1$ .

We then start off by treating  $\hat{H}_R$  by means of a variational MF theory based on the Bogoliubov theorem [80, 81]. Thus, the variational expression of the MF energy at  $T = 0$  satisfies the inequality:

$$E_{mf} \leq E_0 + \langle \hat{H}_R - \hat{H}_{trial} \rangle_0, \quad (2.27)$$

where  $E_0$  is the ground-state energy of the trial Hamiltonian - here denoted by  $\hat{H}_{trial}$  - and the expectation value is taken with respect to its ground-state wavefunction. So, we need firstly to diagonalize  $\hat{H}_{trial}$  by way of the Lanczos algorithm [63] to construct the Bogoliubov inequality, which is then minimized with respect to its variational parameters: for chosen values of the frustration control parameter ( $J$ ), minimization is carried out numerically, by deploying a simplex procedure [82].

For trial Hamiltonians we use both single-site and multi-site Hamiltonians, as described in Sec. 2.3 and Sec. 2.4, respectively.

Before going on to the two approaches described in Sec. 2.3 and Sec. 2.4, we emphasize the following features about the *stability* of the numerical implementations carried out in this work. So, in our simulations we have verified that we could safely work with a minimally reduced Hilbert space if the values of  $g$  and  $\alpha$  were set sufficiently large. In fact, the Hilbert space size and the value of  $g$  and  $\alpha$  determine

the stability of our problem: for small space sizes (e.g.,  $\ell = 3/2$ ) and small values of  $g$  and  $\alpha$  (e.g.,  $g = \alpha = 0.1$ ), the system becomes completely unstable due to contributions of high-energy terms which cause the system to fluctuate beyond control. On the other hand, by choosing a small space size ( $\ell = 3/2$ ), but a sufficiently large value of  $g$ , the system behaves quite stably. Therefore, in this work we shall use small space size, i.e.,  $\ell = 3/2$ , associated with a large value of  $g$ , in order to make computations feasible and establish a close contact with spin-1/2 models. We shall exhibit an example of this phenomenon in due time.

## 2.3 Quantum rotors on the AB<sub>2</sub> chain: single-site variational mean-field approach on the unit cell

As a first and straightforward application of the aforementioned variational MF theory, we postulate the following trial Hamiltonian, acting on one unit cell of the AB<sub>2</sub> chain:

$$\hat{H}_{trial} = \sum_i \left[ \frac{g}{2} \left( \hat{\mathbf{L}}_i^2 + \alpha (\hat{\mathbf{L}}_i^2)^2 \right) + \mathbf{N}_i \cdot \hat{\mathbf{n}}_i + \mathbf{h}_i \cdot \hat{\mathbf{L}}_i \right], \quad (2.28)$$

where  $\mathbf{h} = (h_x, h_y, h_z)$  and  $\mathbf{N} = (N_x, N_y, N_z)$  are the variational c-number fields and the subscript  $i$  goes over the sites  $A_1$ ,  $B_1$ , and  $B_2$ .

The ground-state wavefunction of  $\hat{H}_{trial}$  and energy are given by

$$|\Psi_0\rangle = |\Psi_0\rangle_{A_1} |\Psi_0\rangle_{B_1} |\Psi_0\rangle_{B_2} \quad (2.29)$$

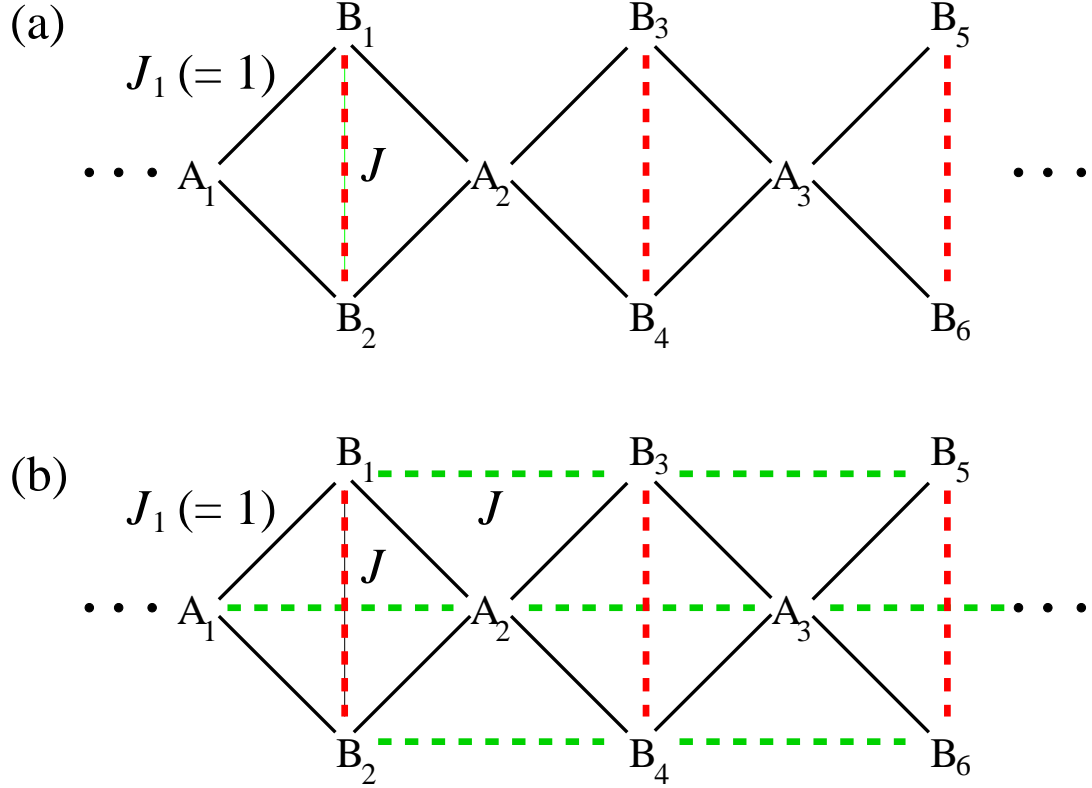


Figure 2.2: Illustration of the QR chains with three rotors per unit cell  $i$ :  $A_i$ ,  $B_{2i-1}$ , and  $B_{2i}$ . Full lines indicate antiferromagnetic exchange couplings ( $J_1 \equiv 1$ ) which give rise to the ferrimagnetic ground state, while dashed lines represent exchange couplings ( $J \geq 0$ ) which frustrate the magnetic order: (a) frustration pattern F<sub>1</sub> and (b) frustration pattern F<sub>2</sub>.

and

$$E_0 = \sum_i E_{0_i} = E_{0_{A_1}} + E_{0_{B_1}} + E_{0_{B_2}}, \quad (2.30)$$

where  $E_{0_i} = E_{0_i}(g, \alpha; N_i, h_i)$  represents the ground-state energy of the respective wavefunction, such that for any pair of operators  $\hat{\mathbf{X}}_i, \hat{\mathbf{X}}_j$ , with  $i \neq j$ :

$$\langle \Psi_0 | \hat{\mathbf{X}}_i \cdot \hat{\mathbf{X}}_j | \Psi_0 \rangle = \langle \hat{\mathbf{X}}_i \rangle_0 \cdot \langle \hat{\mathbf{X}}_j \rangle_0, \quad (2.31)$$

We then get, for frustration F<sub>1</sub>, the Bogoliubov inequality *for the unit cell*:

$$E_{mf}^{(F_1)} \leq E_1 + E_2 + E_3, \quad (2.32)$$

where the  $E_\nu$  read:

$$\begin{aligned} E_1 &= \sum_i E_{0_i} - \sum_i (\mathbf{N}_i \cdot \langle \hat{\mathbf{n}}_i \rangle_0 + \mathbf{h}_i \cdot \langle \hat{\mathbf{L}}_i \rangle_0); \\ E_2 &= 2 \sum_{i>j, j=A_1} [\langle \hat{\mathbf{n}}_i \rangle_0 \cdot \langle \hat{\mathbf{n}}_j \rangle_0 + \langle \hat{\mathbf{L}}_i \rangle_0 \cdot \langle \hat{\mathbf{L}}_j \rangle_0 \\ &\quad + M(\langle \hat{\mathbf{n}}_i \rangle_0 \cdot \langle \hat{\mathbf{L}}_j \rangle_0 + \langle \hat{\mathbf{n}}_j \rangle_0 \cdot \langle \hat{\mathbf{L}}_i \rangle_0)]; \\ E_3 &= J(\langle \hat{\mathbf{n}}_{B_1} \rangle_0 \cdot \langle \hat{\mathbf{n}}_{B_2} \rangle_0 + \langle \hat{\mathbf{L}}_{B_1} \rangle_0 \cdot \langle \hat{\mathbf{L}}_{B_2} \rangle_0) + \\ &\quad M(\langle \hat{\mathbf{n}}_{B_1} \rangle_0 \cdot \langle \hat{\mathbf{L}}_{B_2} \rangle_0 + \langle \hat{\mathbf{n}}_{B_2} \rangle_0 \cdot \langle \hat{\mathbf{L}}_{B_1} \rangle_0); \end{aligned}$$

the index  $i$  ( $j$ ) visits the sites of the unit cell, with the convention:  $A_1 < B_1 < B_2$ .

For frustration F<sub>2</sub>, a fourth term must be added to the Bogoliubov inequality:

$$E_4 = 2 \sum_i [J \langle \hat{\mathbf{n}}_i \rangle_0 \cdot \langle \hat{\mathbf{n}}_i \rangle_0 + \langle \hat{\mathbf{L}}_i \rangle_0 \cdot \langle \hat{\mathbf{L}}_i \rangle_0 + \\ M(\langle \hat{\mathbf{n}}_i \rangle_0 \cdot \langle \hat{\mathbf{L}}_i \rangle_0 + \langle \hat{\mathbf{n}}_i \rangle_0 \cdot \langle \hat{\mathbf{L}}_i \rangle_0)].$$

The GS wavefunction and energy of  $\hat{H}_{trial}$  are obtained through ED. The MF energy – best evaluation of  $E_{mf}^{(F_1)} \equiv E_{mf}^{(F_1)}(g, \alpha, J)$  or  $E_{mf}^{(F_2)} \equiv E_{mf}^{(F_2)}(g, \alpha, J)$  – is then obtained by performing the minimization with respect to variations of the fields  $\mathbf{N}_i$  and  $\mathbf{h}_i$ .

To produce the results of this section, it sufficed to set  $g = \alpha = 10$  and a space size determined by truncating the Hilbert space at  $\ell = 3/2$ . Further, we have focused only on those quantities that suffice to afford the relevant information needed for the proper interpretation of the problem at this level, i. e., the two-point MF momentum products, defined here through the products  $\langle \hat{\mathbf{L}}_i \rangle \cdot \langle \hat{\mathbf{L}}_j \rangle$ , where  $i \neq j$  runs over the sites of the unit cell, and the MF energy. We thereby leave out the position- and momentum-position products, for they are redundant. This is due to the fact that  $\hat{L}_\mu$  and  $\hat{n}_\mu$  have the same signature under all allowed symmetries for  $q \geq 0$ , and so their expectation values turn out to be proportional to each other on a given site [47].

We then proceed to discuss the results in Fig. 2.3 (frustration F<sub>1</sub>) and Fig. 2.4 (frustration F<sub>2</sub>), which reveal some salient features. Firstly, we verified that the classical result  $\langle \hat{\mathbf{L}}_i \rangle^2 = 0.25$ , with  $i = A_1, B_1, B_2$ , independent of  $J$ , is produced. The momentum products show that, *in all cases*, the system starts out with a magnetization plateau:  $\langle \hat{\mathbf{L}}_{B_1} \rangle \cdot \langle \hat{\mathbf{L}}_{B_2} \rangle = 0.25$  and  $\langle \hat{\mathbf{L}}_{A_1} \rangle \cdot \langle \hat{\mathbf{L}}_{B_{1,2}} \rangle = -0.25$ , which corresponds to the Lieb-Mattis[83] phase of the analogous spin-1/2 system, before undergoing a phase transition at  $J = 1$ . This transition is of second order

( $M \equiv 0$ ), as shown in Fig. 2.3 (a) and Fig. 2.4 (a), and of first order ( $M \equiv 1$ ), as shown in Fig. 2.3 (c) and Fig. 2.4 (c).

In the first case ( $M \equiv 0$ ), the system evolves continually (with the MF energy curve - Fig. 2.3 (b) and Fig. 2.4 (b) - smooth at the point  $J = 1$ ) to a stable phase where the momenta at the A and B sites become uncorrelated, i.e.,  $\langle \hat{\mathbf{L}}_{A_1} \rangle \cdot \langle \hat{\mathbf{L}}_{B_{1,2}} \rangle \approx 0$ , while the momenta at the B sites tend to directly oppose each other with increasing  $J$ , forming a singletlike configuration:  $\langle \hat{\mathbf{L}}_{B_1} \rangle \cdot \langle \hat{\mathbf{L}}_{B_2} \rangle \approx -0.25$ , for  $J \gg 1$ .

In the second case ( $M \equiv 1$ ), the transition takes place quite abruptly, having undoubtedly first-order characteristics, and the system immediately accommodates into the stable singletlike phase that we have just referred to. The MF energy curves of these first-order transitions at  $J = 1$  are shown in Fig. 2.3 (d) and Fig. 2.4 (d), and we notice that the cusp in the latter is less pronounced.

We notice further, that the products between the momenta at the A and B sites display quite sizable fluctuations around  $\langle \hat{\mathbf{L}}_{A_1} \rangle \cdot \langle \hat{\mathbf{L}}_{B_{1,2}} \rangle \approx 0$ , as seen in Fig. 2.3 (c) and Fig. 2.4 (c) ( $M \neq 0$ ), and in lesser degree in Fig. 2.4 (a) for frustration  $F_2$  and  $M = 0$ . The corresponding wide points occur pairwise and fairly symmetrically with respect to the classical curves (see below) that represent the decoupling of the momenta at the A and B sites, leaving the MF energy practically unaltered. In fact, with increasing  $J$ , the system becomes more prone to wandering through near-degenerate states, which give rise to these stray points.

The phase, for  $J \gg 1$ , with the A sites uncoupled and the B sites with opposing momenta in a singletlike configuration, is much like the dimer-monomer phase of the work by Takano, Kubo, and Sakamoto [57]. We perceive, however, that important features in between those  $J$  extremes of the phase diagram do not appear by way of

this naive *single-site* MF theory.

We now get back to the instability situation mentioned in the previous section. When the Hilbert space is truncated at a small value of  $\ell$  and the system is given free reins to accomodate in higher-energy states (through a small value of  $g$  and  $\alpha$ ), then we end up by having an ill-defined problem in our hands. It happens that truncation problems (the system seeks out nonexistent states in the cutoff region) make numerical implementation errors too important. The result is we come up with a picture that is totally blurred and no physics arises, as can be visualized in Fig. 2.5. On the other hand, for larger values of  $\ell$  ( $\ell = 6.5$ , in this example), the phase diagram is stable and shows the same pattern that was analyzed so far (see Fig. 2.3). But all momenta are scaled up thirteenfold to the maximum  $\ell = 6.5$  value, and we understand this behavior as a signature of an all-classical system. This is illustrated in Fig. 2.6.

We now notice, through Eq. (2.31), that with the rotor momenta being fixed at  $\ell = 1/2$ , and having  $\langle L_i \rangle^2 = 0.25$ , for all sites  $i$ , independent of  $J$ , all dot products can only vary between the extremes -0.25 and 0.25. Therefore, through this MF approach, we are led to envision the momenta on the unit cell of the AB<sub>2</sub> chain as classical vectors of constant magnitude, such as represented in Fig. 2.7. We can thus provide a simple interpretation based on this configuration of classical vectors on the  $xy$  plane (akin to the XY model). We then build the energy function for the configuration in Fig. 2.7 on a symmetric unit of the AB<sub>2</sub> chain centered on the A site. The classical constraints may be set as

$$\begin{aligned} |\mathbf{L}_{A_l}| &= |\mathbf{L}_{B_1}| = |\mathbf{L}_{B_2}| \equiv 1/2, \\ |\mathbf{n}_{A_l}| &= |\mathbf{n}_{B_1}| = |\mathbf{n}_{B_2}| \equiv n, \end{aligned} \tag{2.33}$$

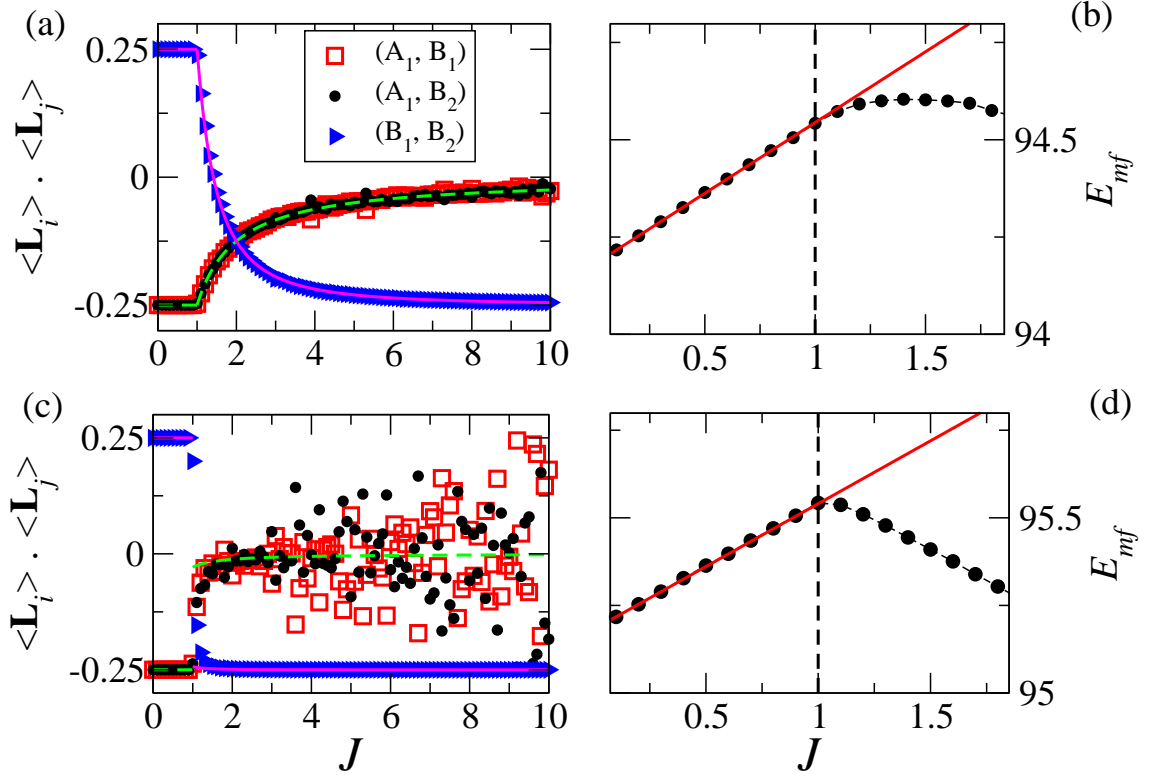


Figure 2.3: Frustration  $F_1$ . Two-point MF momentum products [(a)  $M \equiv 0$ , (c)  $M \equiv 1$ ] between the indicated rotors and MF energy curve [(b)  $M \equiv 0$ , (d)  $M \equiv 1$ ], where we have drawn straight (full) lines to show that at  $J = 1$  the system steers away from the linear regime that prevails for  $J \leq 1$  and so a phase transition takes place. Full and dashed lines in (a) and (c) indicate the results of the classical vector model. Dashed lines in (b) and (d) are guides to the eye.



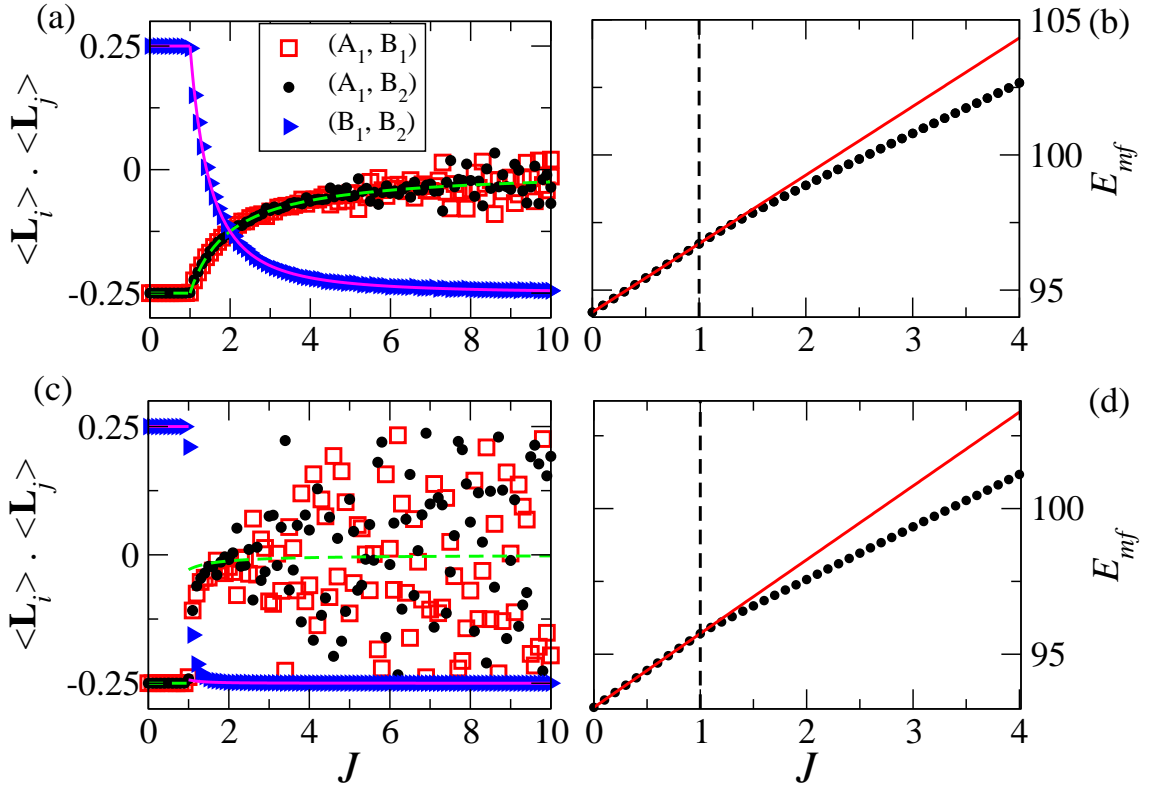


Figure 2.4: Frustration F<sub>2</sub>. Same as in Fig. 2.3.

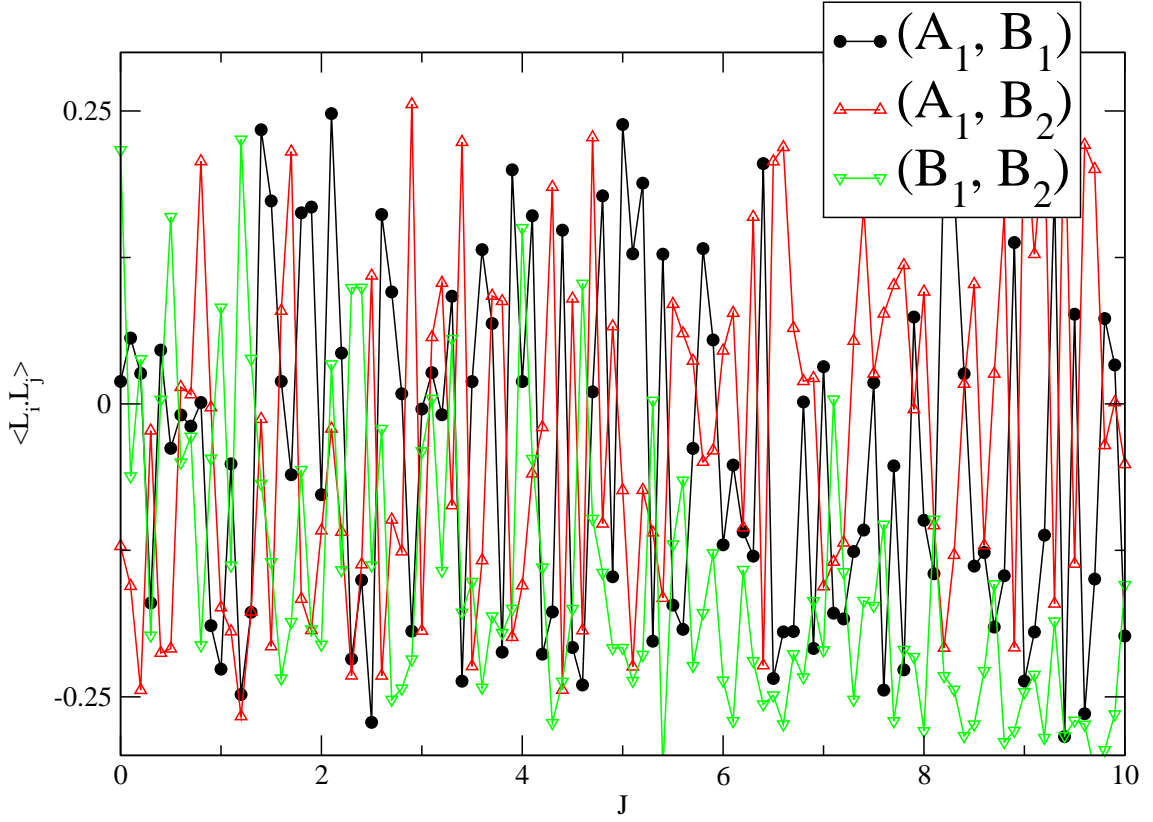


Figure 2.5: Two-point MF momentum products for frustration  $F_1$ . Here an inappropriate choice of the parameters  $g = \alpha = 1$  and a Hilbert space truncated at  $\ell = 1/2$  was made. One cannot make any physical pattern out of the plots.

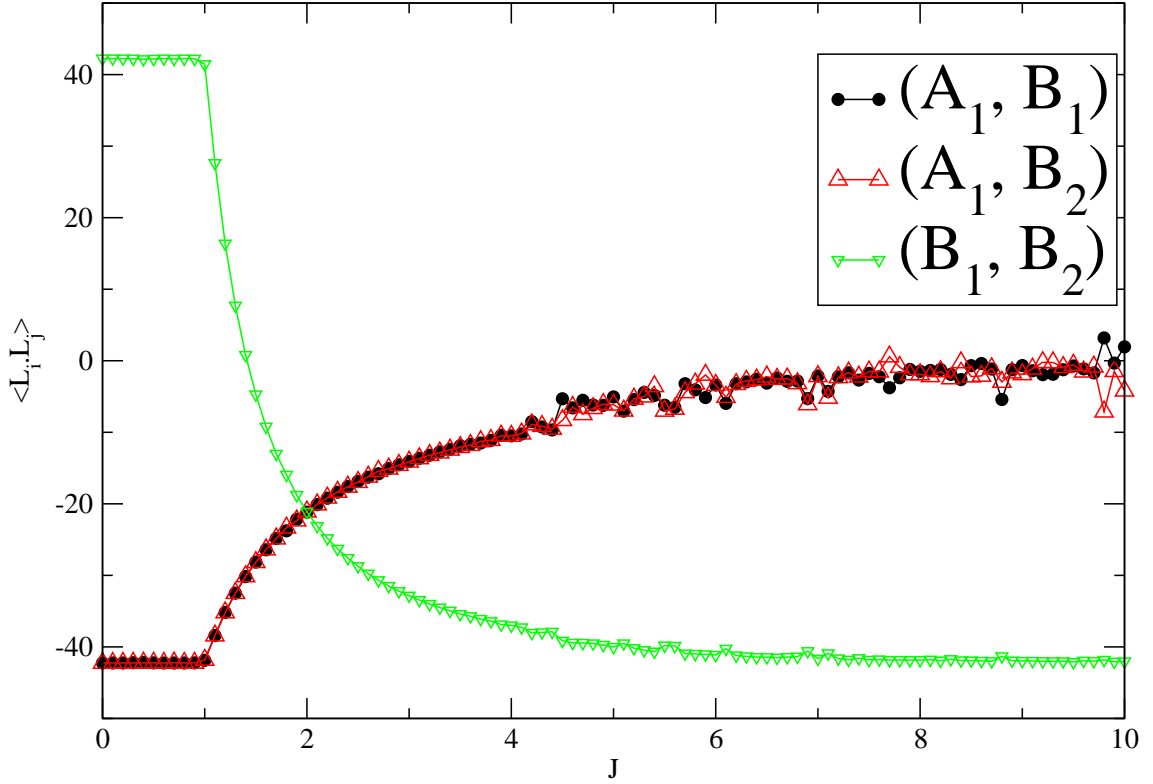


Figure 2.6: Two-point MF momentum products for frustration  $F_1$ . Here we show a choice of the parameters  $g = \alpha = 1$  with a Hilbert space truncated at  $\ell = 6.5$ . The momenta are scaled up to the highest  $\ell$ .

(we take  $n$  constant, which is about true for small  $\ell$ , as verified in the simulations, and whose value must be read off from the plots). We start off with the energy function for the frustration  $F_1$ , taking into account the cases  $M = 0$  and  $M = 1$ . So, for each case, up to a constant independent of  $\theta$ :

$$\begin{aligned} E_{(M=0)}(\theta) &= -2(1 + 4n^2) \cos \frac{\theta}{2} + \frac{J}{2}(1 + 4n^2) \cos \theta, \\ E_{(M=1)}(\theta) &= -2(1 - 4n + 4n^2) \cos \frac{\theta}{2} - 2n \cos \theta + \frac{J}{2}(1 + 4n^2) \cos \theta. \end{aligned} \quad (2.34)$$

Upon imposing the minimization conditions (relative to the unique parameter  $\theta$ ), we obtain: (i) for  $J < 1$  we have  $\theta = 0$ , which holds for both  $M = 0$  and  $M = 1$ ; (ii) for  $J > 1$ , we have  $\theta \neq 0$ , which in turn implies that  $J = \frac{1}{\cos \frac{\theta}{2}}$ , for  $M = 0$ , while  $J = \frac{(1-2n)^2 + 4n \cos \frac{\theta}{2}}{(1+4n^2) \cos \frac{\theta}{2}}$ , for  $M = 1$ . The momentum products are accordingly given by:

- for  $J < 1$ , and both  $M = 0$  and  $M = 1$ ,

$$\begin{aligned} \mathbf{L}_{A_1} \cdot \mathbf{L}_{B_{1,2}} &= -0.25, \\ \mathbf{L}_{B_1} \cdot \mathbf{L}_{B_2} &= +0.25. \end{aligned} \quad (2.35)$$

- for  $J > 1$ ,

$$\begin{aligned} \mathbf{L}_{A_1} \cdot \mathbf{L}_{B_{1,2}} &= -\frac{1}{4J}, \\ \mathbf{L}_{B_1} \cdot \mathbf{L}_{B_2} &= \frac{1}{2J^2} - \frac{1}{4}, \quad M = 0; \end{aligned} \quad (2.36)$$

$$\begin{aligned}\mathbf{L}_{A_1} \cdot \mathbf{L}_{B_{1,2}} &= -\frac{1}{4} \left( \frac{(1-2n)^2}{J(1+4n^2) - 4n} \right), \\ \mathbf{L}_{B_1} \cdot \mathbf{L}_{B_2} &= \frac{1}{4} \left( \frac{2(1-2n)^4}{[J(1+4n^2) - 4n]^2} - 1 \right), \quad M = 1.\end{aligned}\tag{2.37}$$

With respect to frustration F<sub>2</sub>, our present MF approach can only “sense” a repetition of the configuration of Fig. 2.7, in that we get additional terms to the energy functions above that are independent of  $\theta$  (and therefore vanish upon minimization), implying the same results for the dot products.

This classical description fully accounts for the momentum products in both frustration types for  $M = 0$ , including the nature of the phase transition at  $J = 1$ , as seen in Fig. 2.3 (a) and Fig. 2.4 (a) through the matching fit to the points of the numerical implementation for the rotors; for  $M = 1$ , this interpretation confirms the first-order transition at  $J = 1$  and offers hints at the expected behavior of these momentum products, were it not for the stray points, as can be seen in the diagrams of Fig. 2.3(c) and Fig. 2.4(c). In Eq. (2.37) we have used  $n = 0.34$ , that can be read off from the plots of  $\langle \hat{\mathbf{n}}^2 \rangle$ , which were not explicitly presented in this work. One might be misled to understand that a coupling  $M \neq 0$  always changes the transition to first order. This not the case for the system plotted in Fig. 2.8, where  $M = 1$  in all couplings, except for the frustation coupling which is allowed to vary. With a slight modification, the classical interpretation above assures us that the transition continues to be of second order and that the transition point is shifted to the right, i. e, the new transition point is approximately given by

$$J_t = 1 + \frac{nM}{1 + 4n^2}.\tag{2.38}$$

We have also detected other situations with ( $M \neq 0$ ) whose transition remains

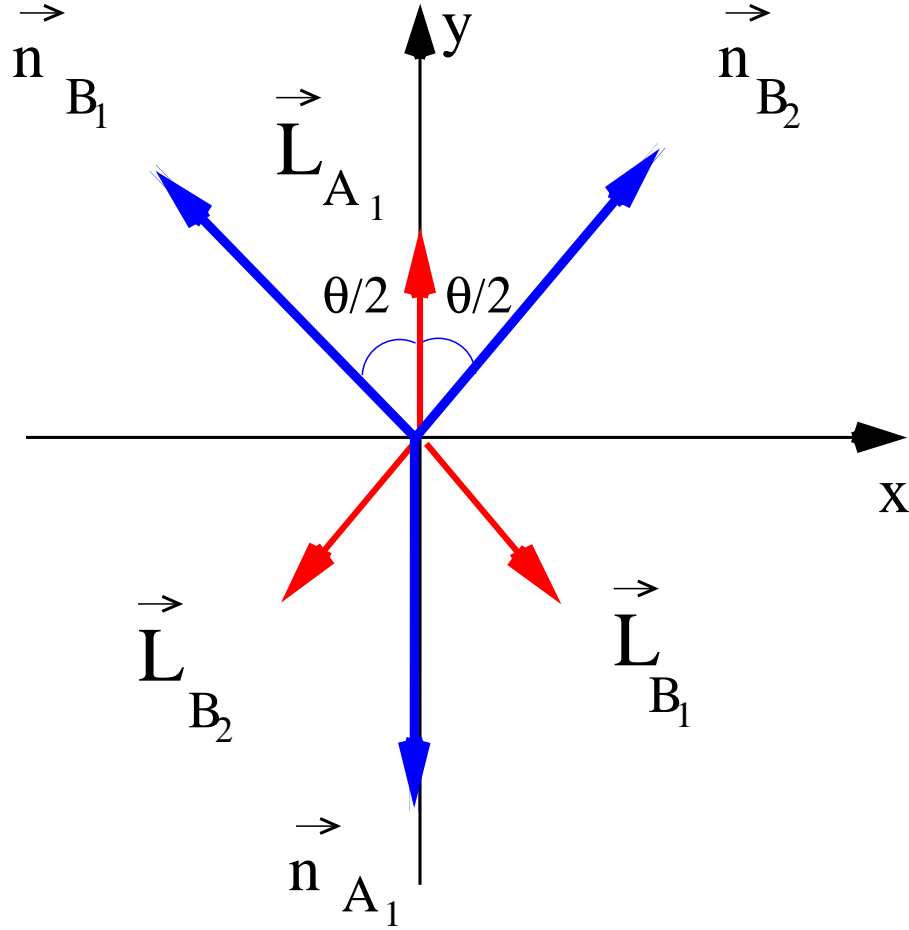


Figure 2.7: Classical vector configuration. The angle  $\theta$  is the unique order parameter.

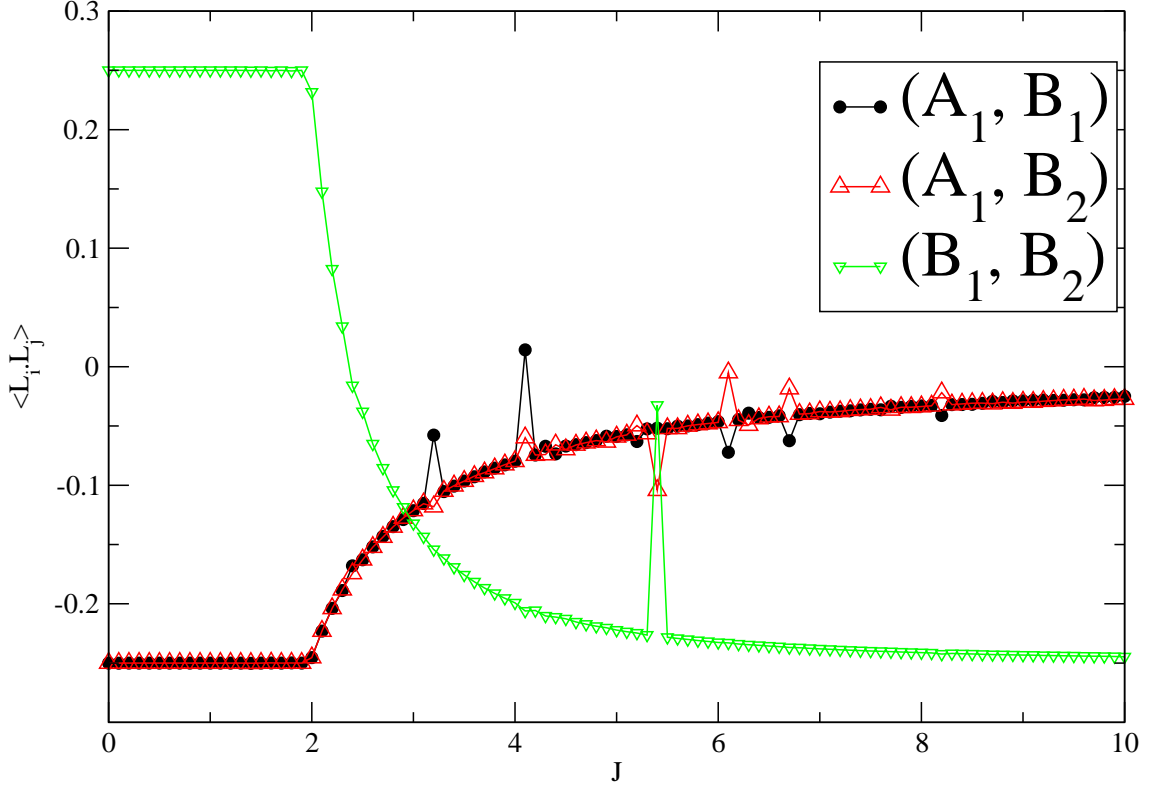


Figure 2.8: Two-point MF momentum products for frustration  $F_1$ . Here we show a choice of the parameters  $g = \alpha = 1$  with a Hilbert space truncated at  $\ell = 5.5$ .  $M = 10$  in the frustration coupling and  $M = 1$  elsewhere. The system behaves just like the one depicted in Fig. 2.3, but the transition takes place at  $J_t \approx 1.8$ , i.e., with a shift to the right hinted at by Eq. (2.38).

second order with no shift at all and whose transition changes to first order with a shift, all explainable in this classical framework.

In the following section we try a *more elaborate* MF technique on a double-cell structure, as a way to circumvent Eq. (2.31), as well as to get a direct evaluation of the intra- and intercell two-point correlations. For simplicity, we restrict ourselves to  $M = 0$ .

## 2.4 Quantum rotors on the AB<sub>2</sub> chain: the double-cell variational mean-field approach

Differently from the approach presented in Sec. 2.3, we build our trial Hamiltonian acting on the *global* space formed by the six sites of the double-cell structure made up of two contiguous unit cells, such as showed in Fig. 2.2, i.e., we build one *six-site* trial Hamiltonian acting, say, on the sites A<sub>1</sub>, A<sub>2</sub>, B<sub>1</sub>, B<sub>2</sub>, B<sub>3</sub>, and B<sub>4</sub>. In order to achieve that, we assigned to each site its own *local* vector subspace, and we then constructed our global space by forming the tensor product of these subspaces in one chosen order. Aiming at simplifying the equations below, when necessary, the *local* operator that acts on the quantum rotor located at site A<sub>1</sub>, for instance, is denoted by  $\hat{\mathbf{X}}_{A_1}$ , which may refer to either operator  $\hat{\mathbf{L}}$  or operator  $\hat{\mathbf{n}}$ . The *extended* operator on the same site was then defined by

$$\hat{\mathbf{X}}_{A_1}^* = \hat{\mathbf{X}}_{A_1} \otimes I_{A_2} \otimes I_{B_1} \otimes I_{B_2} \otimes I_{B_3} \otimes I_{B_4}, \quad (2.39)$$

where an order is implicitly chosen, and  $I$  stands for the identity operators (represented by the unit matrix) acting on the respective site subspaces. For a dot



product, for example, between operators acting on sites A<sub>1</sub> and B<sub>2</sub>, we have

$$\begin{aligned}
 \hat{\mathbf{X}}_{A_1}^* \cdot \hat{\mathbf{X}}_{B_2}^* &= (\hat{X}_{A_1}^*)_x (\hat{X}_{B_2}^*)_x + (\hat{X}_{A_1}^*)_y (\hat{X}_{B_2}^*)_y + (\hat{X}_{A_1}^*)_z (\hat{X}_{B_2}^*)_z \\
 &= \sum_{i=x,y,z} [(\hat{\mathbf{X}}_{A_1})_i \otimes I_{A_2} \otimes \cdots \otimes I_{B_4}] [I_{A_1} \otimes \cdots \otimes (\hat{\mathbf{X}}_{B_2})_i \otimes \cdots \otimes I_{B_4}] \\
 &= \sum_{i=x,y,z} [(\hat{\mathbf{X}}_{A_1})_i \otimes I_{A_2} \otimes I_{B_1} \otimes (\hat{\mathbf{X}}_{B_2})_i \otimes I_{B_3} \otimes I_{B_4}], \tag{2.40}
 \end{aligned}$$

and here the  $(\hat{\mathbf{X}}_{site})_i$ , ( $i = x, y, z$ ), is represented by the matrix formed of the matrix elements given in Appendix A.1, which were thoroughly deduced for both operators  $\hat{\mathbf{n}}$  and  $\hat{\mathbf{L}}$ . We see that the ordinary product of extended operators is indeed a tensor product of local operators. More appropriately speaking, the matrix operation above is realized through the Kronecker product of matrices as opposed to the ordinary product. A tensor product as is commonly referred to in the mathematical literature occurs between two vectors and has as result a matrix. From now on, in order to unburden the notation, we will make do with the star superscript in the equations and relations with extended operators in the rest of this section.

We now write down the trial Hamiltonian acting on a given double-cell structure for frustration F<sub>1</sub>:

$$\hat{H}_{trial} = \hat{H}_{trial}^{(1)} + \hat{H}_{trial}^{(2)} + \hat{H}_{trial}^{(3)}. \tag{2.41}$$

The first term (the kinetic energy term plus effective fields) is given by

$$\hat{H}_{trial}^{(1)} = \sum_i \left[ \frac{g}{2} \left( \hat{\mathbf{L}}_i^2 + \alpha (\hat{\mathbf{L}}_i^2)^2 \right) + \mathbf{N}_i \cdot \hat{\mathbf{n}}_i + \mathbf{h}_i \cdot \hat{\mathbf{L}}_i \right], \tag{2.42}$$

where the index  $i$  goes over the sites A<sub>1</sub>, A<sub>2</sub>, B<sub>1</sub>, B<sub>2</sub>, B<sub>3</sub>, and B<sub>4</sub>;  $\mathbf{N}_i$  and  $\mathbf{h}_i$  being the effective fields (variational c-numbers) due to the rest of the system (which plays

the role of a bath), and acting on each site  $i$  of the double-cell cluster. The next term (first neighbors or bonds) reads

$$\begin{aligned} \hat{H}_{trial}^{(2)} = \sum_{\hat{\mathbf{X}}=\hat{\mathbf{n}},\hat{\mathbf{L}}} [ & (\hat{\mathbf{X}}_{A_1} + \hat{\mathbf{X}}_{A_2}) \cdot (\hat{\mathbf{X}}_{B_1} + \hat{\mathbf{X}}_{B_2}) \\ & + \hat{\mathbf{X}}_{A_2} \cdot (\hat{\mathbf{X}}_{B_3} + \hat{\mathbf{X}}_{B_4})], \end{aligned} \quad (2.43)$$

while the last one (frustration interaction) is written as

$$\hat{H}_{trial}^{(3)} = J \sum_{\hat{\mathbf{X}}=\hat{\mathbf{n}},\hat{\mathbf{L}}} [(\hat{\mathbf{X}}_{B_1} \cdot \hat{\mathbf{X}}_{B_2}) + (\hat{\mathbf{X}}_{B_3} \cdot \hat{\mathbf{X}}_{B_4})], \quad (2.44)$$

where in the first term we opted to use the explicit operators, i.e.,  $\hat{\mathbf{L}}_i$  and  $\hat{\mathbf{n}}_i$ . For frustration F<sub>2</sub>, the following term (intercell frustration interaction) must be added to Eq. (2.41):

$$\hat{H}_{trial}^{(4)} = J \sum_{\hat{\mathbf{X}}=\hat{\mathbf{n}},\hat{\mathbf{L}}} [(\hat{\mathbf{X}}_{A_1} \cdot \hat{\mathbf{X}}_{A_2} + \hat{\mathbf{X}}_{B_1} \cdot \hat{\mathbf{X}}_{B_3} + \hat{\mathbf{X}}_{B_2} \cdot \hat{\mathbf{X}}_{B_4})]. \quad (2.45)$$

The direct application of Eq. (2.27) yields for frustration F<sub>1</sub> the following expression for the *double-cell* variational MF energy  $E_{mf}^{(F1)} \equiv E_{mf}^{(F1)}(g, \alpha, J)$ , where the equals sign implies that minimization with respect to the variational fields has already been carried through:

$$\begin{aligned} E_{mf}^{(F1)} = E_0 + 2 \sum_{\hat{\mathbf{X}}=\hat{\mathbf{n}},\hat{\mathbf{L}}} & \langle \hat{\mathbf{X}}_{A_1} \rangle_0 \cdot (\langle \hat{\mathbf{X}}_{B_3} \rangle_0 + \langle \hat{\mathbf{X}}_{B_4} \rangle_0) \\ & - \sum_i (\mathbf{N}_i \cdot \langle \hat{\mathbf{n}}_i \rangle_0 + \mathbf{h}_i \cdot \langle \hat{\mathbf{L}}_i \rangle_0), \end{aligned} \quad (2.46)$$

where,  $E_0$  represents the ground-state energy of  $\hat{H}_{trial}$  and, as before, the index  $i$

visits the sites A<sub>1</sub>, A<sub>2</sub>, B<sub>1</sub>, B<sub>2</sub>, B<sub>3</sub>, and B<sub>4</sub>.

For frustration F<sub>2</sub>, we get analogously  $E_{mf}^{(F_2)} \equiv E_{mf}^{(F_2)}(g, \alpha, J)$ :

$$\begin{aligned}
 E_{mf}^{(F_2)} &= E_0 + 2 \sum_{\hat{\mathbf{X}}=\hat{\mathbf{n}}, \hat{\mathbf{L}}} \langle \hat{\mathbf{X}}_{A_1} \rangle_0 \cdot (\langle \hat{\mathbf{X}}_{B_3} \rangle_0 + \langle \hat{\mathbf{X}}_{B_4} \rangle_0) \\
 &\quad + 2J \sum_{\hat{\mathbf{X}}=\hat{\mathbf{n}}, \hat{\mathbf{L}}} (\langle \hat{\mathbf{X}}_{A_1} \rangle_0 \cdot \langle \hat{\mathbf{X}}_{A_2} \rangle_0 + \\
 &\quad \langle \hat{\mathbf{X}}_{B_1} \rangle_0 \cdot \langle \hat{\mathbf{X}}_{B_3} \rangle_0 + \langle \hat{\mathbf{X}}_{B_2} \rangle_0 \cdot \langle \hat{\mathbf{X}}_{B_4} \rangle_0) \\
 &\quad - \sum_i (\mathbf{N}_i \cdot \langle \hat{\mathbf{n}}_i \rangle_0 + \mathbf{h}_i \cdot \langle \hat{\mathbf{L}}_i \rangle_0).
 \end{aligned} \tag{2.47}$$

Now, a given eigenfunction of  $\hat{H}_{trial}$  may not necessarily be a tensor product of the eigenfunctions of the respective site subspaces, differently from the case in Sec. 2.3, so that, for example,

$$\langle \Psi_0 | \hat{\mathbf{X}}_{A_1} \cdot \hat{\mathbf{X}}_{B_2} | \Psi_0 \rangle \neq \langle \Psi_0 | \hat{\mathbf{X}}_{A_1} | \Psi_0 \rangle \cdot \langle \Psi_0 | \hat{\mathbf{X}}_{B_2} | \Psi_0 \rangle, \tag{2.48}$$

where  $|\Psi_0\rangle$  designates the ground-state wavefunction of  $H_{trial}$ . It is an important aspect in this approach, which differs from the standard MF result given by Eq. (2.31). Thus, in principle, taking advantage of the available capability of diagonalizing more complex operators (trial Hamiltonians), we can produce more reliable cluster variational MF theories.

The dimension of the global space is  $d^6$ , where  $d$  is the dimension of the local subspace. Therefore, due to computational implementability, this fact prompted us to limit the size of the Hilbert space by deploying rotors with maximum  $\ell = 3/2$ .

An observation about the value of  $g$  is in order. On studying frustration  $F_1$ , when we had set  $g = 10$ , as in the preceding section, we verified that the momentum

correlation  $\langle \hat{\mathbf{L}}_{A_1} \cdot \hat{\mathbf{L}}_{A_2} \rangle$  remained pegged at 0.25, even after the transition at  $J = 2$ , which turns out not to be true (see below). In solving this problem, we resorted in this section to a higher value of  $g$  (namely,  $g = 1000$ ), which then inhibited more strongly the appearance of disturbing states; however one should notice that if much greater values of  $g$  are employed, the kinetic energy becomes overwhelmingly dominant, and as a consequence, small changes in the correlations tend to go unnoticed.

As before, we concentrated on the relevant quantities that can provide the information needed for the physical interpretation of the problem: namely, *the MF energy*, the *expectation value of the total angular momentum*, and the *momentum correlations*. The expectation value of the total angular momentum per unit cell was calculated according to the formula  $|\langle \mathbf{L} \rangle|^2 = 1/2 \sum_{\mu} \langle L_{\mu}^2 \rangle$ , where  $L_{\mu}$  ( $\mu = x, y, z$ ) is the respective resultant component (component sum over all the six sites of the double-cell structure).

### 2.4.1 Frustration F<sub>1</sub>

In order to facilitate comparison between the QR results and those of the spin-1/2 counterpart with the same type of frustration, we present in Fig. 2.9 the phases obtained for the spin-1/2 diamond chain[57]. The Lieb-Mattis[83] ferrimagnetic phase (FERRI) appears when  $J < 0.909$  ( $J$  is also used to indicate the frustration control parameter for the spin system). In the tetramer-dimer (TD) phase, which ensues when  $0.909 < J < 2$ , the state is precisely the regular array of singlet tetramers (the closed loop encompasses four spins, in which the B sites form a triplet pair, and the spins on the A sites oppose those on the B sites, so that zero total spin takes place), and singlet dimers (two spins within the elliptical contour) as shown in

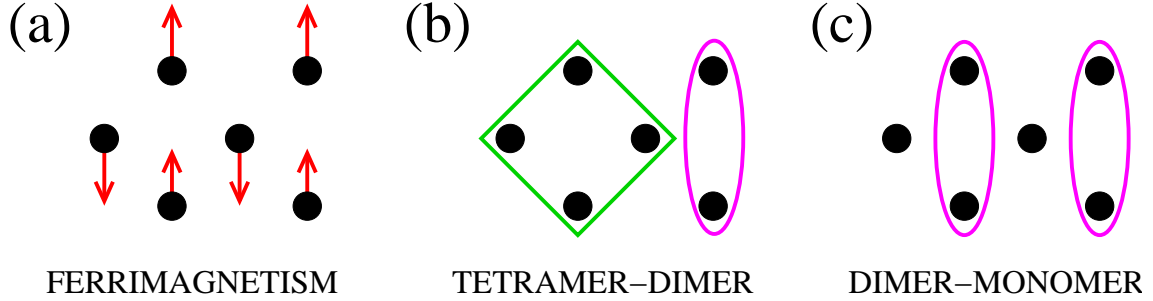


Figure 2.9: Illustration of the ground states found for the spin-1/2 diamond chain[57] as  $J$  is increased from 0. (a) The ferrimagnetic (FERRI) state. (b) The tetramer-dimer (TD) state, where rectangles represent singlet tetramers and ellipses singlet dimers. (c) The dimer-monomer (DM) state. There are two first-order phase transitions: at  $J = 0.909$  (FERRI/TD) and  $J = 2$  (TD/DM).

Fig. 2.9 (b). Finally, the dimer-monomer (DM) state is shown in Fig. 2.9 (c) and sets in when  $J > 2$ ; it is composed of the regular array of singlet dimers and free spins, and vanishing total spin is also expected. Because of the free spins, the DM state is macroscopically  $2^{N/3}$ -fold degenerate for a chain with  $N$  sites. Furthermore, both transitions are of first order.

In order to allow a direct comparison with our MF results for quantum rotors, we have solved the spin-1/2 diamond chain (AB<sub>2</sub> chain with frustration between spins at sites B of the same unit cell) for sizes up to 28 sites, using the ED procedure with open boundary conditions. The results are displayed as follows: the relevant correlations are represented by the curves plotted in Fig. 2.10; in Fig. 2.11 (a) and (b) we plotted respectively the energy and total-spin curves (normalized by the Lieb-Mattis value [83]).

Examination of the correlation plots show clear correspondence with the phases exhibited in Fig. 2.9. The phase FERRI is characterized by the following correlations:  $\langle \hat{\mathbf{S}}_{B_1} \cdot \hat{\mathbf{S}}_{B_2} \rangle = \langle \hat{\mathbf{S}}_{B_3} \cdot \hat{\mathbf{S}}_{B_4} \rangle = 0.25$ ,  $\langle \hat{\mathbf{S}}_{B_1} \cdot \hat{\mathbf{S}}_{B_3} \rangle = 0.21$ ,  $\langle \hat{\mathbf{S}}_{A_1} \cdot \hat{\mathbf{S}}_{A_2} \rangle =$

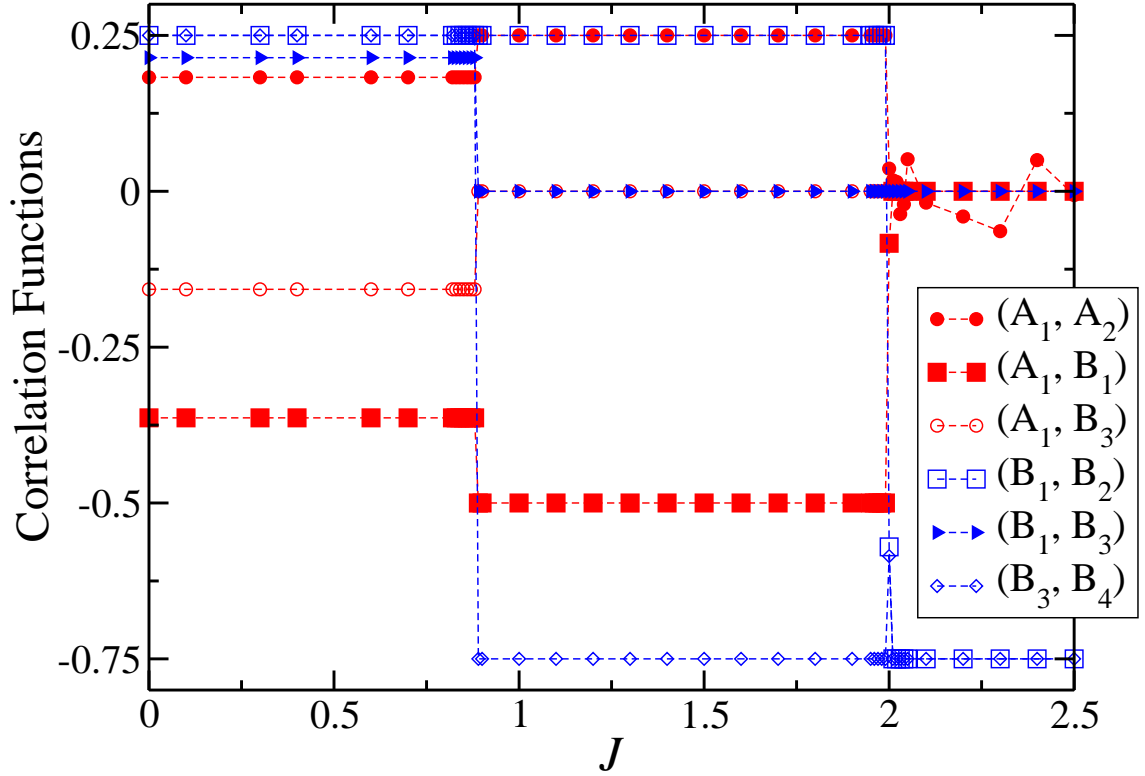


Figure 2.10: Spin-1/2 diamond chain: ED results for the correlation functions between spins at a central cluster of a system with 28 sites. Dashed lines are guides to the eye.

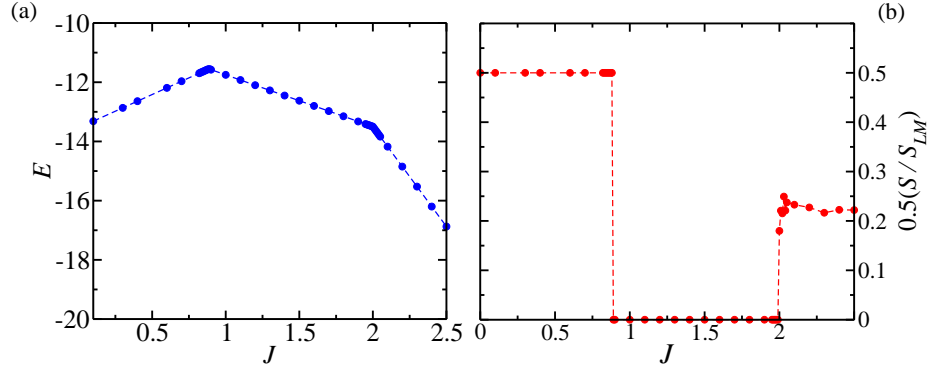


Figure 2.11: Spin-1/2 diamond chain: ED results for the (a) average ground-state energy and (b) rescaled total spin of a system with 28 sites. Phase transitions occur at  $J = 0.88$  and  $J = 2.0$ , both of first order. Dashed lines are guides to the eye.

0.18,  $\langle \hat{\mathbf{S}}_{A_1} \cdot \hat{\mathbf{S}}_{B_3} \rangle = -0.15$ ,  $\langle \hat{\mathbf{S}}_{A_1} \cdot \hat{\mathbf{S}}_{B_1} \rangle = -0.36$ . The total spin per unit cell in Fig. 2.11 (b) shows the Lieb-Mattis value of 0.5 throughout. The transition to the intermediate phase TD then occurs at  $J = 0.88$ , very close to the estimated value for the infinite chain [57]:  $J = 0.909$ . We note that in this phase the chain breaks up into smaller units - tetramers and dimers - and quantum fluctuations within each unit do not affect the spin correlations. Hence the correlations are just those calculated for the TD configuration of spins in Fig. 2.9 (b):  $\langle \hat{\mathbf{S}}_{A_1} \cdot \hat{\mathbf{S}}_{A_2} \rangle = \langle \hat{\mathbf{S}}_{B_1} \cdot \hat{\mathbf{S}}_{B_2} \rangle = 0.25$  (triplets),  $\langle \hat{\mathbf{S}}_{B_3} \cdot \hat{\mathbf{S}}_{B_4} \rangle = -0.75$  (singlets),  $\langle \hat{\mathbf{S}}_{A_1} \cdot \hat{\mathbf{S}}_{B_1} \rangle = -0.5$ , the other correlations being zero. With increasing  $J$  though, quantum fluctuations become strong enough to disrupt the tetramer unit and a new transition to the DM phase happens at  $J = 2$ , this point being independent of size because of the chain breakup. In this phase correlation  $\langle \hat{\mathbf{S}}_{A_1} \cdot \hat{\mathbf{S}}_{A_2} \rangle$  has varying nonzero values due to finite size effects, and does not vanish as should be expected in the thermodynamic limit. On the other hand, the B spins, which are interlocked in singlet units, are totally unaffected. This phase, depicted in Fig. 2.9 (c), shows the final chain breakup as the

tetramer gives way to two monomer units and another dimer, clearly indicated by the correlations in Fig. 2.10 ( $J \geq 2$ ). The energy curve in Fig. 2.11 (a) exhibits cusps at the transition points, typical of a first-order nature, also verified through the discontinuities of the correlations at these points. The total spin per unit cell in Fig. 2.11 (b) corroborates the above phase description; however in the last phase the apparent nonzero value is a finite-size effect.

Finally, getting down to the QR AB<sub>2</sub> chain, we display our variational MF numerical results in Fig. 2.12 (momentum correlations) and Fig. 2.13 (energy and total angular momentum) and we proceed to a comparative examination with respect to the preceding spin results. A blow-by-blow confrontation of the correlations in both Fig. 2.10 and Fig. 2.12 shows that the double-cell variational MF approach is able to reproduce the three phases exhibited in Ref. [57], namely, the FERRI, TD, and DM phases. In the FERRI phase, quantum fluctuations appear to be equally important, causing the same correlations to deviate somewhat from calculated results for stiff momenta. A closer examination shows that, up to two decimal digits, we have same correlations for  $\langle \hat{\mathbf{L}}_{B_1} \cdot \hat{\mathbf{L}}_{B_2} \rangle = \langle \hat{\mathbf{L}}_{B_3} \cdot \hat{\mathbf{L}}_{B_4} \rangle = 0.25$ , but slightly different correlations, namely:  $\langle \hat{\mathbf{L}}_{A_1} \cdot \hat{\mathbf{L}}_{A_2} \rangle = 0.22$ ,  $\langle \hat{\mathbf{L}}_{A_1} \cdot \hat{\mathbf{L}}_{B_1} \rangle = 0.46$ ,  $\langle \hat{\mathbf{L}}_{A_1} \cdot \hat{\mathbf{L}}_{B_3} \rangle = 0.20$ , and  $\langle \hat{\mathbf{L}}_{B_1} \cdot \hat{\mathbf{L}}_{B_3} \rangle = 0.22$ , for the rotor system, which should be compared with  $\langle \hat{\mathbf{S}}_{A_1} \cdot \hat{\mathbf{S}}_{A_2} \rangle = 0.18$ ,  $\langle \hat{\mathbf{S}}_{A_1} \cdot \hat{\mathbf{S}}_{B_1} \rangle = 0.36$ ,  $\langle \hat{\mathbf{S}}_{A_1} \cdot \hat{\mathbf{S}}_{B_3} \rangle = 0.16$ , and  $\langle \hat{\mathbf{S}}_{B_1} \cdot \hat{\mathbf{S}}_{B_3} \rangle = 0.21$ , for the spin system. Phase transitions occur at  $J = 0.68$  and  $J = 2$ , evidently of first order; in the first transition we have a lesser value ( $J = 0.68$ ) than the Lanczos result for the 28-site spin-1/2 chain ( $J = 0.88$ ), and that of Ref. [57] ( $J = 0.909$ ). The momentum and spin correlations match one another, respectively, in both phases: in the DM phase, correlation  $\langle \hat{\mathbf{L}}_{A_1} \cdot \hat{\mathbf{L}}_{A_2} \rangle$  shows also an erratic behavior similar to its spin counterpart, in other words, finite size effects are



also at play. The minor differences in correlations in the FERRI phase, as well as in the first transition point do not constitute a fundamental discrepancy between the respective phase diagrams, which are endowed with the same topological features. In Fig. 2.13 (a) the cusps in the MF energy at  $J = 0.68$  and  $J = 2$  also bespeak the occurrence of these first-order transitions. Comparing the total momentum in Fig. 2.13 (b) with the total spin in Fig. 2.11 (b), we observe similar results for the ED calculations for the spin model, including finite-size effects in the last phase.

It is instructing to study the QR system regarding the average singlet density per unit cell of the B momenta [59], which in our case (*double-cell* cluster) is calculated directly using

$$\langle \eta \rangle = \frac{1}{4} - \frac{1}{2}(\langle \hat{\mathbf{L}}_{B_1} \cdot \hat{\mathbf{L}}_{B_2} \rangle + \langle \hat{\mathbf{L}}_{B_3} \cdot \hat{\mathbf{L}}_{B_4} \rangle), \quad (2.49)$$

and which is displayed in Fig. 2.14. These results permit a direct comparison with the phase diagram of Fig. 2.9, as far as the buildup of singlet pairs out of B momenta is concerned. As is the case for spins, size effects are not important here, so that one perceives that the number of singlets is very clearly a quantized quantity within each phase.

### 2.4.2 Frustration F<sub>2</sub>

Before getting down to quantum rotors, we describe succinctly existent results[59] for the spin-1/2 AB<sub>2</sub> chain with the same frustration F<sub>2</sub> pattern. The rich phase diagram of the model was studied through DMRG, ED, and a hard-core boson model. The phase diagram thus obtained presented three transition points. The first one is continuous and occurs at  $J = 0.34$  between the Lieb-Mattis ferrimagnetic phase

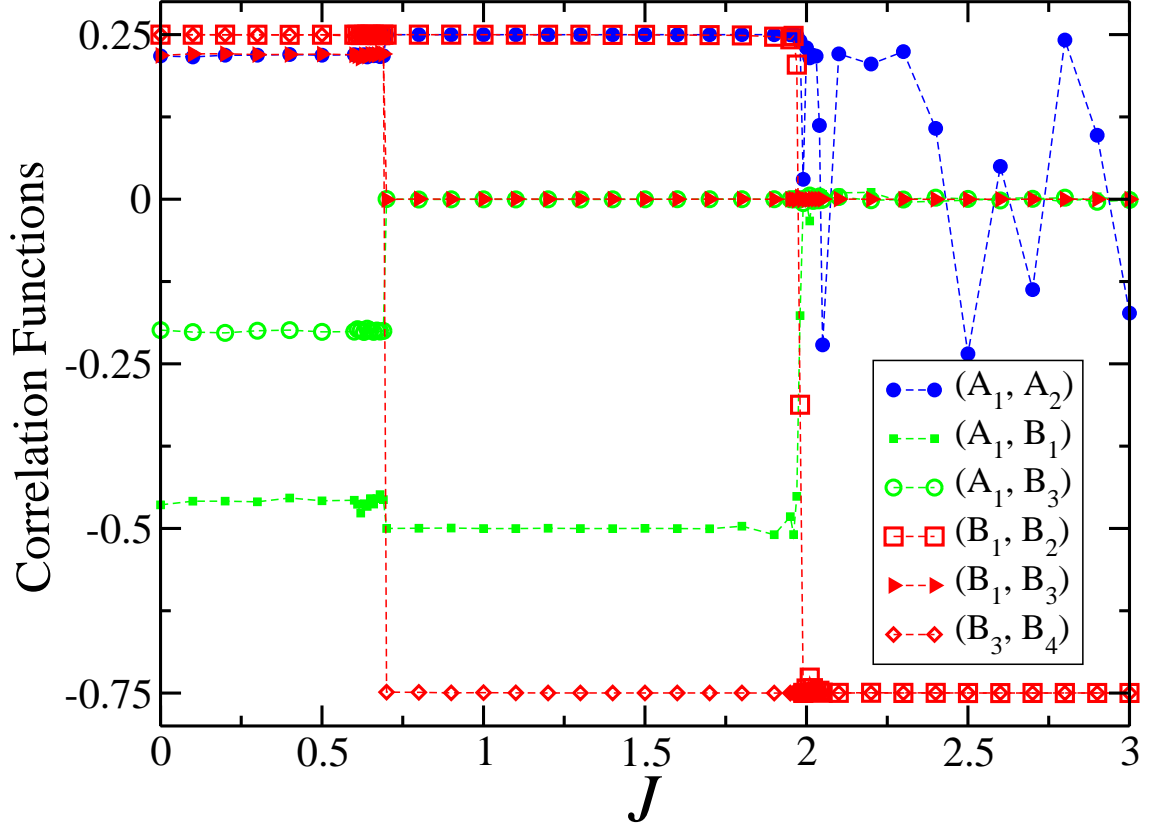


Figure 2.12: QR momentum correlations calculated by using the double-cell variational MF approach for frustration  $F_1$ . One notices the phase sequence  $FERRI \leftrightarrow TD \leftrightarrow DM$ , with first-order transitions at  $J = 0.68$  and  $J = 2$ . Dashed lines are guides to the eye.

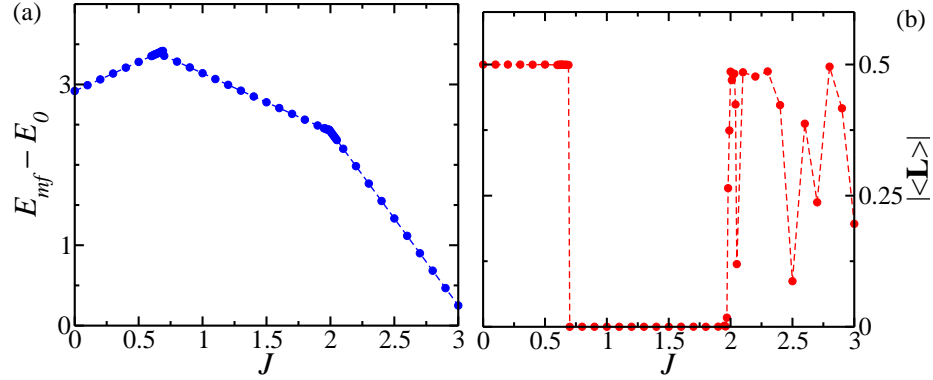


Figure 2.13: Quantum rotors by using the double-cell variational MF results for frustration F<sub>1</sub>: (a) the energy plot ( $E_0 = 1962$ ) shows cusps at the first-order transition points  $J = 0.68$  and  $J = 2.0$ ; (b) expectation value of the total angular momentum per unit cell. Dashed lines are guides to the eye.

(F1) and a ferrimagnetic phase (F2) characterized by the condensation of the singlet component of the spins at the sites B<sub>1</sub> and B<sub>2</sub> of the same unit cell, with transverse critical antiferromagnetic correlations. At  $J = 0.445$ , a first-order transition to a phase characterized by spiral and predominantly AF correlations (*singlet spiral*) takes place. The number of singlets in the lattice is quantized before this transition, but is a continuous quantity afterwards, and can be envisioned by measuring the singlet density. Further, a continuous chain-ladder decoupling transition at  $J = 0.91$  is observed. Above this value, the A spins present critical AF correlations following the asymptotic behavior observed in a linear chain, with power-law decay, while the ladder of B spins are short-range correlated with a finite correlation length, whose value is  $J$ -dependent, and nears the two-legged-ladder configuration (*decoupled chain ladder*).

As far as quantum rotors are concerned, the examination of the momentum correlations in Fig. 2.15 reveals that the system starts out with the FERRI phase

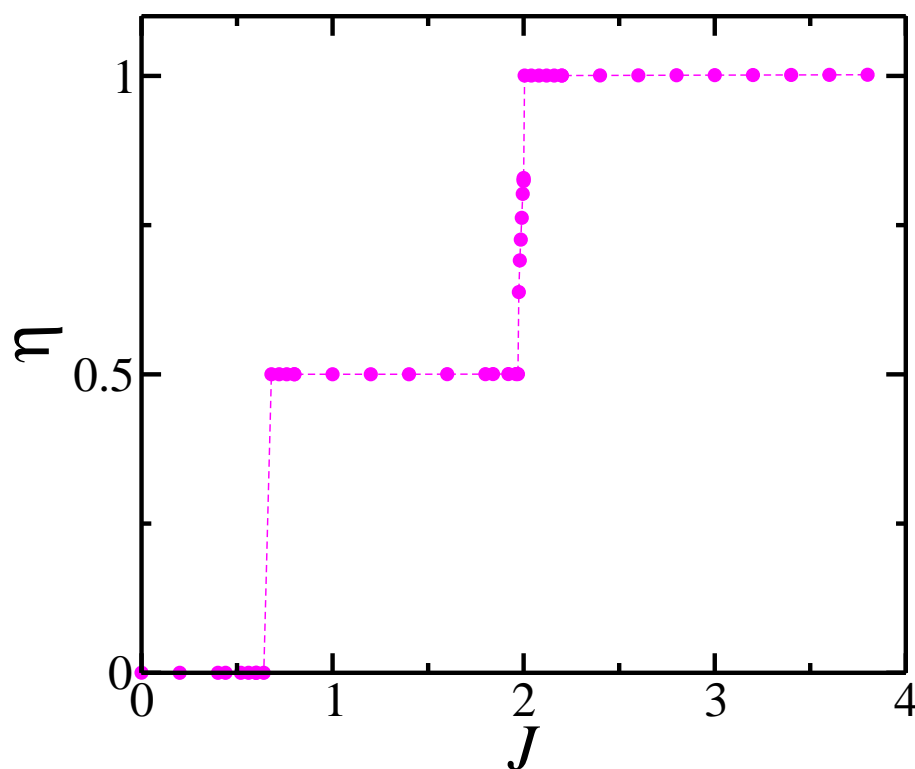


Figure 2.14: Quantum rotors with frustration F<sub>1</sub>: average singlet density per unit cell for the momenta of the B sites at the same unit cell. One can make out the three phases: FERRI, TD, and DM, as well as pertinent transitions. Dashed lines are guides to the eye.

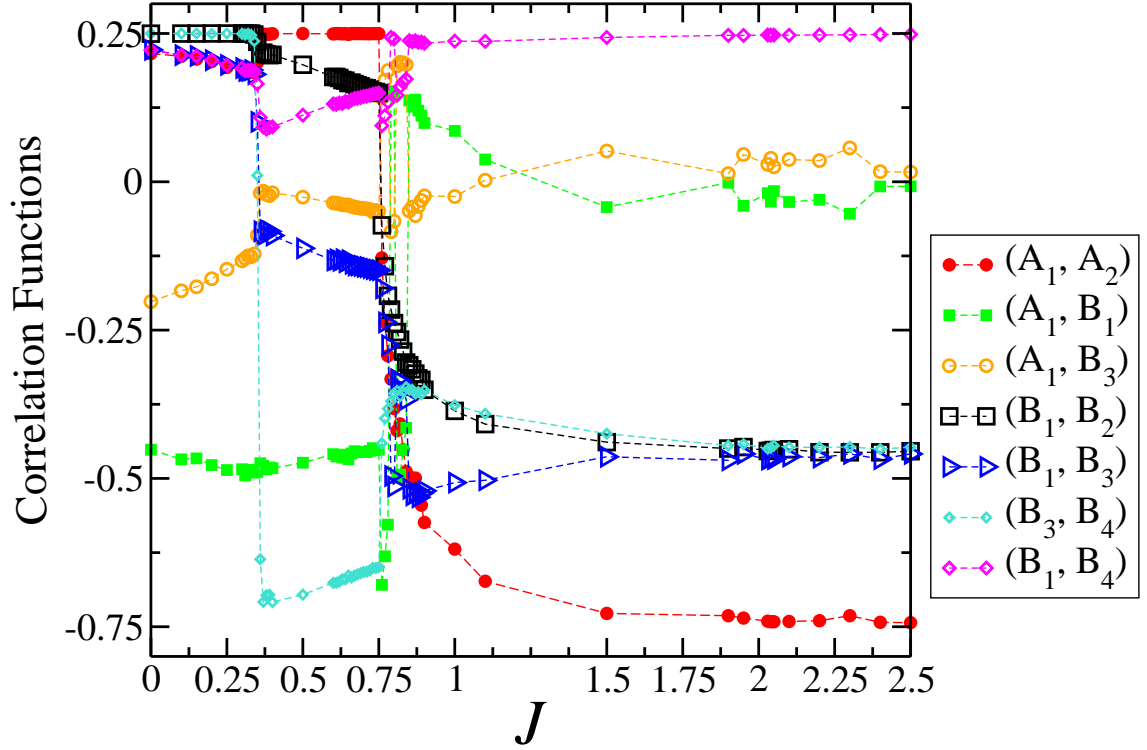


Figure 2.15: QR momentum correlations calculated by using the double-cell variational MF approach for frustration  $F_2$ . One can distinguish three major phases: FERRI, CANTED, and the decoupled AF chain ladder system, with transitions occurring around  $J = 0.35$  and  $J = 0.75$ . Dashed lines are guides to the eye.

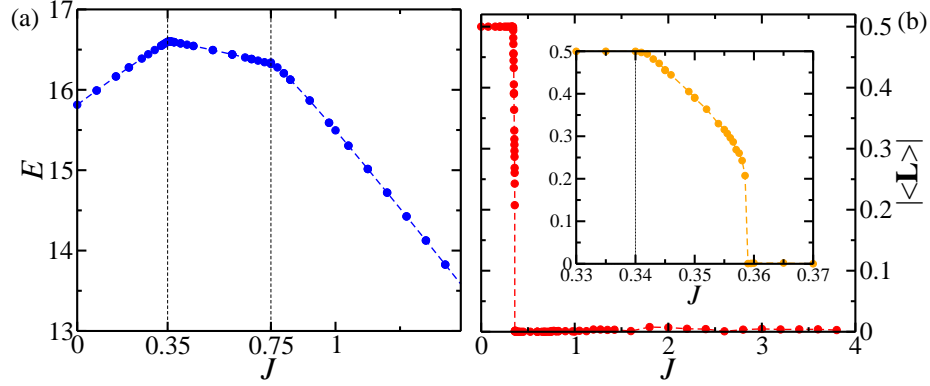


Figure 2.16: Quantum rotors by using the double-cell variational MF results for frustration F<sub>2</sub>: (a) energy and (b) expectation value of the total angular momentum per unit cell. The inset shows details of the phase transition around  $J = 0.35$ . Dashed lines are guides to the eye.

which is the counterpart of phase F1 of the spin system studied in Ref. [59]. The double-cell variational MF energy plotted in Fig. 2.16 (a) exhibits a pattern quite similar to that of frustration F<sub>1</sub>, shown in Fig. 2.11 (a). But resorting to Fig. 2.15 with the help of Fig. 2.16 (b) (total average momentum per unit cell), we can clear up the picture: in fact, at  $J = 0.34$  it is reasonable to think that a second-order transition takes place giving rise to a narrow transient phase that corresponds to the phase F2 (condensation of singlet components of the spins at the sites B of the same unit cell) for the spin system and is best visualized through the inset in the latter figure, which shows the behavior of the total angular momentum. In this phase the momenta of the A sites keep their ferromagnetic configuration ( $\langle \hat{\mathbf{L}}_{A_1} \cdot \hat{\mathbf{L}}_{A_2} \rangle = 0.25$ ) while the B momenta conform to a magnetic canted configuration. A first-order transition follows at  $J \approx 0.36$  to a new state that should correspond to the phase *singlet spiral* of the respective spin system. With respect to the momenta at the A sites, the ferromagnetic configuration also prevails in this phase. The

total angular momentum of the A sublattice exactly counterbalances that of the B sublattice, so that, as it happens for the spin system, a vanishing expectation value of the total angular momentum (spin) per unit cell occurs. Furthermore, upon inspecting the B correlations in Fig. 2.15, this phase appears here to have also a semiclassical canted configuration, hence the name CANTED that we use to designate this QR phase together with the previous one. In the same manner for the spin system [59], the additional intercell interactions produce nonquantized values of the B momenta (see, for example, correlation  $\langle \hat{\mathbf{L}}_{B_1} \cdot \hat{\mathbf{L}}_{B_3} \rangle$ ). The nonquantization verified in the spin system, which is a coherent superposition of singlet and triplet configurations, may rather be seen as manifestation of the symmetry-breaking of the invariance of the Hamiltonian under interchange of the B sites in the same cell brought about by the additional frustration. This is also clearly verified in the QR system. In the absence of the additional frustration, as is the case for frustration  $F_1$  (Fig. 2.2 (a)), this symmetry stays unscathed, so that there is no singlet-triplet superposition: we have either a singlet or a triplet configuration per cell, but never both simultaneously, which was already verified for both spin and QR systems. Finally, as seen in Fig. 2.15, at  $J = 0.75$ , quantum fluctuations bring the sudden decoupling of the chain through another phase transition with first-order characteristics (in the spin system the transition is second-order), and the system settles into an antiferromagnetic (AF) phase, also marked by a vanishing expectation value of the total angular momentum per unit cell, as shown in Fig. 2.16 (b). In this phase the frustrated AB<sub>2</sub> chain splits into two decoupled chains, namely, an AF linear chain ( $\langle \hat{\mathbf{L}}_{A_1} \cdot \hat{\mathbf{L}}_{A_2} \rangle = -0.75$ ) and an AF two-legged ladder ( $\langle \hat{\mathbf{L}}_{B_1} \cdot \hat{\mathbf{L}}_{B_2} \rangle = \langle \hat{\mathbf{L}}_{B_1} \cdot \hat{\mathbf{L}}_{B_3} \rangle = \langle \hat{\mathbf{L}}_{B_1} \cdot \hat{\mathbf{L}}_{B_4} \rangle = -0.5$  and  $\langle \hat{\mathbf{L}}_{B_1} \cdot \hat{\mathbf{L}}_{B_4} \rangle = 0.25$ ); the decoupling is seen through  $\langle \hat{\mathbf{L}}_{A_1} \cdot \hat{\mathbf{L}}_{B_{3,4}} \rangle \cong 0$ . In Fig. 2.17, we show a pictorial representation of the

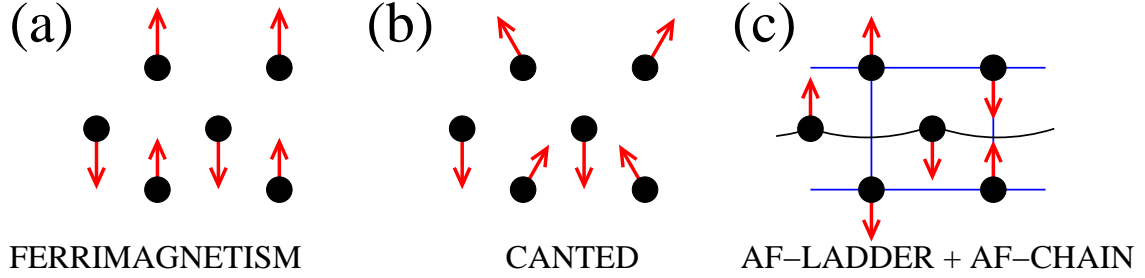


Figure 2.17: Illustration of the major QR ground states for frustration  $F_2$ : (a) FERRI; (b) CANTED; (c) AF, which is composed of two decoupled 1D systems: a linear chain (A sites) and the two-legged ladder (B sites).

the three major phases FERRI, CANTED and AF. With respect to this AF phase, our QR simulations evidently shed no light onto the criticality and short-rangedness of the linear and two-legged ladder chains, respectively. This phase corresponds to the *decoupled chain-ladder* system, which in turn has a vanishing total spin. The first-order transition at  $J = 0.75$  may rather be seen as a manifestation of finite-size effects of our two-cell approach: the absence of many intermediate states preclude a smooth transition.

The average singlet density for this frustration pattern is shown in Fig. 2.18: the singlet number is quantized (except for the narrow interval around  $J = 0.36$ , until the frustration reaches the value  $J = 0.75$ , wherefrom the singlet number goes on nonquantized. We see that the QR system exhibits a four-phase pattern quite similar to that of the respective spin system, with the nature of all but the last phase transitions being similar in both systems. With respect to singlet quantization, we find agreement in the first and last phases (where singlet densities 0 and 0.7 are observed); in the intermediate phases no match is observed and again we impute this naturally to finite size effects of our two-cell approach, which hinder a discrete one-



by-one singlet condensation. Also, because of the additional intercell frustration, it was not possible to form isolated singlet configurations, differently from frustration F<sub>1</sub>.

In what follows, we provide a more detailed comparison between QR MF results and the spin-1/2 chain, in its quantum and classical versions. The phase diagram initially described of the spin-1/2 chain from Ref. [59] is summarized in Fig. 2.19 (a). The spiral phase can be exposed in a clear fashion through the pitch angle  $q$  obtained from the magnetic structure factor defined as

$$F(q) = \frac{1}{2N} \sum_{j,k} \langle \hat{\mathbf{S}}_j \cdot \hat{\mathbf{S}}_k \rangle e^{iq(j-k)}, \quad (2.50)$$

where  $N \equiv N_c$  (in the figure) is the number of cells, with  $q = 2\pi n/(2N)$ , for  $n = 0, 1, 2, \dots, 2N - 1$ , and  $\mathbf{S}_j = \mathbf{A}_{(j+1)/2}$ , if  $j$  is odd, while  $\mathbf{S}_j = \mathbf{B}_{1,j/2} + \mathbf{B}_{2,j/2}$ , if  $j$  is even, and here we are labeling the sites in a more convenient way: A<sub>1</sub>, B<sub>1l</sub>, and B<sub>2l</sub> just denote the sites A<sub>1</sub>, B<sub>1</sub>, and B<sub>2</sub> of the  $l$ th unit cell. In the Lieb-Mattis phase the ferrimagnetic order is indicated by a sharp peak at  $q = \pi$  (a period-2 configuration); while in the decoupled phase, in which a period-4 structure is observed (see also Fig. 2.17), there is a peak at  $q = \pi/2$ . These two situations are magnetic configurations commensurate with the lattice, while the spiral phase is indicated by a peak at a value of  $q$  between  $q = \pi/2$  and  $q = \pi$ . In Fig. 2.19 (a) we display the behavior of  $q$  as a function of  $J$  for finite systems calculated through ED and DMRG (we took advantage of previous results produced in our laboratory). Finite size effects lead to a little shift in the transition point from the spiral phase to the decoupled phase, even though  $q$  can be clearly used to mark the spiral phase.

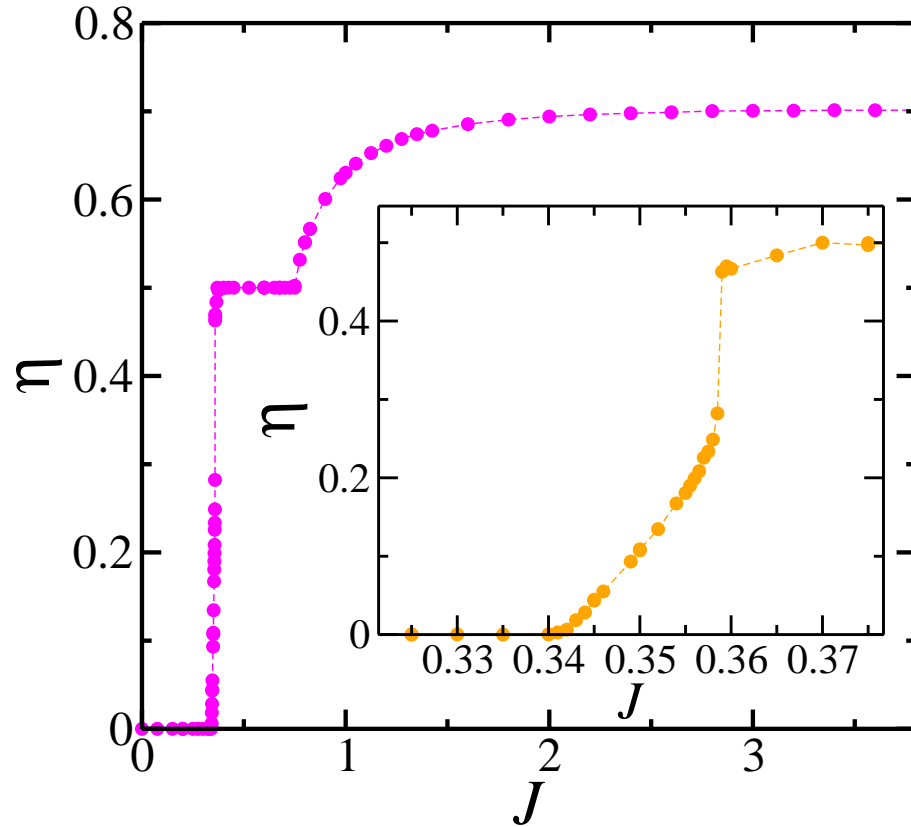


Figure 2.18: Quantum rotors with frustration  $F_2$ : average singlet density per unit cell for the momentum correlations at B sites along the same rung of the ladder. The inset shows details of the phase transition around  $J = 0.36$ .

Motivated by these results, we consider the classical model in the space spanned by two parameters (in the approach of Sec. 2.3, one single parameter sufficed to explain the results): a canting angle  $\theta$  between the B momenta at the same cell and the pitch angle  $q$  associated with the spiral order. The classical vectors are accordingly written as:

$$\begin{aligned}
\mathbf{A}_l &= \cos[q(2l-1)]\mathbf{x} + \sin[q(2l-1)]\mathbf{z}; \\
\mathbf{B}_{1l} &= \cos(\theta)\cos(2ql)\mathbf{x} + \sin(\theta)(-1)^l\mathbf{y} \\
&\quad + \cos(\theta)\sin(2ql)\mathbf{z}, \text{ and} \\
\mathbf{B}_{2l} &= \cos(\theta)\cos(2ql)\mathbf{x} + \sin(\theta)(-1)^{l+1}\mathbf{y} \\
&\quad + \cos(\theta)\sin(2ql)\mathbf{z},
\end{aligned} \tag{2.51}$$

with  $|\mathbf{A}_l| = |\mathbf{B}_{1l}| = |\mathbf{B}_{2l}| \equiv 1$ , while  $\mathbf{x}, \mathbf{y}$  and  $\mathbf{z}$  are orthogonal unit vectors in the three-dimensional space. Substituting these fields in the classical version of the Hamiltonian, Eq. (2.26), we get the energy function  $E(q, \theta) \sim 4\cos q \cos \theta + J(\cos 2\theta + \cos 2q + 2\cos^2\theta \cos 2q - 2\sin^2\theta)$  and minimizing this function with respect to  $q$  and  $\theta$ , we find that  $\cos(\theta) = 1$  and  $\cos(q) = \pi$  for  $0 < J < (1/3)$ , which is the classical version of the Lieb-Mattis phase found for  $0 < J < 0.34$  in the quantum Hamiltonian, for both quantum rotors (FERRI phase) and spin system (Phase F1 of Ref. [59]). For  $(1/3) < J < 1$  we obtain

$$\cos(\theta) = \sqrt{\frac{1-J}{2J}}; \tag{2.52}$$

$$\cos(q) = -\cos(\theta), \tag{2.53}$$

which may be seen as the classical version of the CANTED phase ( $0.34 \lesssim J \lesssim$

0.75) and of the spiral phase ( $0.445 \lesssim J \lesssim 0.91$ ) found in Ref. [59]. This phase holds some similarities with the second phase observed for the quantum rotors in the first single-site approach of Sec. 2.3. Finally, for  $J > 1$  the three chains are antiferromagnetically ordered with the B momenta lying in the  $y$  direction and the A momenta ordered in the  $z$  direction, which is the classical analog of the decoupled phase observed for  $J > 0.75$  for the quantum rotors and for  $J > 0.91$  for the spin system [59]. Such phase does not exist in the single-site approach: it is only obtained asymptotically ( $J \rightarrow \infty$ ). Therefore, the classical solution presents two critical points:  $J_{c1,\text{classical}} = 1/3$  and  $J_{c2,\text{classical}} = 1$ , and the transitions remain second order. Also, the first-order transition at  $J = 0.36$  ( $J_t \approx 0.445$ , for the spin systems) is not observed in the classical model. In fact, in the F<sub>2</sub> phase[59] ( $0.34 \lesssim J \lesssim 0.445$ ) the number of singlets is quantized and the spiral peak is absent, while in the classical model the two orders coexist for  $J_{c1,\text{classical}} < J < J_{c2,\text{classical}}$ . This classical result is also indicated in Fig. 2.19 (a).

In Fig. 2.19 (b), we present the results of this classical interpretation for the momentum correlations. A direct relationship with Fig. 2.15 can be established: we have the classical counterparts of the FERRI phase ( $J \leq 1/3$ ) and the AF phase ( $J \geq 1$ ); the CANTED phase is but a gradual continuous transition between the FERRI and AF phases. Further, the decoupling transition in the classical model is clearly observed at  $J = 1$  through the dot products indicated in the figure. Finally, we notice that when this classical approach is applied to frustration F<sub>1</sub>, the minimum energy configuration obtained is the same as that derived through the first classical model discussed in Sec. 2.3.

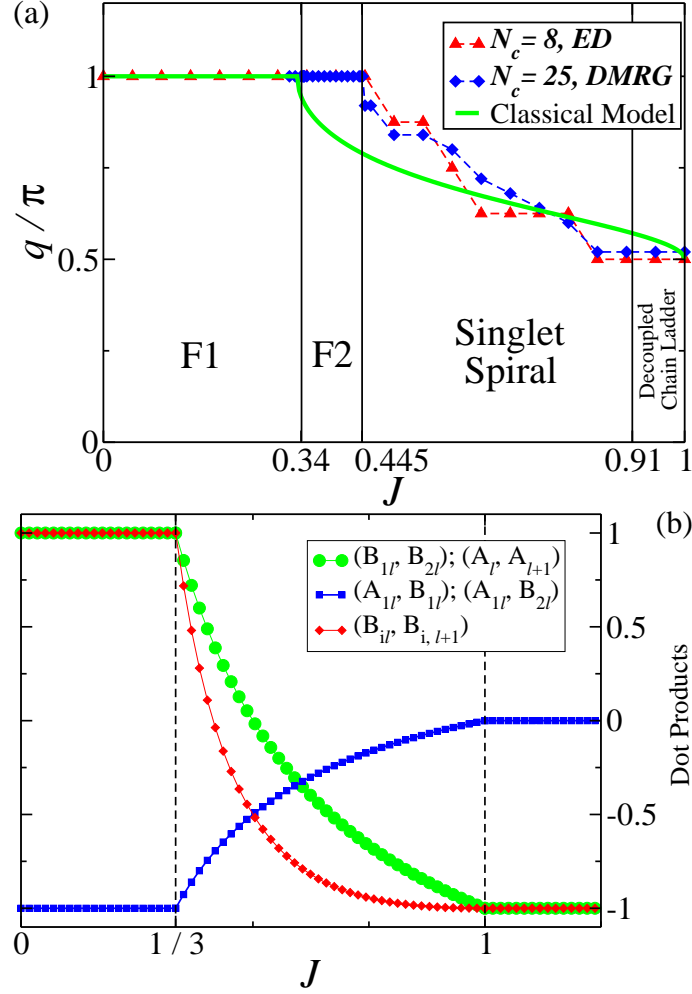


Figure 2.19: (a) Pitch angle for the quantum spin-1/2 model calculated through ED, DMRG, and for the minimum energy configuration of the classical vector model with two order parameters:  $q$  (pitch angle) and  $\theta$  (canting angle). The transition points estimated in Ref. [59] are indicated. (b) Momentum dot products ( $i = 1, 2$ , and  $l$  denotes the unit cell) in the minimum energy configuration of the classical vector model.

## 2.5 Summary and conclusions

In dealing with quantum rotors placed at the sites of an  $AB_2$  chain we resorted to a cluster variational MF theory implemented via two distinct approaches, which yielded different results. First, we learned that the size of the Hilbert space could be considerably reduced without affecting results, with the proviso that the rotor states should be kept possibly nearest ( $\ell = 1/2$ )-momentum states. Our main goal was then to attempt to freeze the QR momentum tower at the least value of  $\ell$  and so be able to trace a parallel between rotor and spin-1/2 systems. That was attained by increasing the importance of the kinetic energy term in the Hamiltonian (by setting relatively high values of the coupling  $g$ ), and a judicious choice of the Hilbert space, whenever needed. This was a most important fact for the computations in multiple-cell clusters that were to be performed in the second approach, where processing capacity is a crucial limiting factor.

In the first approach the natural single-site MF theory was developed. A two-phase pattern was produced with the phase transition between them being of second order for  $M = 0$  and of first order for  $M = 1$ . For  $J \leq 1$ , the Lieb-Mattislike phase typical in the spin-1/2 system arose, and for  $J \gg 1$ , we observed the decoupling of the system, where the momenta on the A sites tend to become uncorrelated with the momenta on the B sites, which in turn formed singletlike pairs, while the decoupling of the A sites was a salient feature laid bare by this approach, much like the dimer-monomer phase in Ref. [59]. A classical interpretation was laid down that conformed to our QR numerical findings, inclusively showing how the fixed coupling of momentum and position turns the second-order transition into a first-order one within certain scenarios: in this case when  $M = 1$ . With the benefit of hindsight it was obvious that the results would be classical: in this methodology

we dealt but with averages of quantum observables. Therefore, we were not able to provide a reasonable quantum picture that could relate to the known behavior of the corresponding quantum  $AB_2$  chain. Furthermore, treated this way the system was not able to essentially tell apart frustration  $F_1$  from frustration  $F_2$  and this alone constituted a major setback. So, all this was a reminder that the main goal of our work still remained to be achieved.

In our last step, we then improved the former approach by producing a cluster (double-cell) variational MF theory in which the trial Hamiltonian acts on the space composed of the tensor product of the respective local subspaces of the six sites at two neighboring unit cells. The gist of this theory stands on the important fact that it allows the construction of the two-point correlations  $\langle \hat{\mathbf{X}}_i \cdot \hat{\mathbf{Y}}_j \rangle$  between any pairs of operators acting on sites  $i, j$  of the cluster. This afforded us the observation of quantum features inherent in the system, as well as to distinguish between both frustrations  $F_1$  and  $F_2$ . For the construction of this more complex “system”, we relied on the availability of processing capacity to carry out the numerical implementation. The experience acquired in the first approach through our endeavor to optimize computations just carried over.

For frustration  $F_1$ , besides the QR numerical simulation, we performed ED on the spin-1/2 diamond chain using a system with 28 sites and calculated the correlation functions between spin at a central cluster, as well as other relevant physical quantities. Upon confronting with the QR results, we verified that the QR phase diagrams obtained through numerical implementation of the double-cell MF variational approach exhibited a sequence of phases analogous to those of the spin chains, with phase transitions of the same nature. We therefore produced the FERRI-TD-DM phase sequence, with first order transitions, which is in essence

the phase diagram of Ref. [57]. The transition point FERRI-TD at  $J = 0.68$  is somewhat displaced, but the transition point TD-DM at  $J = 2$  was exactly calculated by our approach.

For frustration  $F_2$ , we obtained a phase diagram in good agreement with the results of Ref. [59] on the respective spin-1/2 chains, endowed with the equivalent frustration pattern: FERRI, CANTED, and AF which are associated with the phases F1, F2/Spiral Singlet, and decoupled ladder chain, respectively, of the spin model. Notwithstanding, the criticality of the A spins correlations manifests itself here as an AF magnetic ordering due to finite-size effects. For the same reason, we were not able to probe the short-rangedness of the correlation functions between the B momenta. We also produced ED as well as DMRG results that helped us to visualize the spiral phase in the spin system, and derived an insightful classical interpretation.



## Chapter 3

# Ground state and thermodynamics of alternating quantum spin chains

### 3.1 Introduction

In what follows, we present a brief review of the latest developments in molecular magnetism. Although not at all biased, it is quite a partial account considering on one hand the overwhelming extensiveness of the available literature on the subject matter and, on the other hand, the limited time to carry out a thorough research. Nevertheless, we drew on the most important facts and kept as close as possible to our objectives in the present chapter.

The field of molecular magnetism has become nowadays a hot topic of research at the frontier between chemistry and physics. Chemists bustle at research centers the world over in their quest to synthesize new compounds and predict their properties on the basis of a molecular approach to the exchange phenomenon, while physicists in turn test on one-dimensional (1D) materials the validity of phenomenological

models. As one example of the early successes of these joint efforts we cite the experimental proof of the Haldane conjecture [50] in a molecular chain compound [85]. So far, the organic chemistry synthesis endeavor in this field has afforded a great deal of original compounds with properties that are characteristic of both magnets and organic compounds. Notwithstanding, to date and to the best of our knowledge, molecular magnetism has not yet provided materials that can measure up to metallic hard magnets at the high-temperature regime and thus be suitable for use in everyday objects. Due to the fact that 1D magnetic systems are unable to display long-range order at finite temperatures [86], one of the main lines of research in molecular magnetism of the last three decades has therefore been driven by the vehement quest to efficiently connect magnetic 1D chains in three-dimensional (3D) networks in order to enhance bulk magnetism and make it observable and eventually a viable industrial product. On the other hand, low-dimensional magnetic materials besides continuing to represent a source of intermediate building blocks to be used in the synthesis of such yearned-for bulk molecular-based materials are also very interesting objects on their own.

So we will focus our review mostly on 1D or quasi-1D materials. At first, investigated compounds were regular homometallic chains in which the magnetic centers are equally spaced along the chain [87–89]. In the meantime, work was also being done on purely organic compounds (that is, which consist only of the light elements H, C, N, and O) and one of the first bulk ferromagnets of this kind was discovered, to wit *p*-nitrophenyl nitronyl nitroxide, abbreviated as *p*-NPNN [90]. Only ten years later the first example of a genuine organic ferrimagnetic material having well defined chemical and crystal structure was synthesized, viz the PNNBNO compound [68]. Since the possibilities of synthesis in molecular chemistry are virtually limitless,

the appearance of other interesting structures was naturally foreseeable. We speak here of polymetallic chains, that is, those endowed with various metallic centers, different spatial intra- and interchain architectures, alternating interaction pathways (superexchange), leading to different magnetic properties especially at low temperature where interchain interactions begin to play a more significant role [91, 92]. Most important among these are the structurally ordered bimetallic chains of the type  $(A-X-B-X)_n$ , where A and B are two different paramagnetic metal ions and X is a bridging ligand. The first example of a bimetallic ferrimagnetic chain compound [93, 94] was built of  $Mn^{2+}$  and  $Cu^{2+}$  ions endowed with spin 5/2 and spin 1/2, respectively, linked through a dithioxalato ligand. Bimetallic chains possess intrachain interactions that are mostly of antiferromagnetic nature [93–101], with a number of ferromagnetic chains also known [102–105]. This line of research is still very active with the focus on cyano- and oxamato-bridged compounds being very intense, mainly because of the discovery of slow relaxation of the magnetization at low temperature in many of them; the cyano groups offer other possible interesting features on the side, to wit redox activity, photosensitivity, or chirality [106].

The materials referred to so far are considered from the magnetic standpoint either to be organic, that is, the spin carriers are organic entities, or inorganic (homometallic chains), where the magnetic centers reside on metal complexes. An intermediate synthesis approach resulted in the family of compounds of paramount importance constituted by the metallo-organic (hybrid) chains, in which the spin carriers are a metallic ion and an organic free radical, generally nitroxide. Specimens of this novel family have also been synthesized and contributed to enrich further the large variety of magnetic materials [92, 107–113]. The success of the metallo-organic route chosen by several groups owes to the use of nitronyl nitroxide

free radicals (NITR) where R stands for an alkyl (methyl, ethyl) or aromatic group (phenyl). This organic entity has one unpaired electron carrying a spin  $1/2$ , delocalized over the 5 atoms of its O-N-C-N-O fragment as shown by polarized neutron studies on a compound of very weakly interacting nitronyl nitroxide molecules [114], and the electronic configuration allows the radical to be coupled simultaneously to two metallic groups. Such groups can be built of one magnetic 3d metallic ion such as Cu, Ni, Mn or Co, surrounded by magnetic inactive bulky organic moieties like hexafluoroacetylacetonates (hfac) [107–110, 113, 115]. The use of the NITR free radical leads preferentially to an antiferromagnetic intrachain coupling which proves to be stronger as against the interaction in the bimetallic counterparts, except for the case of some Cu complexes where ferromagnetic interactions are manifest. The possible cis or trans  $\text{NITR-M(hfac)}_2$  (M stands for a metallic ion) coordination scheme, determined by the R group, can yield different architectural arrangements leading to linear, zig-zag or helical chains endowed with different magnetic properties. Worth mentioning are the studies by the pioneering research group around Caneschi [109] within the rich and very important family of the Mn-NITR compounds, where the underlying interaction is the strong antiferromagnetic coupling of the spin- $1/2$  radicals and the spin- $5/2$  manganese(II) ions. Several other compounds with different R groups, investigated by magnetometry and electron paramagnetic resonance (EPR), were shown to present a ferrimagnetic 1D behavior.

The temperature dependence of the product of the molar magnetic susceptibility ( $\chi_m$ ) and the temperature ( $T$ ), in the mid- and high-temperature regime, for ferrimagnetic polymers, when the intrachain interaction is antiferromagnetic, exhibits a characteristic minimum, which may be considered as the signature of the 1D ferrimagnetic behavior. On the other hand, the magnetic properties in the very

low-temperature range are influenced by interchain interactions, which can never be totally ignored. In most cases, these interchain interactions lead to the onset of a three-dimensional (3D) antiferromagnetic ordering with a sharp maximum of  $\chi_m T$  (and  $\chi_m$ ), as shown in Fig. 3.1. Let us consider now the case of the Mn-NITR compounds. It is known that in these materials the chains are well magnetically isolated from each other thanks to their large separation by bulky magnetically inactive organic moieties. This ensures very weak interchain exchange interactions, resulting in a ratio of intra- to interchain interaction that reaches several orders of magnitude, so that the virtual isolation of the chains prompts a quite accentuated 1D behavior. But at low temperature, between 5K and 9K, these materials are reported to exhibit bulk magnetic order, and this is imputed to a phase transition toward a 3D long-range order consisting of a ferromagnetic ordering of the magnetic centers, because in pure 1D compounds, long-range order is not expected at finite temperature [86]. Altogether, it is necessary to take into account other usually neglected interactions such as dipolar to justify such phase transition. Indeed, very weak interchain dipolar interactions, reinforced by strong intrachain correlations, can induce such a 3D long-range order [116–118]. The role of the dipolar interaction has also been invoked to explain the 3D magnetic ordering of high spin molecular cluster compounds [119–121]. More generally, the transition to the 3D long-range order of 1D compounds is a very complex phenomenon and not totally understood nowadays.

Now we digress briefly to touch upon an important development in the field of molecular magnetism. More recently polynuclear clusters (complex molecules) [122] and 1D chains [106] are being widely investigated for their ability to retain a magnetic memory of purely molecular origin as well as for an assortment of interest-

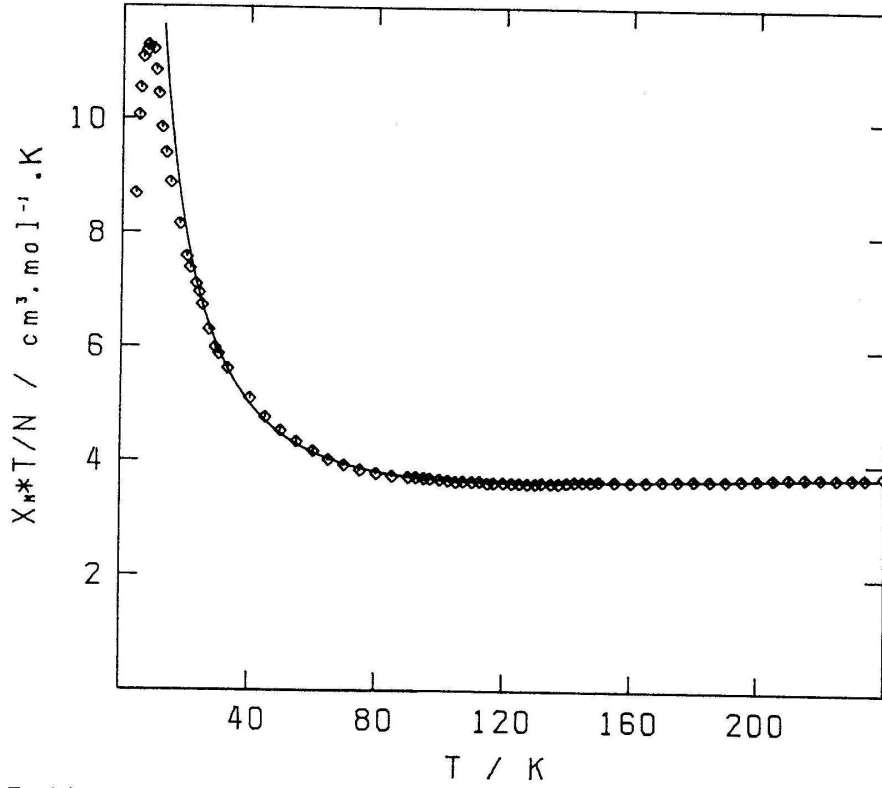


Figure 3.1: Temperature dependence of  $\chi_m T$  for the first bimetallic chain (CuMnDTO) [93, 94], where  $\chi_m$  is the molar susceptibility and  $T$  is the temperature. Squares represent experimental points, and the full line is a plot of Eq. (3.35). A minimum occurs at  $T = 130\text{K}$ . Reproduced from Seiden[141].

ing quantum effects. These two classes of materials have been given the evocative acronyms single-molecule magnets (SMM) and single-chain magnets (SCM), respectively. The observation of slow magnetic relaxation in SMMs is now considered a paramount achievement of molecular magnetism of the last few years. Such systems have provided unique opportunities for the study of molecular magnetic hysteresis [123], quantum tunneling of the magnetization [124], magnetic avalanches, that is to say, abrupt magnetic reversals [125], and phase interference (Berry phase) [126], which are features where slow magnetic relaxation plays an important part. As already stated above, purely 1D systems do not exhibit any long-range ordering at finite temperatures and so they cannot be stabilized as *thermodynamic magnets* in consequence, for instance, of a ferromagnetic order. Nevertheless, as for SCMs the possibility to observe the freezing of the magnetization, in a process of very slow relaxation, was predicted in the 1960s by Glauber [127], who developed the kinetic model for a chain of ferromagnetically coupled spins showing Ising-type anisotropy. Gatteschi and co-workers were the first to report observation of a slow magnetization in a cobalt(II)-nitronyl-nitroxide alternating chain where the effective Ising-type spin  $S_{eff} = 1/2$  of Co(II) and the isotropic  $S = 1/2$  of the radical are antiferromagnetically coupled [128]. This is another example of an experimental confirmation of a brilliant theoretical prediction formulated more than four decades ago. Since then, SCM behavior in several compounds has been observed [106, 129, 130], and a new field of research opened up. Most recently it was discovered that one-dimensional cobalt-radical coordination magnets have revealed an astounding facet: when 1D units undergo a phase transition to 3D magnetic order, a very large coercivity arises and increases so pronouncedly at low temperature as to make these materials comparable to the hardest magnets ever known [131, 132]. On the other hand, new

perspectives for storing information in a single magnetic polymer are wide open. Also interesting physical properties other than magnetic are a proven possibility. All in all, the physics and chemistry of these systems have become more and more very active fields of research with a long, winding, but all the more exciting and rewarding road to tread.

## 3.2 Theoretical models and methods

Almost all the systems referred to in the previous section can be well described, insofar as they are considered 1D systems, by the quantum isotropic Heisenberg Hamiltonian

$$\hat{H}_{ex} = \sum_{i,j} J_{ij} \hat{\mathbf{S}}_i \cdot \hat{\mathbf{S}}_j, \quad (3.1)$$

where  $\hat{\mathbf{S}}_i, \hat{\mathbf{S}}_j$  are spin operators at sites  $i$  and  $j$  ( $i \neq j$ ) and  $J_{ij}$  are the exchange interactions between the respective spins and may be negative (ferromagnetic) or positive (antiferromagnetic). Further studying the magnetic susceptibility, the Zeeman term must be considered

$$\hat{H}_{zee} = -\mu_B H_z \sum_i g_i \hat{S}_i^z, \quad (3.2)$$

where the  $g_i$  are the Landé factors associated with the  $S_i^z$ , the  $z$  projection of the spin at site  $i$ . As opposed to the uniform linear chain, an alternating (binuclear, i.e., the unit cell contains two spin carriers) chain, with only nearest-neighbor interactions, is such a system where at least one of the following relations occur: i)  $\hat{\mathbf{S}}_{2k-1} \neq \hat{\mathbf{S}}_{2k}$ , ii)  $J_{2k-1,2k} \neq J_{2k,2k+1}$ , or iii)  $g_{2k-1} \neq g_{2k}$ . Many a system reviewed in the previous section, while thermodynamically behaving at the 1D regime, above a certain usually low temperature threshold, can be well described by such alter-



nating spin chains. Among these materials, spin-1/2 spin-5/2 chains with isotropic intrachain interaction and  $g$  factor have been the focus of intense research in the past three decades. Materials of the sort, exhibiting both ferromagnetic systems [91] as well as antiferromagnetic [93–95, 97, 99, 102, 109] have been characterized. Also chains with other alternating spin values [98, 103–105, 108], and systems with both alternating spins and interactions have been reported [97, 100], as well as systems with both alternating spins and  $g$  factors [97]. The first example of an alternate ferromagnetic-antiferromagnetic spin-1/2 chain was announced by the Caneschi team [107]. Furthermore, for a large number of other systems known in the literature, the experimental evidence indicates that single-ion anisotropy is relevant and so a finite magnetic anisotropy must be included in the model,

$$\hat{H}_{an} = D \sum_{i,j} \hat{S}_i^z \hat{S}_j^z, \quad (3.3)$$

where  $D$  is a coupling constant that gives the strength of the single-ion anisotropy. So far, compounds modeled by this anisotropic Halmiltonian have been widely researched and are particularly indicated as possible candidates to choose from in the synthesis of SCMs [106]. Finally, we simply have a large class of compounds that can be satisfactorily modeled by a fully isotropic Hamiltonian in which the three conditions i, ii and iii above are just equalities [89, 90]. To proceed with our discussions, we will write Eq. (3.1) in such a way as to become easy to specialize in a quantum linear chain made up of two sublattices, with a uniform exchange interaction, which may be either positive (antiferromagnetic) or negative (ferromagnetic):

$$\hat{H}_{sS} = \sum_i^{N-1} \hat{H}_i, \quad \hat{H}_i = J(\hat{\mathbf{S}}_i + \hat{\mathbf{S}}_{i+1}) \cdot \hat{\mathbf{s}}_i, \quad (3.4)$$

for a chain with  $N$   $[s, S]$  cells.

When  $s = S$  we fall back to the totally isotropic and uniform Heisenberg spin chain. So far, this model, as it is, for  $N \rightarrow \infty$ , has been analytically intractable. A closed-form solution has been provided only in the classical limit, when  $S \rightarrow \infty$  [133]. So, when the spins are large enough, this method may be applied as was the case of a spin-5/2 chain, with some modifications [89]. A limiting behavior may be established from numerical results worked out on finite closed forms (rings) extrapolated in order to yield the thermodynamic limit ( $N \rightarrow \infty$ ). This approximate approach was first used by Bonner and Fisher [134], for the  $S = 1/2$  chain and later on extended to chains with arbitrary quantum spin numbers [135]. The only limitation of this model is the storage and processing capacity of the available computers. Therefore, other recourses have been sought in the quest to estimate the behavior in the infinite chain limit. Among early efforts in this field of endeavor, we cite spin-wave theory [136, 137], high-temperature series expansions [138], and Green's functions approaches [139].

With respect to alternating chains, i.e., chains made up of unequal sublattices ( $s \neq S$ ), the first attempt at finding a closed form for the susceptibility  $\chi$  was carried out by Blöte [140], who set one of the spin quantum numbers infinite (i.e., it could be treated classically). However, in his calculations he neglected the contribution of the quantum sublattice vis-à-vis the classical one, thus rendering his procedure unable to take into account the experimental results. In 1981, Verdaguer and Gleizes discovered the first bimetallic chain [93, 94], and this stimulated extensive theoretical research in the area. The compound  $\text{CuMn}(\text{S}_2\text{C}_2\text{O}_2)_2 \cdot 7.5\text{H}_2\text{O}$  (CuMnDTO) was made up of two different paramagnetic ions,  $\text{Cu}^{2+}$  and  $\text{Mn}^{2+}$ , structurally ordered in an alternating manner and bridged by a polyatomic dithioxalato anion ligand

- showing the pattern of a regular -Cu-Mn-Cu-Mn- alternating spin-1/2 spin-5/2 chain. Motivated by the failure of previous models to explain the properties of the new compound, Seiden [141] set about solving analytically the magnetic susceptibility of the  $[1/2, S]$  chain, where  $S$  is large enough to be considered classical. So far, this simple model has been a valuable tool in the research of new materials [97, 108, 109, 112, 115, 122], besides constituting another interesting example of the interplay between the experimental and theoretical assembly lines.

In the context of pure quantum methods, alternating-spin Heisenberg chains were initially approached by numerical diagonalization [142]. Further investigations were carried through with the use of the powerful techniques of density-matrix renormalization group [143, 144] and quantum Monte Carlo methods [145, 146] in an attempt to clear up dual features of ferrimagnetic excitations. The conventional antiferromagnetic spin-wave formalism [136, 137] has been modified, on the one hand by following the Takahashi prescription [147], which was originally proposed for ferromagnets, and then for 2D antiferromagnets [148], while on the other hand with the introduction of a slightly different approach [149]. The finite-temperature Lanczos method (FTLM) [150] - which is based on the Lanczos diagonalization technique and random sampling - has also become a very useful tool in the evaluation of both static and dynamical quantities in small many-body quantum systems. We will take advantage of such method in this chapter in a similar manner we did ED previously.

### 3.3 Static properties of an alternating isotropic chain of quantum spins 1/2 and classical spins

We now provide an overview of the article by Seiden [141], which as stated before, has been taken advantage of in the determination of the coupling constant  $J$ , as an indicator of the dimensionality as well as the overall behavior of the investigated materials (for which one sublattice spin can be treated as a classical vector) in the mid- and high-temperature ranges. We proceed then with the main purpose of retrieving the analytical expression of the magnetic susceptibility, which will later be recalled in this chapter, but also with a didactical mind so that, when deemed necessary, we try to clarify a couple of passages here and there in the paper.

The Hamiltonian was already given in Eq. (3.4), and in Fig. 3.2 (a) we provide a depiction of the alternating chain (sS chain) in question, illustrating the ground state, which according to the Lieb-Mattis theorem [83] possesses a net spin 2 per unit cell. In what follows, the spins  $\hat{\mathbf{s}}_i$  will be treated as quantum operators, with  $s = 1/2$ , whereas the spins  $\hat{\mathbf{S}}_i$  will be considered vectors of length  $S$ . As a result, each  $\hat{\mathbf{s}}_i$  is coupled only with its two classical next neighbors  $\mathbf{S}_i$  and  $\mathbf{S}_{i+1}$ , so that all the  $\hat{H}_i$  commute. This is the great advantage of interspersing classical vectors throughout the chain, in between the quantum spins, allowing for a simple expression of the partition function below, from which quantities of interest can be analytically derived.

### 3.3.1 Free energy

One sets about calculating the free energy. The partition function is given by

$$Z = \left( \frac{2S+1}{4\pi} \right)^N \int d\Omega_1 \dots d\Omega_N z_{1,2} z_{2,3} \dots z_{N-1,N}, \quad (3.5)$$

with

$$z_{i,i+1} = \exp\left(\frac{-\beta J S_{i,i+1}}{2}\right) + \exp\left(\frac{\beta J S_{i,i+1}}{2}\right), \quad (3.6)$$

and

$$\mathbf{S}_{i,i+1} = \mathbf{S}_i + \mathbf{S}_{i+1}, \quad S_{i,i+1} = |\mathbf{S}_{i,i+1}| = S \sqrt{2(1 + \cos \theta_{i,i+1})}, \quad (3.7)$$

where  $\theta_{i,i+1}$  is the angle formed by  $\mathbf{S}_i$  and  $\mathbf{S}_{i+1}$ , and we consider the z direction as that of  $\mathbf{S}_i + \mathbf{S}_{i+1}$ . There are N classical spins (which amounts to say N cells) and N-1 quantum spins: open boundary conditions, where each quantum spin is surrounded by two classical vectors. In Eq. (3.6), one summed over the quantum degrees of freedom ( $s^z = -1/2, +1/2$ ) projected on the  $z_i$  direction. In Eq. (3.5), the integration over the classical degrees of freedom was already performed in  $dS$ , where the coordinate  $S$  was assumed to take on  $2S+1$  discrete values (semi-quantum approach), while remaining N angular integrations to be carried out ( $d\Omega_i = \sin \theta_i d\theta_i d\phi_i$ ).  $4\pi$  is just a normalization constant related to the solid angle of the entire sphere.

The next step consists in developing Eq. (3.6) in a series of Legendre polynomials:

$$z_{i,i+1} = z(\theta_{i,i+1}) = \sum_{l=0}^{\infty} a_l P_l(\cos \theta_{i,i+1}). \quad (3.8)$$

The above polynomials, involving an angle between two vectors ( $\theta_{i,i+1}$ ), can be farther developed in terms of the individual angles ( $\theta_i$  and  $\theta_{i+1}$ ) by using the addition

theorem for spherical harmonics

$$P_l(\cos \theta_{i,i+1}) = \frac{4\pi}{(2l+1)} \sum_{m=-l}^{m=l} Y_{l,m}^*(\theta_i, \phi_i) Y_{l,m}(\theta_{i+1}, \phi_{i+1}). \quad (3.9)$$

Upon using the normalization and orthogonality conditions

$$\int_0^{2\pi} d\phi \int_0^\pi Y_{l',m'}^*(\theta, \phi) Y_{l,m}(\theta, \phi) = \delta_{l,l'} \delta_{m,m'}, \quad (3.10)$$

the partition function for a finite chain (with N classical vectors) can be evaluated, namely:

$$Z = (2S+1)^N \sum_{l=0}^{\infty} \frac{a_l^{N-1}}{(2l+1)^{N-1}}. \quad (3.11)$$

and for an open and infinite chain ( $N \rightarrow \infty$ ), one gets finally the mathematically rigorous result

$$Z = (2S+1)^N a_0^{N-1}, \quad (3.12)$$

from which the desired expression for the free energy can be derived, which then reads

$$F = -\frac{1}{\beta} \log Z, \quad (3.13)$$

where the term  $a_0$  must yet be calculated. This will be done in a short while.

### 3.3.2 Two-spin correlations

There are three types of correlations to be calculated, defined below so as to cohere with the rotational invariance of the Hamiltonian in Eq. (3.4), namely

- all-classical correlations

$$\begin{aligned} \langle S_i^z S_{i+p}^z \rangle &= \left( \frac{2S+1}{4\pi} \right)^N \frac{1}{Z} \int d\Omega_1 \dots d\Omega_N z_{1,2} \dots z_{i-1,i} S \cos \theta_i z_{i,i+1} \times \\ &\dots \times z_{i+p-1,i+p} S \cos \theta_{i+p} z_{i+p,i+p+1} \dots z_{N-1,N}; \end{aligned} \quad (3.14)$$

- quantum-classical correlations

$$\begin{aligned} \langle s_i^z S_{i+p}^z \rangle &= \left( \frac{2S+1}{4\pi} \right)^N \frac{1}{Z} \int d\Omega_1 \dots d\Omega_N z_{1,2} \dots z_{i-1,i} y_{i,i+1} z_{i+1,i+2} \times \\ &\dots \times z_{i+p-1,i+p} S \cos \theta_{i+p} z_{i+p,i+p+1} \dots z_{N-1,N}, \end{aligned} \quad (3.15)$$

where the spin operator is averaged by the temperature:

$$y_{i,i+1} = \text{trace} [s_i^z \exp(-\beta J \mathbf{S}_{i,i+1} \cdot \hat{\mathbf{s}}_i)]; \quad (3.16)$$

- all-quantum correlations

$$\begin{aligned} \langle s_i^z s_{i+p}^z \rangle &= \left( \frac{2S+1}{4\pi} \right)^N \frac{1}{Z} \int d\Omega_1 \dots d\Omega_N z_{1,2} \dots z_{i-1,i} y_{i,i+1} z_{i+1,i+2} \times \\ &\dots \times z_{i+p-1,i+p} y_{i+p,i+p+1} z_{i+p+1,i+p+2} \dots z_{N-1,N}. \end{aligned} \quad (3.17)$$

### 3.3.3 Evaluation of the classical correlations

To this end, one needs to calculate the first two terms of Eq. (3.8), as it is easy to infer from examining Eq. (3.14). For a general term  $a_n$ , we have (from the normalization and orthogonality of Legendre polynomials):

$$a_n = \frac{(2n+1)}{2} \int_0^\pi z(\theta) P_n(\cos \theta) \sin \theta d\theta, \quad (3.18)$$

from which derive

$$a_0 = \frac{1}{2} \int_0^\pi z(\theta) \sin \theta d\theta \quad \text{and} \quad a_1 = \frac{3}{2} \int_0^\pi z(\theta) \cos \theta \sin \theta d\theta. \quad (3.19)$$

Noting that  $\cos \theta/2 = [(1 + \cos \theta)/2]^{1/2}$ , with the appropriate change of variables ( $\beta JS \cos \theta/2 = u$ ), and by using the formulas from elementary calculus

$$\begin{aligned} \int u \cosh(u) du &= u \sinh(u) - \cosh(u), \\ \int u^3 \cosh(u) du &= (u^3 + 6u) \sinh(u) - (3u^2 + 6) \cosh(u), \end{aligned} \quad (3.20)$$

one finds finally:

$$\begin{aligned} a_0 &= 4(x^{-1} \sinh(x) - x^{-2} \cosh(x) + x^{-2}), \\ a_1 &= 12[(x^{-1} + 12x^{-3}) \sinh(x) - (5x^{-2} + 12x^{-4}) \cosh(x) - x^{-2} + 12x^{-4}], \end{aligned} \quad (3.21)$$

where  $x = \beta JS = JS/k_B T$ . Now, with the value of  $a_0$  at hand, the free energy can then be calculated as a by-product.

To calculate the classical correlations as prescribed by Eq. (3.14), we note that the integrals over  $d\Omega_1 \dots d\Omega_{i-1}$  as well as those over  $d\Omega_{i+p+1} \dots d\Omega_N$  can be factored off (they contribute a factor of  $4\pi(4\pi a_0)^{N-p-1}$  which cancel out with an equal contribution coming from  $1/Z$  outside of the integral). To accomplish our task we have to calculate now the *correlated* integrals ( $d\Omega_{i+1} \dots d\Omega_{i+p}$ , whereto we resort to a technique used by Fisher [133]: The angles  $\theta_i$  and  $\theta_{i+p}$  are polar angles referred to the  $z$  axis. By using  $\mathbf{S}_{i+p-1}$  as polar axis, with  $\mathbf{S}_i$  defining the reference



plane for  $\phi_{i+p}$ , we have

$$\cos \theta_{i+p} = \cos \Theta_{i+p} \cos \theta_{i+p-1} + \sin \Theta_{i+p} \sin \theta_{i+p-1} \cos(\Phi_{i+p} - \phi_{i+p-1}), \quad (3.22)$$

where  $\Theta_{i+p}$  is the angle between  $\mathbf{S}_{i+p}$  and  $\mathbf{S}_{i+p-1}$ . Upon integration only the first term in Eq. (3.22) survives due to  $\langle \cos \Phi_{i+p} \rangle \equiv 0$ , and so we get

$$\langle \cos \theta_{i+p} \rangle = \langle \cos \Theta_{i+p} \rangle \langle \cos \theta_{i+p-1} \rangle = \langle \cos \theta_{i+p-1} \rangle \langle \cos \theta \rangle, \quad (3.23)$$

where  $\Theta_{i+p}$  is turned into the integration variable  $\theta$ . By repeating the procedure for  $\cos \theta_{i+p-1}$ , we can then infer a simple recurrence relation. Thus, by means of Eq. (3.23), we perform the last part of the integration, yielding a factor of  $(4\pi)^p (a_1/3)^p S^2$ , which divided by the rest factor  $(4\pi a_0)^p$  coming from  $1/Z$  (outside the integral) gives finally  $(a_1/3a_0)^p S^2$ . The pair correlation function is defined here so that  $\langle S_i^z S_{i+p}^z \rangle = \frac{1}{3} \langle \mathbf{S}_i \cdot \mathbf{S}_{i+p} \rangle$  (rotational invariance), whereby a factor of  $1/3$  must be brought into the final result:

$$\langle S_i^z S_{i+p}^z \rangle = \delta^p \frac{S^2}{3}, \quad (3.24)$$

with

$$\delta = \frac{a_1}{3a_0}. \quad (3.25)$$

### 3.3.4 Evaluation of correlations comprising quantum spins

One uses the basis spanned by the eigenstates of  $s^z$  ( $s^z|m\rangle = m|m\rangle$ ) to evaluate the expression of Eq. (3.16), resulting in

$$y = \sum_m \sum_\mu \langle m|\mu\rangle \langle \mu| \exp(-\beta J \mathbf{S} \cdot \hat{\mathbf{s}}) |\mu\rangle \langle \mu|m\rangle, \quad (3.26)$$

where  $|\mu\rangle$  are the eigenstates of the projection of  $\hat{\mathbf{s}}$  on  $\mathbf{S}$ , and  $\langle m|\mu\rangle$  are the matrix elements of the Wigner- $D^{1/2}(\psi)$  matrix:

$$D^{1/2}(\psi) = \begin{pmatrix} \cos \psi/2 & -\sin \psi/2 \\ \sin \psi/2 & \cos \psi/2 \end{pmatrix}$$

and  $\psi$  is naturally the angle with the  $z$  axis. One gets straightforwardly ( $s = 1/2$ )

$$y = -\cos \psi \sinh\left(\frac{\beta JS}{2}\right); \quad (3.27)$$

$$\cos \psi_{i,i+1} = \frac{S_{i,i+1}^z}{S_{i,i+1}} = \frac{(\cos \theta_i + \cos \theta_{i+1})}{S_{i,i+1}}. \quad (3.28)$$

By expanding the following in a series of Legendre polynomials

$$\frac{\sinh\left(\frac{\beta JS_{i,i+1}}{2}\right)}{S_{i,i+1}} = \sum_{l=0}^{\infty} b_l P_l(\cos \theta_{i,i+1}), \quad (3.29)$$

and with the aid of the calculus formula, with the same change of variables used previously

$$\int u^2 \sinh(u) du = (u^2 + 2) \cosh(u) - 2u \sinh(u), \quad (3.30)$$

one obtains

$$\begin{aligned} b_0 &= x^{-1}[\cosh(x) - 1], \\ b_1 &= 3[(x^{-1} + 4x^{-3}) \cosh(x) - 4x^{-2} \sinh(x) + x^{-1} - 4x^{-3}]. \end{aligned} \quad (3.31)$$

Proceeding analogously to the determination of the all-classical correlations carried out in the previous subsection and introducing

$$\Lambda = 2 \left( \frac{b_1}{3a_0} + \frac{b_0}{a_0} \right), \quad (3.32)$$

one gets finally

$$\begin{aligned} \langle s_i^z S_{i+p}^z \rangle &= -\Lambda \delta^{p-1} \frac{sS}{3}, \\ \langle s_i^z s_{i+p}^z \rangle &= \Lambda^2 \delta^{p-1} \frac{s^2}{3}, \end{aligned} \quad (3.33)$$

where  $p > 0$ . For completeness, the self-correlations are included:  $\langle s_i^z s_i^z \rangle = s(s+1)/3$  and  $\langle S_i^z S_i^z \rangle = S(S+1)/3$ ; the latter defined in such a manner as to build a consistent theory.

### 3.3.5 Magnetic susceptibility

The susceptibility in zero field can now be calculated from the fluctuation relation

$$\chi = \beta \mu_B^2 \sum_{i,j} \langle (g_S S_i^z + g_s s_i^z) (g_S S_j^z + g_s s_j^z) \rangle, \quad (3.34)$$

where  $g_S$  and  $g_s$  are the  $g$  factors of the classical and quantum spins, respectively. By using the correlations just calculated and noting that  $\delta < 1$ , so that  $\sum_p^\infty \delta^p =$

$\delta/(1 - \delta) \sum_p^\infty \delta^{p-1} = 1/\delta \sum_p^\infty \delta^p = 1/(1 - \delta)$ , one gets the closed form for the magnetic susceptibility

$$\chi = \frac{N\beta\mu_B^2}{3} \left[ g_S^2 S^2 \left( \frac{S+1}{S} + 2\frac{\delta}{1-\delta} \right) - 4g_S g_s \Lambda s S \frac{1}{1-\delta} + g_s^2 \left( s(s+1) + 2\Lambda^2 s^2 \frac{1}{1-\delta} \right) \right], \quad (3.35)$$

for a chain with  $N \gg 1$  cells. When  $J > 0$ , the quantity  $T\chi(T)$  has a minimum at a temperature  $T_m$  which is generally situated in a region where  $\beta JS < 1$ , a feature which has been known to be typical of 1D ferrimagnets. At low temperatures, i.e.,  $x \gg 1$ , or  $\frac{J|S|}{k_B T} \gg 1$ , it is found in first order  $\frac{\delta}{1-\delta} = \frac{\Lambda}{1-\delta} = \frac{\Lambda^2}{1-\delta} \approx \frac{x}{4}$ , so that

$$\chi = \frac{N\beta\mu_B^2}{3} \left[ g_S^2 S(S+1) + g_s^2 s(s+1) + \frac{\beta JS}{2} \left( g_S S - \frac{J}{|J|} g_s s \right)^2 \right], \quad (3.36)$$

and we note that only integer powers of the temperature are present.

To adjust Eq. (3.35) to the experimental data of Fig. 3.1, by setting  $g_S = g_s$ , Seiden identified  $J = 59.7$  and  $g = 1.9$ .

In another paper [94], Verdaguer *et al.*, by making use of the same classical approximation, centered on the transfer matrix technique, developed a numerical method for the calculation of the susceptibility yielding a more precise value of the intrachain coupling  $J = 43.6$  (as opposed to the value of  $J = 59.7$  found by way of Eq. 3.35). This new approach may be viewed as a refinement of the results discussed here, albeit not analytical.

In Fig. 3.2 (b), we sketch the alternating chain (ssS chain), with the zero-field ground state explicitly indicated, which was used to model the compound  $[\text{Mn}(\text{NITIm})(\text{NITImH})]\text{ClO}_4$ , from now on indicated as MnNN, where NITIm is a bis-chelating nitronyl nitroxide ligand, that was studied in the work by Fegy *et al.*

[111]. This chain can be expressed by a Hamiltonian of the form

$$\hat{H}_{ssS} = J \sum_{l=1}^{N-1} \hat{\mathbf{s}}_l \cdot (\hat{\mathbf{S}}_l + \hat{\mathbf{S}}_{l+1}) + J' \sum_{l=1}^N \hat{\mathbf{S}}_l \cdot \hat{\mathbf{s}}'_l, \quad (3.37)$$

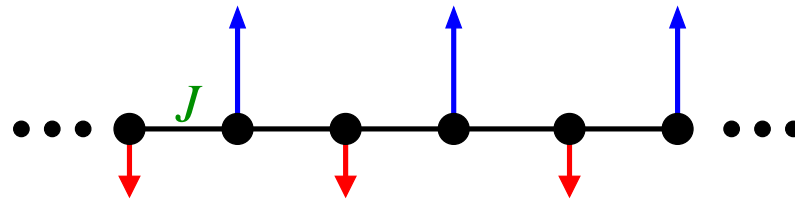
where  $\hat{\mathbf{s}}_l$  and  $\hat{\mathbf{s}}'_l$  are spin-1/2 variables (nitronyl nitroxide radical) and  $\hat{\mathbf{S}}_l$  are spin-5/2 variables (ion  $\text{Mn}^{II}$ ). By using this semiclassical approximation, where the spin-5/2 are treated as classical vectors, they calculated a closed expression for the susceptibility in an analogous way, namely

$$\chi = \frac{N\beta g^2 \mu_B^2}{3} [S^2 + s(s+1) + s'(s'+1) - St + \frac{1}{1-\delta}(-4S\Lambda + 2\Lambda^2 + 2\Lambda t) + \frac{\delta}{1-\delta} \left( 2S^2 - 2St + \frac{t^2}{2} \right)], \quad (3.38)$$

where  $t = \tanh(J'\beta s)$ , with  $\delta$  and  $\Lambda$  as defined previously..

In the next section we will apply FTLM [150] to finite-size chains described by the Hamiltonians given by Eqs. (3.4) and (3.37), for the case where  $s = s' = 1/2$  and  $S = 5/2$ . The results so produced will be put together in the context of experimental data [93, 94, 111] as well as calculations from other theoretical approaches, namely, the semiclassical magnetic susceptibility expressed by Eqs. (3.35) and (3.38) and spin-wave results [143, 147, 149, 151] and then comparisons will be drawn. Thus a brief review of FTLM is in order. This is provided in Appendix A.2.

(a): sS chain



(b): ssS chain

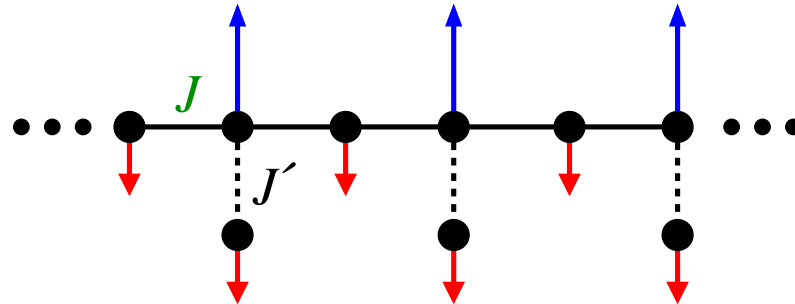


Figure 3.2: Schematic representation of the Hamiltonian and ground-state magnetic order of the (a) sS and (b) ssS alternating chains. In Seiden's paper [141] the larger spin (longer arrow) is a classical quantity, the other one being quantum.

### 3.4 Alternating spin-1/2 spin-5/2 ferrimagnetic chains - ground state and thermodynamics

We now present ED and FTLM results for the ground state and thermodynamic functions. Whenever possible, we bring together pertinent experimental data as well as results from other theoretical approaches for the sake of comparison. From now on, differently from the previous subsection, the number of magnetic sites in the chain will be indicated with the letter  $N$ , so that the sS chain has  $N/2$  cells and the ssS chain,  $N/3$  cells. To avoid confusion, the number of cells will be appropriately indicated by  $N_c$ .

#### 3.4.1 Ground states - ED results

##### One-magnon bands

In Figs. 3.3 and 3.4 we display one-magnon bands for the sS and ssS chains, respectively. For the sS chain, where we have set  $J = 44.8K$  (see Subsection 3.4.2, Fig. 3.10), the ground state of a system with  $N_c$  cells is found to be ferrimagnetic with total spin  $S_G = 2N_c$ . The bands show that there is a gapless excitation to a state with spin  $S_G - 1$  and a gapped one to a state with spin  $S_G + 1$ . Testing for various sizes we can infer the size of the gap  $\Delta$ , and so we have arrived at  $\Delta = 4.90J$ . In the respective figure appear also plots of the dispersion relations from the calculations

of non-interacting spin waves of Ref. [143], for  $s_1 = 1/2$  and  $s_2 = 5/2$ , namely

$$\begin{aligned}\omega_{1q} &= J(-s_1 + s_2) + \omega_q, \\ \omega_{2q} &= J(s_1 - s_2) + \omega_q, \\ \omega_q &= J\sqrt{(s_1 - s_2)^2 + 4s_1s_2\sin^2(q/2)}.\end{aligned}\tag{3.39}$$

The acoustical mode (gapless) calculated through both approaches superimpose, whereas the optical mode (gapped) does not: the non-interacting spin-wave dispersion is different and has a smaller gap, as is often the case with other mixed-spin systems. See, for example, Ref. [151]. With respect to the ssS chain, where we have set  $J'/J = 1.7$  (see Subsection 3.4.2, Fig. 3.11), similar results were produced, with a lesser value for the gap ( $\Delta = 3.88J$ ). We have not found in the literature calculations of the dispersion relations for this chain topology, which could be taken for referral.

### Magnetization

In Fig. 3.5 we show the magnetization per cell for the sS chain as a function of the applied magnetic field. The first plateau ends at a field  $b_c = g\mu_B B_c/J \approx 4.9$ , which corresponds to the gap of the first antiferromagnetic excitation already shown in Fig. 3.3. This corresponds to a huge field that must be turned on to bridge this gap ( $B_c \sim 150T$ ). To reach the saturation point, we need a very high field  $B_S = Jb_S/g\mu_B \sim 200$  T. In order to estimate the thermodynamic-limit transition pathway, we have used various chain sizes. Next we exhibit in Fig. 3.6 the magnetization of the ssS chain, which conveys a similar pattern of behavior. The first plateau ends at  $b_c = g\mu_B B_c/J \approx 3.9$ , which is the spin-wave gap height of Fig. 3.4.



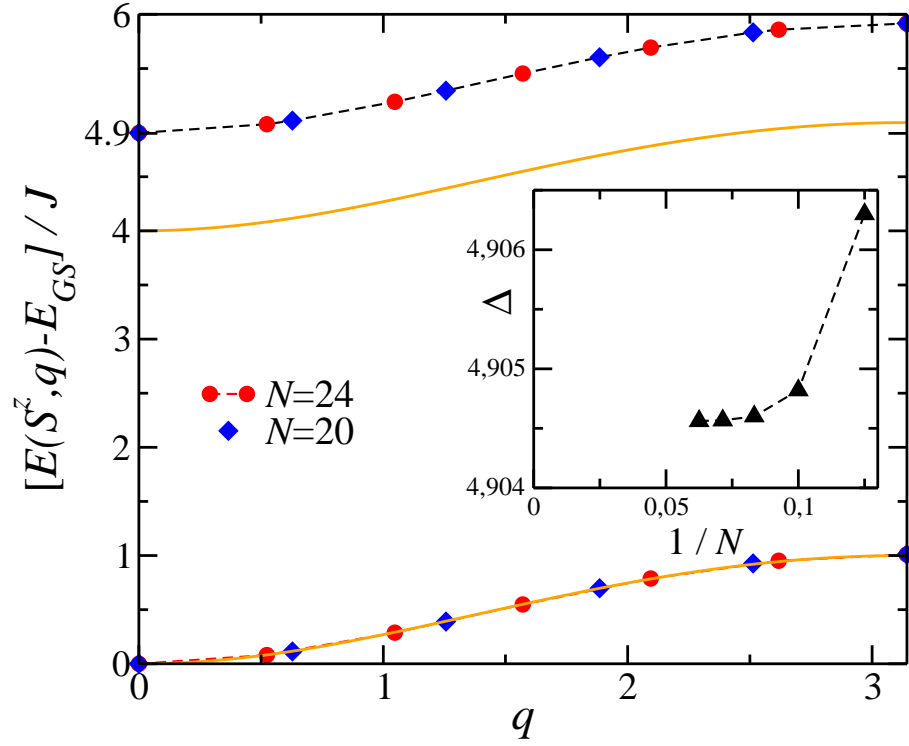


Figure 3.3: One-magnon bands of the sS chain. Full lines are spin-wave results from Ref. [143], while dashed lines are guides to the eyes.  $S^z = S_G - 1$  for the lower band, while  $S^z = S_G + 1$  for the upper one. Inset: Size dependence of the antiferromagnetic gap  $\Delta$ , which is estimated to be  $\Delta = 4.9046J$  in the thermodynamic limit.

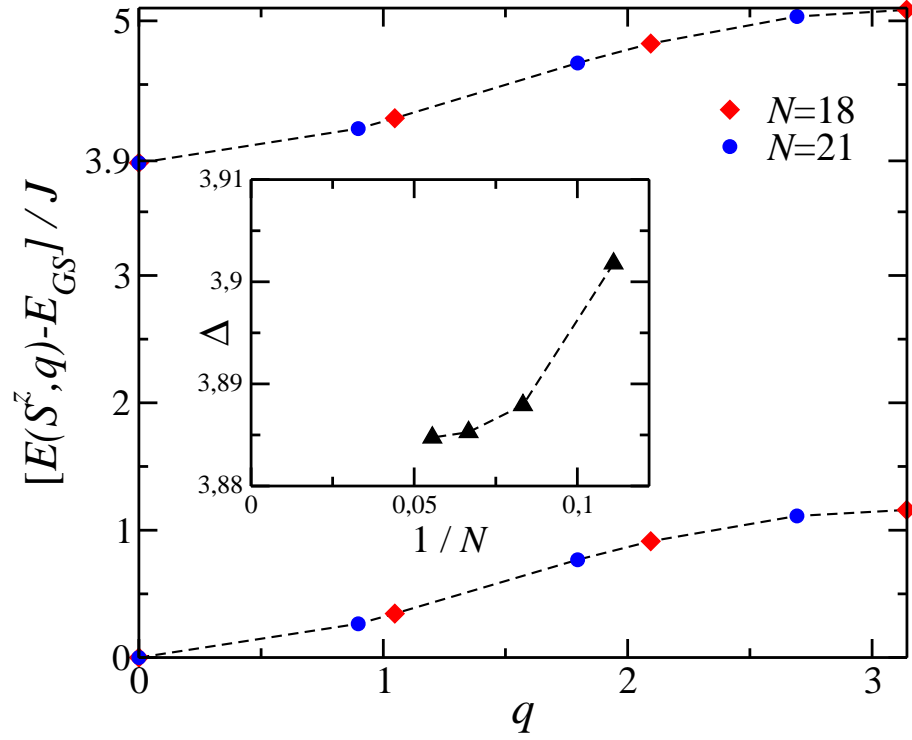


Figure 3.4: One-magnon bands of the ssS chain with  $J' = 1.7J$ . Dashed lines are guides to the eyes.  $S^z = S_G - 1$  for the lower band, while  $S^z = S_G + 1$  for the upper one. Inset: Size dependence of the antiferromagnetic gap  $\Delta$ , which is estimated to be  $\Delta = 3.88J$  in the thermodynamic limit.

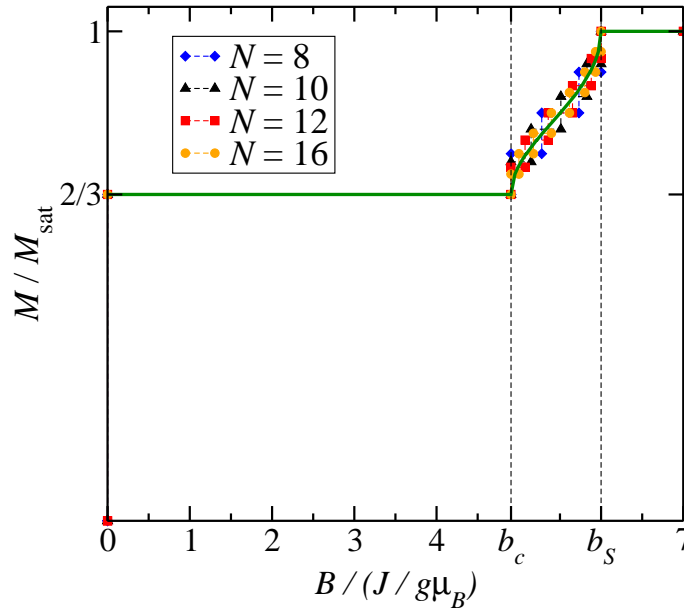


Figure 3.5: Magnetization per cell  $M$  normalized by its saturation value  $M_{sat} = 3g\mu_B$  as a function of applied magnetic field  $B$  in units of  $J/g\mu_B$  at  $T = 0$  for the sS chain. We have set  $J = 44.8K$  (see Subsection 3.4.2, Fig. 3.10). The first plateau ends at  $b_c = g\mu_B B_c/J \approx 4.9$  which implies that  $B_c \sim 150$  T. On the other hand, the saturation field  $B_S = Jb_S/g\mu_B \sim 200$  T.

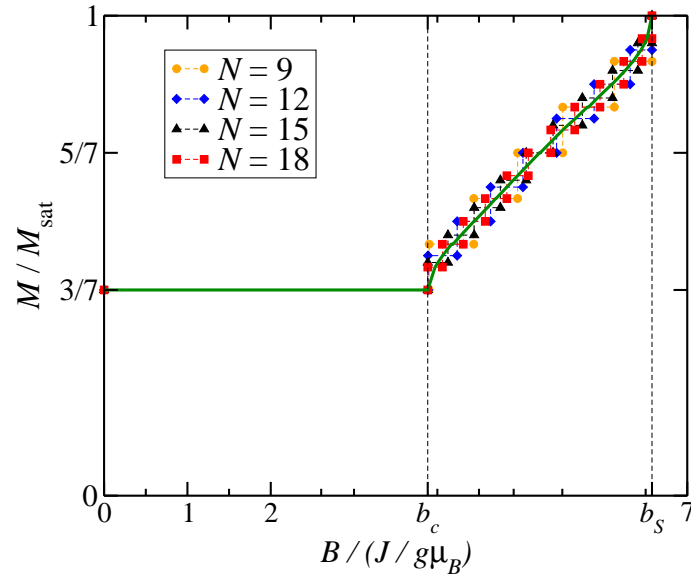


Figure 3.6: Magnetization per cell  $M$  normalized by its saturation value  $M_{sat} = 3.5g\mu_B$  as a function of applied magnetic field  $B$  in units of  $J/g\mu_B$  at  $T = 0$  for the ssS chain with  $J' = 1.7J$  (see Subsection 3.4.2, Fig. 3.11). The first plateau ends at  $b_c = g\mu_B B_c/J \approx 3.9$  which implies that  $B_c \sim 400T$ . On the other hand, the saturation field  $B_S = Jb_S/g\mu_B \sim 600T$ .

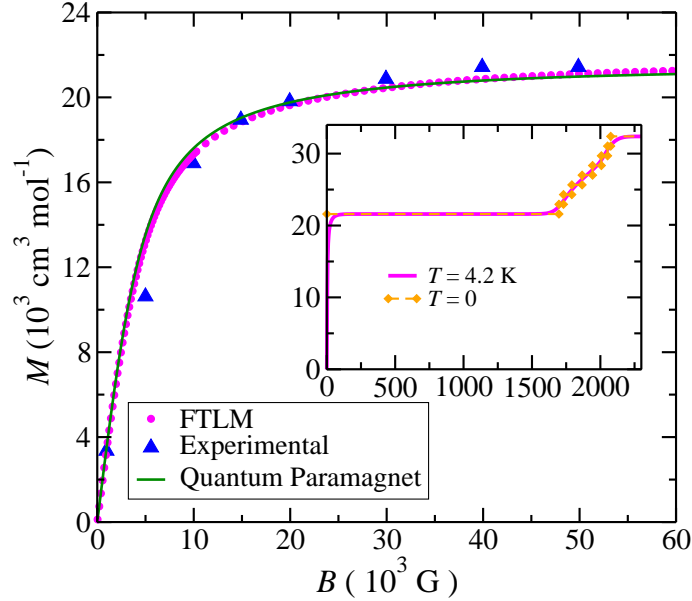


Figure 3.7: Magnetization per mol for the sS chain as a function of the applied magnetic field  $B$  for  $T = 4.2$  K. Experimental data of the compound CuMnDTO from Ref. [94, 141]. FTLM for a system with  $N = 16$ ,  $J = 44.8$  K and  $g = 1.93$ . Quantum paramagnet: fitting of the FTLM data to the magnetization per mol of a quantum paramagnet (Brillouin function) with total spin  $S$ . Taking  $g = 1.93$ , the best fit implying  $S = 15.8$ . The inset serves the purpose of showing how the finite temperature modifies the field-induced Lieb-Mattis ferrimagnetic ground state.

### 3.4.2 Thermodynamic quantities

The study of the thermodynamic functions is carried out through the numerical implementation of the FTLM on chains of finite size. Unless expressly indicated otherwise, we use in our FTLM computations  $M = 50$  for both sS and ssS chains, while setting  $R = 40000$  for the former and  $R = 50000$  for the latter. Periodic boundary conditions were used. When not explicitly shown, we have deemed convenient to set  $k_B = 1$  throughout this section.

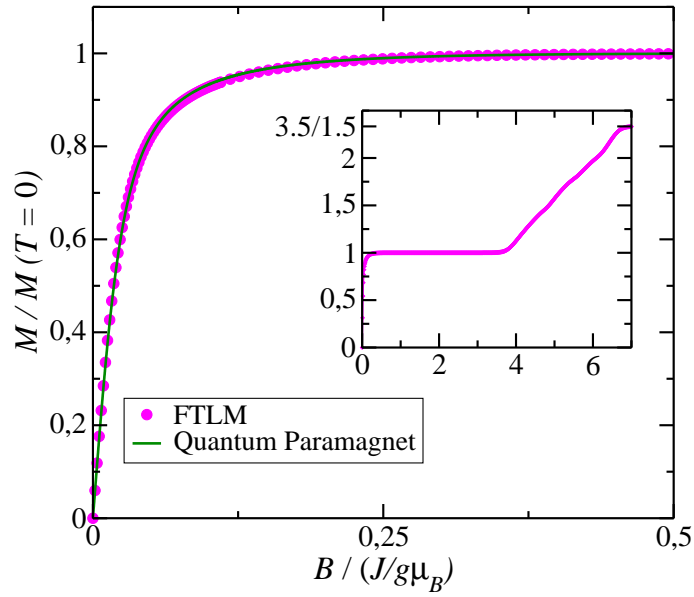


Figure 3.8: FTLM results for the magnetization normalized by its value at  $T = 0$  ( $M(T = 0) = 1.5$  per cell) for the ssS chain as a function of the normalized applied magnetic field at  $T = 0.1J$ . The system size is  $N = 18$ . Quantum paramagnet: fitting of the FTLM data to the expected curve for a quantum paramagnet (Brillouin function) with total spin  $S$ , the best fit implying  $S = 8.74$ . The inset serves the purpose of showing how the finite temperature modifies the field-induced Lieb-Mattis ground state.

### Magnetization

In Fig. 3.7 we show the FTLM results of the molar magnetization as a function of the applied magnetic field for  $T = 4.2K$ . The experimental data [94, 141] for the compound CuMnDTO are also included. A good agreement between both results is observed. We have also contemplated the magnetization  $M(B, T)$  of the quantum paramagnet given by the Brillouin function, namely

$$\begin{aligned} B_J(x) &= \frac{1}{S} \left\{ (S + 1/2) \coth[(S + 1/2)x] - \frac{1}{2} \coth\left(\frac{x}{2}\right) \right\}, \\ M(B, T) &= Ng\mu_B J B_J(x), \end{aligned} \quad (3.40)$$

where  $x = g\mu_B B/k_B T$ , and  $B$  is the applied magnetic field. Eq. (3.40) is also plotted and fitted to the FTLM data. Taking  $g = 1.93$ , and chain size  $N = 16$ , we attain the best fit by setting  $S = 15.8$ . This means that the spins are stirred thermally, so that the total spin is less than its field-induced Lieb-Mattis ferrimagnetic ground-state value, that is,  $S_{Lieb} = 16$ . We then envision an ensemble formed by insulated spin-15.8 units in a thermal bath, i.e., a quantum paramagnet, no less. We have proceeded in the same way relative to the ssS chain and display the results in Fig 3.8: a good fit is verified by using  $S = 8.74$ , which because of ensuing thermal fluctuations is less than the total spin  $S_{Lieb} = 9$  of the field-induced Lieb-Mattis ferrimagnetic ground state.

### Magnetic susceptibility

In Fig. 3.9 we present the product of the susceptibility per site by the temperature as a function of the temperature -  $(\chi T \times T)$  - for the sS chain. The chain size is  $N = 16$ . The characteristic 1D ferrimagnetic minimum takes place at  $T_m = 2.9J$ ,

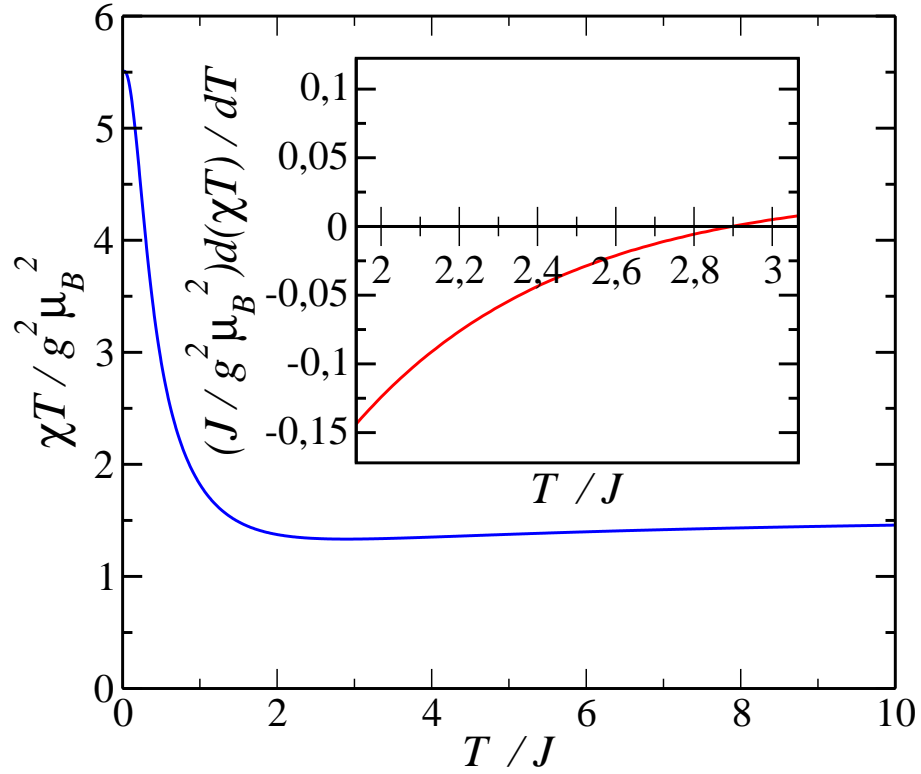


Figure 3.9: Product of the susceptibility per site  $\chi$  and the temperature  $T$  for the sS chain with  $N = 16$ . In the inset we present the derivative of this curve in the temperature range in which its minimum,  $T_{min} = 2.9J$ , is found.



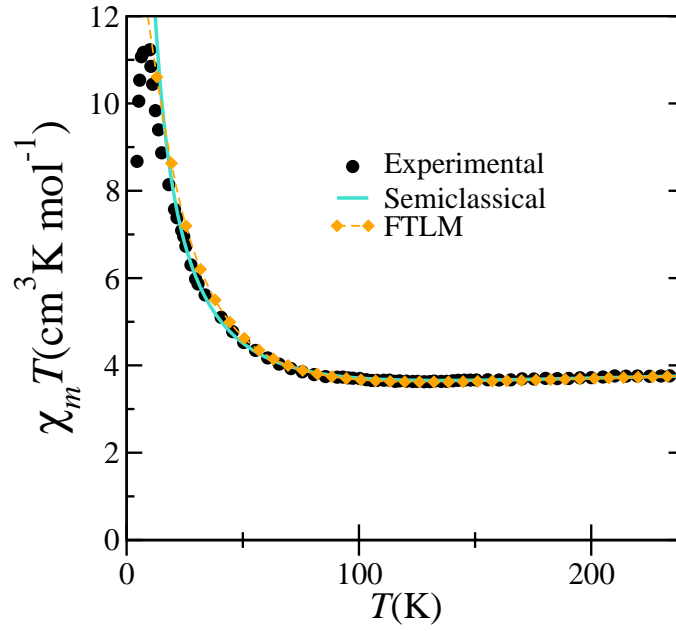


Figure 3.10: Product of the molar susceptibility  $\chi_m$  and temperature  $T$  as a function of  $T$  for the sS chain. Experimental data for the compound CuMnDTO from Ref. [141]. Semiclassical susceptibility according to Eq. (3.35):  $J = 59.7$  K,  $S = 2.5$  and  $g = 1.9$ . FTLM results for a system with  $N = 16$ , the best fit to the experimental data implies  $J = 44.8$  K and  $g = 1.90$ .

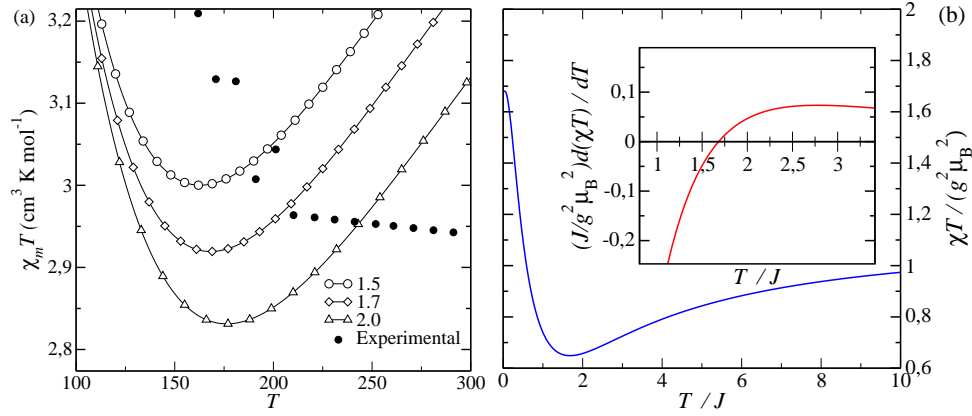


Figure 3.11: Product of the susceptibility per site  $\chi$  and the temperature  $T$  for the ssS chain with  $N = 18$ . (a) The numerical data, for the indicated values of  $J'/J$ , are compared with the experimental data for the compound MnNN from Ref. [111] by arbitrarily defining  $J = 100\text{K}$ , in order to enhance graph readability. (b)  $\chi T$  for  $J' = 1.7J$  and its derivative, shown in the inset. The minimum of this curve is found at  $T_{min} = 1.7J$ .

calculated in the way indicated in the inset, through the numerical derivative. Then in Fig. 3.10 we put together our FTLM results, the semiclassical susceptibility (Eq. (3.35)), and the experimental data [94, 141] for the compound CuMnDTO. By using Eq. (3.35), Seiden estimated  $J = 59.7\text{K}$  and  $g = 1.9$ . The best fit of our FTLM results to the experimental data yielded  $J = 44.8\text{K}$  and  $g = 1.90$ . Our estimate of  $J$  is closer to the one obtained through other numerical approach [94] to which we have already referred in Subsection 2.3.5. The evaluation of  $J$  is made by using the value of  $T_{min} = 130\text{K}$ , which indicates the minimum of the experimental curve. We see that both FTLM and semiclassical approaches agree with experiment in the mid- and high-temperature regimes. This is the regime where the interchain interactions can be considered negligible. Otherwise, and with the concurrence of other factors, the system seems to evolve toward a 3D long-range ferromagnetic

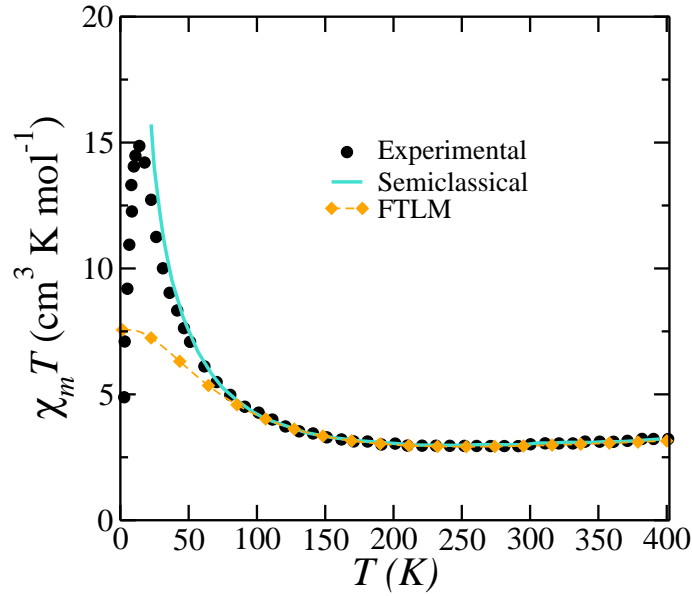


Figure 3.12: Product of the molar susceptibility  $\chi_m$  and temperature  $T$  as a function of  $T$  for the ssS chain. Experimental data of the MnNN compound from Ref. [111]. Semiclassical susceptibility according to Eq. (3.38):  $J = 144$  K,  $J' = 248$  K,  $S = 2.5$  and  $g = 2.0$ . FTLM results for a system with  $N = 18$ , the best fit to the experimental data implies  $J = 150$  K and  $J' = 255$  K, while  $g(= 2.0)$  is not taken as a fitting parameter.

ordering, and therefore, we are unable to push further with our simple 1D model in the quest of explaining experimental data, for this material and the like.

Next, in Fig. 3.11. we show the temperature dependence of  $\chi T$  for the ssS chain. The ratio  $J'/J$  nearest the experimental data is determined as indicated in Fig. 3.11 (a). The ubiquitous characteristic minimum is estimated as in the previous case and is shown in Fig. 3.11 (b). Next we present in Fig. 3.12 the FTLM and semiclassical results (Eq. (3.38)), derived ad hoc for this chain, alongside the experimental data of the MnNN compound. The FTLM results stray from the other two below a certain temperature. We cannot but impute to finite-size effects the discrepancy of the FTLM procedure, a hindrance which is unfortunately difficult to be bypassed by means of the present technique alone, because of machine limitations.

### Specific heat

In Fig. 3.13 we show the specific heat at zero applied field for both sS and ssS chains. The outstanding features are the double peaks, which are reminiscent of the Schottky effect [149, 151, 152]. This phenomenon is actually observed in the laboratory [96]. We also drew the respective Schottky specific heat curves. We see that the ssS and Schottky curves fit together nicely, and furthermore the peak height that comes out agrees with the spin-wave band gap - the Schottky energy gap  $\delta \approx 4.1J$  being just a bit over the expected value, to wit  $\Delta = 3.9j$ . But we seem to have a problem with respect of the fit to the sS chain: we do not get so good an adjustment as with the other chain. To verify if a reasonable adjustment was ever possible, we then worked based on the faint premise that the first left-hand peak somehow strongly influences the higher one, whereas this does not happen with the ssS chain, whose first peak is almost nonexistent, appearing as a mere inflection

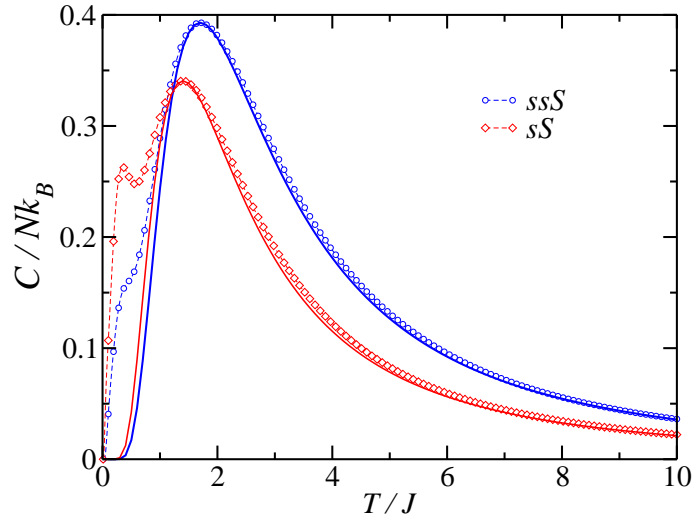


Figure 3.13: Specific heat per site as a function of temperature  $T$  for sS and the ssS, with  $J' = 1.7J$ , chains. The full lines are the respective Schottky specific heats (Eq. (3.41)). Dashed lines are guides to the eye.

point. We finally opted to calculate the specific heat of the sS chain with an applied magnetic field. Our surmise: by using such stratagem, we end up winnowing, upon increasing the field intensity, unwanted low-energy states, and as a result the first peak which in turn is made up of these states vanishes, so that a configuration similar to that of the ssS chain is produced. The peak height initially shifts to the right and then reverses this trend with increasing field. A possible explanation: at lower fields mid-energy states still compound the first peak, enhancing its importance, but as the field is augmented higher energy states (second band) are activated and become available even at lower temperatures and so that the second peak gains dominance and trails back on the temperature scale.

We now try to elaborate on how the fitting and evaluation of the gap is made.

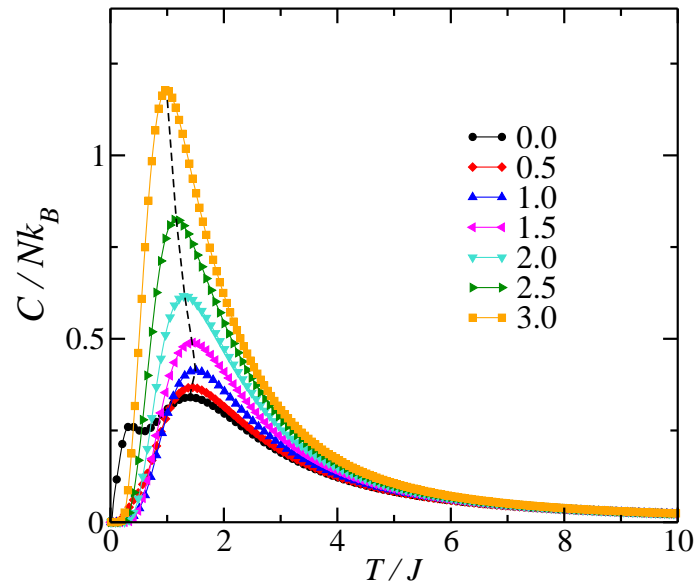


Figure 3.14: Specific heat per site as a function of temperature  $T$  of the sS chain, for various intensities of the applied magnetic field, as indicated. The height position wanders to the right and then back to the left.

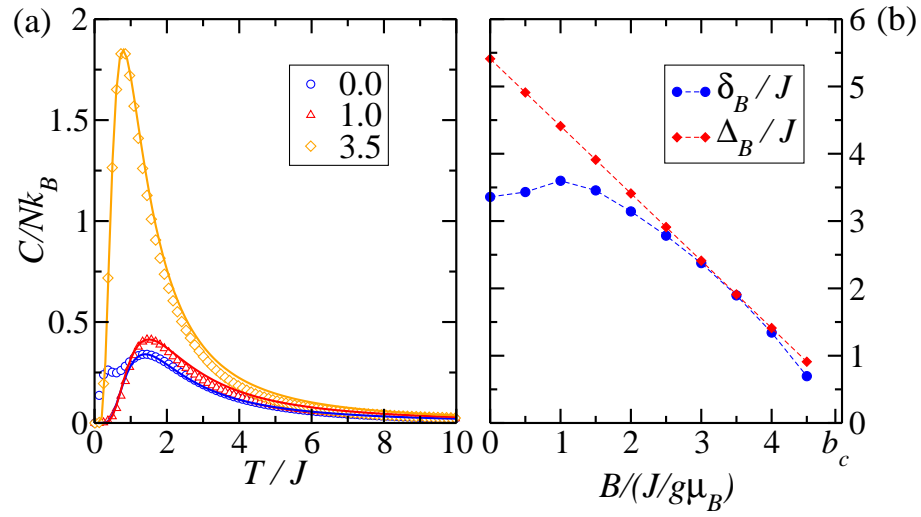


Figure 3.15: (a) Specific heat per site as a function of temperature  $T$  of the sS chains, for various intensities of the applied magnetic field. The full lines represent the respective Schottky specific heat. (b) Schottky  $\delta_B$  (Eq. (3.41)) and chain  $\Delta_B$  gaps as functions of the applied field (Eq. (3.43)). At  $B/(J/g\mu_B) \approx 3.5$ , we find that  $\delta_B \approx \Delta_B$ .

For this goal, we use the Schottky specific heat formula of Ref. [149]:

$$f = \frac{C}{Nk_B} = (Ar) \frac{(\beta\delta)^2 e^{\beta\delta}}{(e^{\beta\delta} + r)^2}, \quad (3.41)$$

where  $A$  is an adjustable parameter,  $r = 1$ , in the thermodynamic limit, and  $\delta$  is the Schottky gap. Setting  $\tilde{f} \equiv f/A$  and  $\tilde{T} \equiv T/\delta$ , with  $k_B \equiv 1$ , we get

$$\tilde{f} = \left(\frac{1}{\tilde{T}}\right)^2 \frac{e^{1/\tilde{T}}}{(e^{1/\tilde{T}} + 1)^2}, \quad (3.42)$$

which upon maximizing yields  $\tilde{f}_{max} = 0.439229$  and  $\tilde{T}_{max} = 0.416778$ , so that  $f_{max} = 0.439229A$  and  $T_{max} = 0.416778\delta$ . From  $T_{max}$  and  $f_{max}$  read off from the specific-heat plots for the sS chain in a given applied magnetic field  $B$ , we determine the parameters  $A(B)$  and the gap  $\delta(B)$ , and so the fitting process is complete. By using the magnon bands, we can also determine the chain specific-heat gap dependence with the applied field ( $\Delta(B)$ ), namely

$$\Delta(B) = \Delta_0 - B, \quad (3.43)$$

where  $\Delta_0$  is the gap at zero field measured from the middle of the second band, i.e.,  $\Delta_0 = 5.4$ . The *best* fit will come about when  $\delta(B) = \Delta(B)$  for a certain field  $B$  as shown in Fig. 3.15 (b), that is, for this value of the applied field both Schottky and band gap coincide.

### Magnetic susceptibility at the low-temperature regime ( $T < J$ )

We now attempt to explore the temperature regime where ferromagnetic excitations tend to be a predominant feature. For the compounds treated here the in-



trachain interaction ( $J \approx 50\text{K}$ ) is relatively small, so that temperatures within this range may be considered low in a certain sense. On the other hand, for some one-dimensional ferrimagnets formed by manganese (II) and nitronyl nitroxides [109]<sup>2</sup>, the characteristic minimum occurs above room temperature and the coupling constant is evaluated at  $J \approx 260\text{cm}^{-1} = 374\text{K}$ , and even higher values can be found among materials composed of nickel (II) and nitronyl nitroxides [108], for which the intrachain interaction is found to be  $J = 424\text{cm}^{-1} = 610\text{K}$  (to operate the  $\text{cm}^{-1} \leftrightarrow \text{K}$  coupling conversion we use the value of  $k_B$  expressed in  $\text{cm}^{-1}/\text{K}$ , i.e.  $k_B = 0.6950356\text{cm}^{-1}/\text{K}$ ). So, in many occasions the expression *low temperature* in the context of this subsection, may be quite misleading. What we do intend actually is to fix a narrow *normalized* low-temperature interval  $0 \leq T/J \leq 1$  and get a close-up view of the behavior of 1D chains as far as various theoretical and experimental results are concerned. This is the regime wherein the materials under study undergo a 3D ordering toward  $T/J \ll 1$ , so that our present models fail to provide a faithful picture of their magnetic behavior in the vicinity of the transition temperature and below.

In Fig. 3.16 we have made FTLM simulations for spin-1/2 linear *ferromagnetic* chains with 8 and 24 sites, and plotted the quantity  $\chi T^2/J(g\mu_B)^2$  as a function of  $T/J$ . We note that down to  $T/J \approx 0.3$ , both graphs superimpose, whereby we conclude that we have already attained the thermodynamic limit at and above this temperature value for such chain sizes. We then resort to the expansion formula of the modified spin-wave theory worked out by Takahashi [147], which up to second order in  $T/J$  reads

$$\chi = \frac{8}{3}S^4JT^{-2} \left[ 1 - \frac{3}{S} \frac{\zeta(\frac{1}{2})}{(2\pi)^{1/2}} \left( \frac{T}{2SJ} \right)^{1/2} + \frac{3}{S^2} \frac{\zeta^2(\frac{1}{2})}{2\pi} \frac{T}{2SJ} + O(T^{3/2}) \right], \quad (3.44)$$

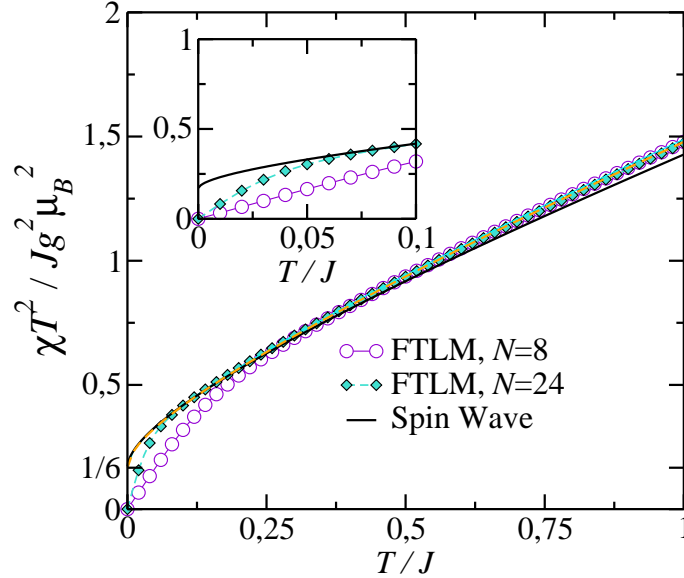


Figure 3.16: Product of the susceptibility per site  $\chi$  and the temperature  $T$  squared for the ferromagnetically coupled linear chain in the low temperature region,  $T < J$ . Spin-wave result up to second order in  $T/J$  from Ref. [147]. The temperature range  $T < 0.1J$  for which the spin-wave result is almost exact is shown in the inset. The FTLM calculations were made on spin-1/2 ferromagnetic linear chains.

where  $\zeta(z)$  is the Riemann zeta function. At  $S = 1/2$ , and by using  $\zeta(1/2) = -1.460354$ , this becomes

$$\chi = JT^{-2} \left[ \frac{1}{6} + 0.5825974(T/J)^{1/2} + 0.6788396(T/J) + O(T^{3/2}) \right], \quad (3.45)$$

whose graph is also included in Fig 3.16. As showed in Ref. [147], in the range  $0 < T/J < 0.1$ , the formula of Eq. (3.45) and the Bethe-ansatz integral equation [153, 154] yield the same results, and this serves to attest Takahashi's derivation as suitable in this temperature regime. So, we could take advantage of this fact and even push a bit further the temperature lower value ( $T/J \approx 0.08$ ) of the range

in which our FTLM results, for  $N = 24$ , are valid in the thermodynamic limit, as shown in the inset of Fig. 3.16. On the other hand, for  $T/J \geq 0.5$ , the graph of Eq. (3.45) slopes down away from the FTLM duo, which indicates that the FTLM is better suited in the higher-temperature region.

Getting back to the sS chain, we now try to sort through the jumble of curves in Fig 3.17, plotted together to facilitate comparison. Firstly, we examine the FTLM results for  $N = 14$  and  $N = 16$ , and we note that both graphs coincide as far down as  $T/J \approx 0.5$ , and so they converge to the thermodynamic limit for temperatures equal or above that point. The experimental data normalized by  $J = 44.8K$  and  $J = 59.7K$  show the expected agreement with the FTLM results and the semiclassical formula, respectively - Eq. (3.35) - as already displayed in Fig. 3.10. The modified-spin-wave result comes from the expansion formula derived by Yamamoto *et al.* [149], up to second order in  $T/J$ :

$$\frac{\chi J}{N(g\mu_B)^2} = \frac{Ss(S-s)^2}{3}t^{-2} - (Ss)^{1/2}(S-s)^{3/2}\frac{\zeta(\frac{1}{2})}{\sqrt{2\pi}}t^{-3/2} + (S-s)\left[\frac{\zeta(\frac{1}{2})}{\sqrt{2\pi}}\right]^2 t^{-1} + O(t^{-1/2}), \quad (3.46)$$

where  $t = T/J$ . We then have set  $s = 1/2$  and  $S = 5/2$ , to obtain

$$\frac{\chi J}{N(g\mu_B)^2} = \frac{5}{3}t^{-2} + 1.842334t^{-3/2} + 0.678839t^{-1} + O(t^{-1/2}). \quad (3.47)$$

Evidently, we do not seem to boast a good agreement with any of the other data whatsoever. To get a closer look, we fitted to the FTLM results a function of the form  $[\frac{5}{3} + a_0(\frac{T}{J})^{\frac{1}{2}} + a_1(\frac{T}{J})]$ , where integer and half-integer powers of  $T$  appear. The estimated values of the coefficients were  $a_0 = 1.28$  and  $a_1 = 0.69$ . A good fit is apparent only in the interval  $0.5 < T/J < 0.9$ , where the FTLM results already represent the thermodynamic limit. By the way, one should stress that while the

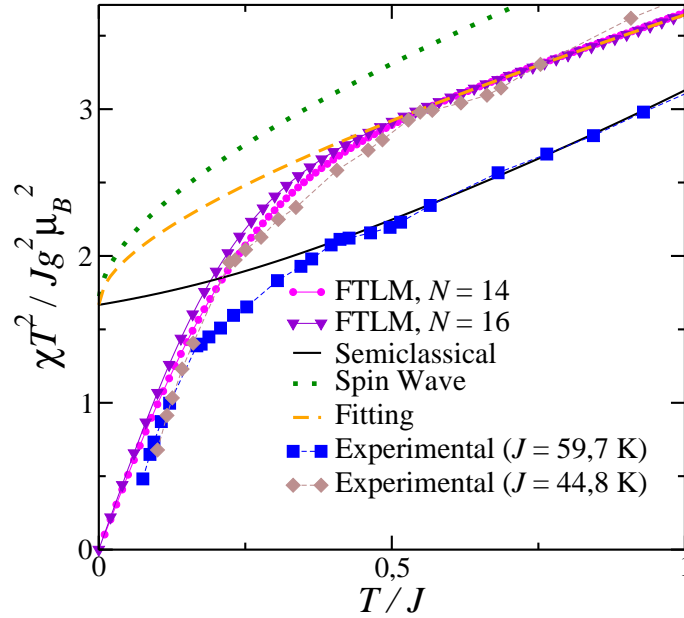


Figure 3.17: Product of the normalized susceptibility  $\chi$  per unit cell and the temperature  $T$  squared. FTLM data were obtained for the indicated system sizes. The semiclassical result comes from Eq. (3.35). Modified spin-wave results up to second order in  $T/J$  from Ref. [149]. The FTLM result for  $0.5 < T/J < 0.9$  is fitted to a function of the form  $[\frac{5}{3} + a_0(\frac{T}{J})^{\frac{1}{2}} + a_1(\frac{T}{J})]$  and  $a_0$  and  $a_1$  are estimated to be 1.28 and 0.69, respectively. Experimental results were normalized by taking  $J = 59.7$  K ( $g = 1.9$ ) and  $J = 44.8$  K ( $g = 1.85$ ), which must be compared with the semiclassical and FTLM results, respectively.

semiclassical, spin-wave and fitting results for  $\chi T^2 / J(g\mu_B)^2$  approach the constant value  $sS(S-s)^2/3 = 5/3$  as  $(T/J) \rightarrow 0$ , the FTLM results and the experimental data cross over to zero. Here one must distinguish two effects: with respect to FTLM, this is evidently a manifestation of finite-size effects, while for the experimental data one can attribute this to the 1D/3D crossover affecting them, where the critical exponent  $\gamma < 2$ , which entails  $\chi T^2 / J(g\mu_B)^2 \rightarrow 0$ , as one obviously has the power law  $\chi \sim T^{-\gamma}$  obeyed in this region.

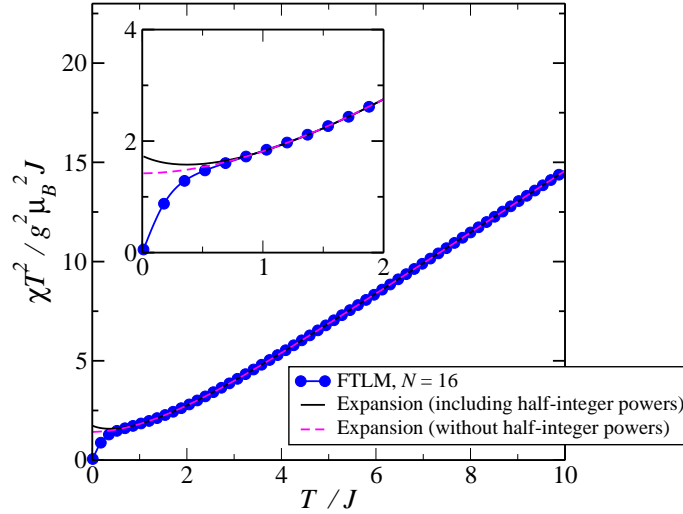


Figure 3.18: Product of the susceptibility per site  $\chi$  and the temperature  $T$  squared for the sS chain. Inset: Temperature region  $0 < (T/J) < 2$ . Best fit, in the region  $T > 0.8J$ , to a function as  $a_0 + a_1x^{0.5} + a_2x + a_3x^{1.5} + a_4x^2 + a_5x^{2.5}$ , with  $x = T/J$ , implies  $a_0 = 1.73$ ,  $a_1 = 0.12$ ,  $a_2 = -1.83$ ,  $a_3 = 2.40$ ,  $a_4 = -0.65$  and  $a_5 = 0.06$ ; while if the fitting function is  $a_0 + a_1x + a_2x^2 + a_3x^3 + a_4x^4 + a_5x^5$ , the best parameters are  $a_0 = 1.4211$ ,  $a_1 = 0.0289$ ,  $a_2 = 0.4255$ ,  $a_3 = -0.0623$ ,  $a_4 = 0.0046$  and  $a_5 = -0.0001$ .

A look in the literature [72, 133, 141] leads us to infer that classical systems contribute integer powers of the temperature for the magnetic susceptibility, while in the quantum case also half-integer contributions arise and may be linked to low-temperature spin-waves [147]. In Fig. 3.18 we provided fits to the FTLM results comprising two polynomials: one which contains exclusively integer powers of the temperature, while the second includes *both* integer and half-integer contributions. We note that the best fit occurs for  $T/J > 0.8$ , where all three graphs superimpose exactly, and this must be the region where the classical results are satisfactory. Lastly, one should notice the presence of finite-size effects in the FTLM results as  $(T/J) \rightarrow 0$ .

## 3.5 Summary and conclusions

We have so far highlighted the importance of 1D systems in present-day research in the field of molecular magnetism - both theoretical and experimental. One area of endeavor is to build more complex assemblages capable of exhibiting bulk magnetism at higher and higher temperatures, starting with the so-called low-dimensional materials, such as the ones referred to in this work. On the other hand, quasi-1D systems are very interesting objects on their own and continue to attract the attention of physicists and chemists from all over the world. The discovery of SMMs and SCMs opened up a new era of activity with research directed to the efficient design of magnetic materials that can be tailored to suit specific needs.

In this chapter, we have principally devoted our attention to an important subset of the quasi-1D materials - the compounds that can be fairly modeled by ferrimagnetic alternating quantum spin-1/2 spin-5/2 chains. We have gathered experimental data of a couple of compounds, namely CuMnDTO and MnNN, the former described by the sS chain and the latter by ssS chain, down to the neighborhood of a certain critical temperature whereon a phase transition to a 3D ferromagnetic ordering takes place. We have concentrated our efforts on applying the finite-temperature Lanczos method (FTLM) to finite-size chains. The magnetic susceptibility, magnetization and specific heat were calculated and the thermodynamic limit estimated for certain temperature regimes. Interesting features in the specific heat as well as in the magnetization were brought to light. The ground-state magnetization and excitation gap were also studied by way of an exact diagonalization procedure (ED); the one-magnon bands for the sS chain were compared with spin-wave results. In addition, we have carried out a comparison of the FTLM results with the semiclassical approach as well as the experimental data concerning the magnetic susceptibility,

and as shown in the figures, and good overall agreement was attained.

Next we have probed further the magnetic susceptibility in the special temperature regime  $0 < T/J < 1$ , now taking into account results from modified spin waves. In particular, the Takahashi expansion formula for low temperature was used and it showed that the FTLM results could converge to the thermodynamic limit in a temperature range that reaches down to very low temperatures. It became clear that the FTLM results are bested by the spin-wave approach in the very low-temperature regime. Finite-size effects are to blame for this setback, although other culprits inherent in the FTLM technique proper may play a part. All told, the FTLM results revealed themselves as reliable and convergence to the thermodynamic limit with relatively small chain sizes, for a wide temperature range, was verified. As already stated, we have not yet considered interacting spin waves results and we intend to do so in the near future. Evidently, near and below the 3D-ordering temperature none of the instruments used so far are adequate and much work is currently under way worldwide in the attempt to explain the intricate behavior of the physical systems in this regime.

In toto, we have explored to some extent the thermodynamics of these interesting systems and touched upon the rich gamut of features that they exhibit, and the potentiality of FTLM in the study of 1D systems was reasonably demonstrated .

# Appendix A

## Appendix

### A.1 The Basis of monopole harmonics states

The appropriate Hilbert space is made up of *angular section* states, which are eigenstates of Eq. (2.20), for which the following are true [52]:

$$\hat{\mathbf{L}}^2|q, l, m\rangle = l(l+1)|q, l, m\rangle; \quad \hat{L}_z|q, l, m\rangle = m|q, l, m\rangle, \quad (\text{A.1})$$

where

$$l = |q|, |q| + 1, |q| + 2, \dots, m = -l, -l + 1, \dots, l. \quad (\text{A.2})$$

In particular,

$$\begin{aligned} \hat{L}_+|q, l, m\rangle &= \sqrt{(l-m)(l+m+1)}|q, l, m+1\rangle, \\ \hat{L}_-|q, l, m\rangle &= \sqrt{(l+m)(l-m+1)}|q, l, m-1\rangle. \end{aligned} \quad (\text{A.3})$$



where  $\hat{L}_\pm = \hat{L}_x \pm i\hat{L}_y$  are the usual ladder operators. Here the operator  $\hat{\mathbf{L}}$  is given by Eq. (2.21) and the vector potential is conveniently expressed by Eq. (2.22). The  $|q, l, m\rangle$  are the so-called eigensections also known as *monopole harmonics*. For a given *region*  $a$  or  $b$  around the magnetic monopole [52], the explicit form of the monopole harmonics, also most frequently referred to by the notation  $Y_{q,l,m}$ , reads

$$\begin{aligned} (Y_{q,l,m})_a &= M_{q,l,m} (1-x)^{\alpha/2} (1+x)^{\beta/2} P_n^{(\alpha,\beta)}(x) e^{i(m+q)\phi}, \\ (Y_{q,l,m})_b &= (Y_{q,l,m})_a e^{(-2iq)\phi}, \end{aligned} \quad (\text{A.4})$$

with the following definitions

$$\alpha = -q - m, \quad \beta = q - m, \quad n = l + m, \quad x = \cos \theta; \quad (\text{A.5})$$

$$M_{q,l,m} = 2^m \sqrt{\left[ \frac{(2l+1)}{4\pi} \frac{(l-m)!(l+m)!}{(l-q)!(l+q)!} \right]}; \quad (\text{A.6})$$

and  $P_n^{(\alpha,\beta)}(x)$  are the Jacobi polynomials [84],

$$P_n^{(\alpha,\beta)}(x) = \frac{(-1)^n}{2^n n!} (1-x)^{-\alpha} (1+x)^{-\beta} \frac{d^n}{dx^n} [(1-x)^{(\alpha+n)} (1+x)^{(\beta+n)}] \quad (\text{A.7})$$

which together with the orthogonality relation for the Jacobi polynomials [84], yield the orthogonality relation for the monopole harmonics

$$\int Y_{q,l',m'}^*(\theta, \phi) Y_{q,l,m}(\theta, \phi) d\Omega = \delta_{l'l} \delta_{m'm}. \quad (\text{A.8})$$

We now use the definition of the monopole harmonics and various recurrence relations of the Jacobi polynomials [84] to establish the following relations valid for all  $q$ :

$$\begin{aligned}
{}_l \left[ \frac{(l+m+1)(l-m+1)(l+q+1)(l-q+1)}{(2l+3)(l+m)(l-m)} \right]^{1/2} Y_{q,l+1,m}(\theta, \phi) &= \\
[l(l+1)\cos\theta + 2mq] \left[ \frac{2l+1}{(l+m)(l-m)} \right]^{1/2} Y_{q,l,m}(\theta, \phi) & \\
-(l+1) \left[ \frac{(l+q)(l-q)}{2l-1} \right]^{1/2} Y_{q,l-1,m}(\theta, \phi), & \quad (\text{A.9})
\end{aligned}$$

$$\begin{aligned}
[(1-x^2)e^{-i\phi}] \left[ \frac{1}{(l+m)(l+m-1)} \right]^{1/2} Y_{q,l-1,m+1}(\theta, \phi) &= \\
\frac{1}{l} \left[ \frac{(l+q)(l-q)(l-m-1)(l-m)}{(2l+1)(2l-1)(l+m)(l+m-1)} \right]^{1/2} Y_{q,l,m}(\theta, \phi) & \\
-\frac{q}{l(l-1)} \left[ \frac{l-m-1}{l+m-1} \right] Y_{q,l-1,m}(\theta, \phi) & \\
-\frac{1}{l-1} \left[ \frac{(l+q-1)(l-q-1)}{(2l-3)(2l-1)} \right]^{1/2} Y_{q,l-2,m}(\theta, \phi), & \quad (\text{A.10})
\end{aligned}$$

$$\begin{aligned}
[(1-x^2)e^{i\phi}] \left[ \frac{1}{(l-m+1)(l-m)} \right]^{1/2} Y_{q,l,m-1}(\theta, \phi) &= \\
-\frac{q(l+m)}{l(l+1)} \left[ \frac{1}{(l+m)(l-m)} \right]^{1/2} Y_{q,l,m}(\theta, \phi) & \\
-\frac{1}{(l+1)} \left[ \frac{(l+m)(l+m+1)(l+q+1)(l-q+1)}{(2l+1)(2l+3)(l-m+1)(l-m)} \right]^{1/2} Y_{q,l+1,m}(\theta, \phi) & \\
+\frac{1}{l} \left[ \frac{(l+q)(l-q)}{(2l+1)(2l-1)} \right]^{1/2} Y_{q,l-1,m}(\theta, \phi). & \quad (\text{A.11})
\end{aligned}$$

We then set  $\hat{n}_\pm = \hat{n}_x \pm i\hat{n}_y$ , similarly to  $\hat{L}_\pm$ , and put the following:  $x = \cos \theta$  and  $\hat{n}_z \rightarrow \cos \theta$ ,  $\hat{n}_+ \rightarrow e^{i\phi} \sin \theta$ . The last step is to make use the orthogonality relation for the monopole harmonics and specialize in the case  $q = \frac{1}{2}$  to get the respective non-zero matrix elements for the operator  $\hat{\mathbf{n}}$ , used in this work:

$$\langle \frac{1}{2}, l, m | \hat{n}_z | \frac{1}{2}, l, m \rangle = -\frac{m}{l(2l+2)}, \quad (\text{A.12})$$

$$\langle \frac{1}{2}, l+1, m | \hat{n}_z | \frac{1}{2}, l, m \rangle = \frac{1}{(2l+2)} \sqrt{(l+m+1)(l-m+1)}, \quad (\text{A.13})$$

$$\langle \frac{1}{2}, l, m | \hat{n}_z | \frac{1}{2}, l-1, m \rangle = \frac{1}{(2l)} \sqrt{(l-m)(l+m)}, \quad (\text{A.14})$$

$$\langle \frac{1}{2}, l, m | \hat{n}_- | \frac{1}{2}, l-1, m+1 \rangle = \frac{1}{2l} \sqrt{(l-m-1)(l-m)}, \quad (\text{A.15})$$

$$\langle \frac{1}{2}, l-1, m | \hat{n}_- | \frac{1}{2}, l-1, m+1 \rangle = -\frac{1}{2l(l-1)} \sqrt{(l+m)(l-m-1)}, \quad (\text{A.16})$$

$$\langle \frac{1}{2}, l-2, m | \hat{n}_- | \frac{1}{2}, l-1, m+1 \rangle = -\frac{1}{2(l-1)} \sqrt{(l+m)(l+m-1)}, \quad (\text{A.17})$$

$$\langle \frac{1}{2}, l, m | \hat{n}_+ | \frac{1}{2}, l, m-1 \rangle = -\frac{1}{2l(l+1)} \sqrt{(l-m+1)(l+m)}, \quad (\text{A.18})$$

$$\langle \frac{1}{2}, l+1, m | \hat{n}_+ | \frac{1}{2}, l, m-1 \rangle = -\frac{1}{2(l+1)} \sqrt{(l+m)(l+m+1)}, \quad (\text{A.19})$$

$$\langle \frac{1}{2}, l-1, m | \hat{n}_+ | \frac{1}{2}, l, m-1 \rangle = \frac{1}{2l} \sqrt{(l-m+1)(l-m)}. \quad (\text{A.20})$$

These can be grouped neatly together as follows (the matrix elements of  $\hat{n}_-$  are obtained by complex conjugation and this fact may be used as a check on the

correctness of relations expressed in Eqs. (A.10) and (A.11):

$$\begin{aligned}
\langle \frac{1}{2}, l, m | \hat{n}_z | \frac{1}{2}, l, m \rangle &= -\frac{m}{l(2l+2)}, \\
\langle \frac{1}{2}, l, m | \hat{n}_z | \frac{1}{2}, l-1, m \rangle &= \frac{1}{2l} \sqrt{(l-m)(l+m)}, \\
\langle \frac{1}{2}, l, m | \hat{n}_+ | \frac{1}{2}, l, m-1 \rangle &= -\frac{1}{2l(l+1)} \sqrt{(l-m+1)(l+m)}, \\
\langle \frac{1}{2}, l, m | \hat{n}_+ | \frac{1}{2}, l-1, m-1 \rangle &= -\frac{1}{2l} \sqrt{(l+m)(l+m-1)}, \\
\langle \frac{1}{2}, l, m | \hat{n}_+ | \frac{1}{2}, l+1, m-1 \rangle &= \frac{1}{2(l+1)} \sqrt{(l-m+1)(l-m+2)}. \quad (\text{A.21})
\end{aligned}$$

Furthemore, making use of the relation [52]

$$Y_{0,l,m}(\theta, \phi) = Y_{l,m}(\theta, \phi), \quad (\text{A.22})$$

we can take advantage of Eqs. (A.9), (A.10), and (A.11) to deduce the matrix elements for  $q = 0$ , instead of using the Legendre polynomials. This fact may come in handy as another test of the airtightness of our derivations.

With the ladder-operator relations given by Eqs. (A.3) and Eqs. (A.1) we get the nonzero matrix elements for  $\hat{\mathbf{L}}$ , which are valid for all  $q$ :

$$\begin{aligned}
\langle l, m | \hat{L}^2 | l, m \rangle &= l(l+1), \\
\langle l, m | \hat{L}_z | l, m \rangle &= m, \\
\langle l, m | \hat{L}_+ | l, m-1 \rangle &= [(l+m)(l-m+1)]^{1/2}. \quad (\text{A.23})
\end{aligned}$$

## A.2 Finite-temperature Lanczos method (FTLM)

### A.2.1 Overview

For completeness, we provide some highlights of FTLM by following the review by Jaklič and Prelovšek [150]. In the study of strongly correlated systems one is mostly faced with the problem of finding the eigenvalues and eigenvectors of very large matrices, which is not feasible with standard algorithms performing full diagonalization. One must instead resort to power algorithms, among which the Lanczos algorithm [63] is one of the most widely known. The core idea behind the Lanczos algorithm is that it begins with a normalized random vector  $|\phi_0\rangle$  in the vector space in which the Hamiltonian operator  $\hat{H}$  is defined. Then  $\hat{H}$  is applied to  $|\phi_0\rangle$  and the resulting vector is split up into components parallel to  $|\phi_0\rangle$ , and  $|\phi_1\rangle$  orthogonal to it, respectively,

$$\hat{H}|\phi_0\rangle = a_0|\phi_0\rangle + b_1|\phi_1\rangle. \quad (\text{A.24})$$

Since  $\hat{H}$  is Hermitian,  $a_0 = \langle\phi_0|\hat{H}|\phi_0\rangle$  is real, while the phase of  $|\phi_1\rangle$  can be chosen so that  $b_1$  be also real. In the next step,  $\hat{H}$  is applied to  $|\phi_1\rangle$ :

$$\hat{H}|\phi_1\rangle = b'_1|\phi_0\rangle + a_1|\phi_1\rangle + b_2|\phi_2\rangle, \quad (\text{A.25})$$

where  $|\phi_2\rangle$  is orthogonal to  $|\phi_0\rangle$  and  $|\phi_1\rangle$ . It follows also  $b'_1 = \langle\phi_0|\hat{H}|\phi_1\rangle = b_1$ . Going ahead with the iteration one gets in  $i$  steps

$$\hat{H}|\phi_i\rangle = b_i|\phi_{i-1}\rangle + a_i|\phi_i\rangle + b_{i+1}|\phi_{i+1}\rangle, \quad 1 \leq i \leq M. \quad (\text{A.26})$$

By stopping the iteration at  $i = M$  and putting the last coefficient  $b_{M+1} = 0$ , the Hamiltonian can be represented in the basis of orthogonal *Lanczos functions*  $|\phi_i\rangle$  as the tridiagonal matrix  $H_M$  with diagonal elements  $a_i$  with  $i = 0 \dots M$ , and off-diagonal ones  $b_i$  with  $i = 1 \dots M$ . Such matrix is easily diagonalized using the standard numerical paraphernalia to obtain approximate eigenvalues  $\epsilon_j$  and the corresponding orthonormal eigenvectors  $|\psi_j\rangle$ ,

$$|\psi_j\rangle = \sum_{i=0}^M v_{ji} |\phi_i\rangle, \quad j = 0 \dots M. \quad (\text{A.27})$$

It is important to realize that  $|\psi_j\rangle$  are in general not exact eigenfunctions of  $\hat{H}$ , but show a remainder

$$\hat{H}|\psi_j\rangle - \epsilon_j|\psi_j\rangle = b_{M+1}v_{jM}|\phi_{M+1}\rangle. \quad (\text{A.28})$$

On the other hand it is evident from the diagonalization of  $H_M$  that the matrix elements

$$\langle\psi_i|\hat{H}|\psi_j\rangle = \epsilon_j\delta_{ij}, \quad i, j = 0 \dots M \quad (\text{A.29})$$

are exact, without restriction to the subspace  $L_M$ . This the crucial identity of the ED procedure.

If in Eq. (A.26)  $b_{M+1} = 0$ , an  $(M + 1)$ -dimensional eigenspace where  $H_M$  is already an exact representation of  $\hat{H}$  has been found. This happens inevitably when  $M = N_{st} - 1$ , where  $N_{st}$  is the space dimension, but for  $M < N_{st} - 1$  it can only occur if the starting vector is orthogonal to some invariant subspace of  $\hat{H}$ . Evidently this should not be the case if the input vector  $|\phi_0\rangle$  is random, without any hidden symmetries.

The number of operations needed to perform  $M$  Lanczos iterations scales as

$MN_{st}$ . Numerically the Lanczos procedure is subject to roundoff errors introduced by the finite-precision arithmetics. Correctional steps then require operations which number in the order of  $M^2N_{st}$ , and can become computationally more demanding than the Lanczos iterations proper, and so the determinant drawback that thwarts its application in large matrices.

By making use of Eq. (A.29), one can construct the fundamental identity:

$$\begin{aligned}
 \langle n | \hat{H}^k \hat{B} \hat{H}^l \hat{A} | n \rangle &= \sum_{i_0=0}^M \dots \sum_{i_k=0}^M \sum_{j_0=0}^M \dots \sum_{j_l=0}^M \langle \phi_0 | \psi_{i_0} \rangle \langle \psi_{i_0} | \hat{H} | \psi_{i_1} \rangle \dots \langle \psi_{i_{k-1}} | \hat{H} | \psi_{i_k} \rangle \\
 &\quad \times \langle \psi_{i_k} | \hat{B} | \tilde{\psi}_{j_l} \rangle \langle \tilde{\psi}_{j_l} | \hat{H} | \tilde{\psi}_{j_{l-1}} \rangle \dots \langle \tilde{\psi}_{j_1} | \hat{H} | \tilde{\psi}_{j_0} \rangle \langle \tilde{\psi}_{j_0} | \hat{A} | \phi_0 \rangle = \\
 &= \sum_{i=0}^M \sum_{j=0}^M \langle \phi_0 | \psi_i \rangle \langle \psi_i | \hat{B} | \tilde{\psi}_j \rangle \langle \tilde{\psi}_j | \hat{A} | \phi_0 \rangle (\epsilon_i)^k (\tilde{\epsilon}_j)^l, \tag{A.30}
 \end{aligned}$$

where  $|n\rangle$  is an arbitrary normalized vector, and  $A, B$  are general operators. To obtain this expression, one performs two Lanczos procedures with  $M = \max(k, l)$  steps. The first one begins with the vector  $|\phi_0\rangle = |n\rangle$  and produces the subspace  $L_M = \{|\phi_j\rangle, j = 0 \dots M\}$  along with approximate eigenvectors  $|\psi_j\rangle$  and eigenvalues  $\epsilon_j$ . The second Lanczos procedure is started with the normalized vector

$$|\tilde{\phi}_0\rangle = A|\phi_0\rangle / \sqrt{\langle \phi_0 | A^\dagger A | \phi_0 \rangle}, \tag{A.31}$$

and results in the subspace  $\tilde{L}_M = \{|\tilde{\phi}_j\rangle, j = 0 \dots M\}$  with approximate  $|\tilde{\psi}_j\rangle$  and  $\tilde{\epsilon}_j$ . To see the derivation in detail, look up the important review in Ref. [150]. So, Eq. (A.30) shows how the matrix element on the left can be written in terms of the Lanczos approximate eigenvectors and eigenvalues alone, and by means of it one can introduce finite temperature in the Lanczos procedure.

The next step is to consider the expectation value of an operator  $\hat{A}$  in the

canonical ensemble

$$\langle \hat{A} \rangle = \sum_{n=1}^{N_{st}} \langle n | e^{-\beta \hat{H}} \hat{A} | n \rangle \bigg/ \sum_{n=1}^{N_{st}} \langle n | e^{-\beta \hat{H}} | n \rangle, \quad (\text{A.32})$$

whereupon one performs the high-temperature expansion of the Boltzmann factor  $e^{-\beta H}$ ,

$$\begin{aligned} \langle \hat{A} \rangle &= Z^{-1} \sum_{n=1}^{N_{st}} \sum_{k=0}^{\infty} \frac{(-\beta)^k}{k!} \langle n | \hat{H}^k \hat{A} | n \rangle, \\ Z &= \sum_{n=1}^{N_{st}} \sum_{k=0}^{\infty} \frac{(-\beta)^k}{k!} \langle n | \hat{H}^k | n \rangle. \end{aligned} \quad (\text{A.33})$$

The terms in the expansion  $\langle n | \hat{H}^k \hat{A} | n \rangle$  can be calculated exactly using the Lanczos procedure with  $M \geq k$  steps and with  $|\phi_0^n\rangle = |n\rangle$  as a starting function, since this is a special case of Eq. (A.30):

$$\langle n | \hat{H}^k \hat{A} | n \rangle = \sum_{i=0}^M \langle n | \psi_i^n \rangle \langle \psi_i^n | \hat{A} | n \rangle (\epsilon_i^n)^k. \quad (\text{A.34})$$

Working with a restricted basis  $k \leq M$ , Eq. (A.34) can be inserted into the sums expressed by Eqs. (A.33), extending them to  $k > M$ , which yields

$$\begin{aligned} \langle \hat{A} \rangle &\approx Z^{-1} \sum_{n=1}^{N_{st}} \sum_{i=0}^M e^{-\beta \epsilon_i^n} \langle n | \psi_i^n \rangle \langle \psi_i^n | \hat{A} | n \rangle, \\ Z &\approx \sum_{n=1}^{N_{st}} \sum_{i=0}^M e^{-\beta \epsilon_i^n} \langle n | \psi_i^n \rangle \langle \psi_i^n | n \rangle, \end{aligned} \quad (\text{A.35})$$

and the error of the approximation is of the order of  $\beta^{M+1}$ . It can be verified that the expectation value so calculated is also valid for  $T \rightarrow 0$  [150].



The computation of static quantities in Eq. (A.35) still involves the summation over the complete set of  $N_{st}$  states  $|n\rangle$ , which is not doable in practice. To obtain a useful method, one further approximation which replaces the full summation by a *partial* one over a much smaller set of random states must be made. One considers the expectation value  $\langle \hat{A} \rangle$  at  $T > 0$ , as defined by Eq. (A.32). Instead of the whole sum, a restricted one over several random vectors  $|r\rangle$ ,  $r = 1 \dots R$ , given by

$$|r\rangle = \sum_{n=1}^{N_{st}} \beta_{rn} |n\rangle, \quad (\text{A.36})$$

where the  $\beta_{rn}$  are assumed to be distributed randomly, is carried out. Therefore in the FTLM, the full summation in Eq. (A.32) is replaced by

$$\langle \hat{A} \rangle = \sum_{r=1}^R \langle r | e^{-\beta \hat{H}} \hat{A} | r \rangle \bigg/ \sum_{r=1}^R \langle r | e^{-\beta \hat{H}} | r \rangle.$$

Such approximation is made analogously to Monte Carlo methods and is of course hard to justify rigorously, although the errors involved can in principle be estimated [150].

So, the fundamental relations required for the implementation of the FTLM for the calculation of static quantities are

$$\begin{aligned} \langle \hat{A} \rangle &\approx \frac{N_{st}}{ZR} \sum_{r=1}^R \sum_{j=0}^M e^{-\beta \epsilon_j^r} \langle r | \psi_j^r \rangle \langle \psi_j^r | \hat{A} | r \rangle, \\ Z &\approx \frac{N_{st}}{R} \sum_{r=1}^R \sum_{j=0}^M e^{-\beta \epsilon_j^r} |\langle r | \psi_j^r \rangle|^2. \end{aligned} \quad (\text{A.37})$$

where the sampling is carried over  $R$  random states  $|r\rangle = |\phi_0^r\rangle$ , which serve as initial

functions for the  $M$ -step Lanczos procedure, and which results in  $M$  approximate eigenvalues  $\epsilon_j^r$  with corresponding eigenvectors  $|\psi_j^r\rangle$ .

In order to reduce computational and storage requirements, taking into account the symmetries of the model Hamiltonian is crucial. One must not forget to "tune up" the method through various tests in order to verify if the results are consistent and satisfactory. The verification of the convergence of results for various system sizes may give a hint at the extent of finite-size effects.

### A.2.2 Adjusting FTLM

In Fig. A.1, we indicate step by step how the FTLM was tuned up. The limit susceptibility was calculated as follows

$$\begin{aligned}\chi &= \frac{\langle (S^z)^2 \rangle}{NT} = \frac{\langle S^2 \rangle}{3NT} \\ \langle S^2 \rangle &\rightarrow \frac{N}{2} \left( \frac{N}{2} + 1 \right) \\ \lim_{T \rightarrow 0} \chi T &\rightarrow \frac{1}{6} \left( \frac{N}{2} + 1 \right) = \frac{5}{3}.\end{aligned}\tag{A.38}$$

We observe that the deviation of the FTLM results from the expected value is very little for  $R > 24000$ . Since the error is increased as  $T \rightarrow 0$ , we expect that the error introduced by the sampling of the Hilbert space is negligible in the temperature range studied in this dissertation. Notice, particularly, that the value of the minimum in  $\chi T$  is free of this type of error for samplings as small as  $R = 10000$ .

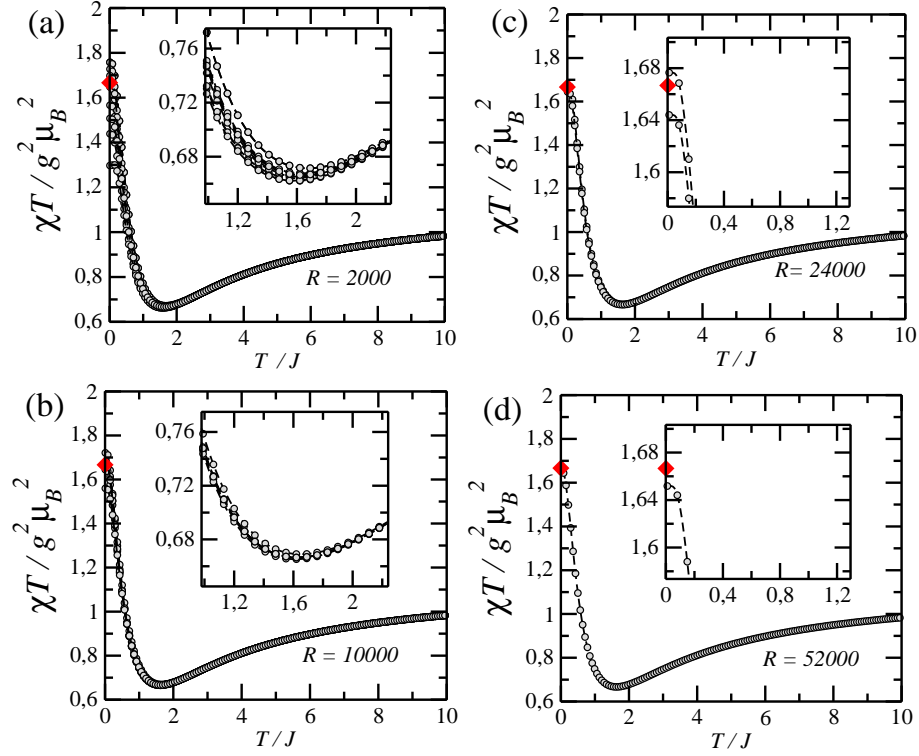


Figure A.1: The behavior of the product of the susceptibility per site  $\chi$  and the temperature  $T$  of the ssS chain with  $N = 18$  and  $J = 1.5J'$ . The number of states  $M$  taken in each random sampling is 50 and the total number of random samples  $R$  is indicated in the figure. Each curve is the result of one running of the FTLM algorithm with the indicated parameters, thus there are 10, 5, 2 and 1 runnings in figures (a), (b), (c) and (d), respectively. The precise value of  $\chi T$  for this system size as  $T \rightarrow 0$ ,  $\lim_{T \rightarrow 0} \chi T = 5/3$ , is indicated by the symbol  $\diamond$ . The inset of (a) and (b) show the region near the minimum of the curve, while the inset of (c) and (d) show the region near  $T = 0$ .

# Bibliography

- [1] D. M. Dennison, Phys. Rev. **28**, 318 (1926).
- [2] R. de L. Kronig and I. Rabi, Phys. Rev. **29**, 262 (1927).
- [3] L. Pauling, Phys. Rev. **36**, 430 (1930).
- [4] V. G. Manzhelii and Yu A. Freiman, *Physics of Cryocrystals* (AIP Press, NY, 1997).
- [5] D. Marx and H. Wiechert, *Adv. Chem. Phys.* **95**, 213 (1996).
- [6] M. N. Müser and J. Ankerhold, Europhys. Lett. **44**, No 2, 216 (1998)
- [7] N. S. Sullivan and K. Kim, J. Low Temp. Phys. **111**, 533 (1998); J. Low Temp. Phys. **113**, 705 (1998).
- [8] Yu. A. Freiman, V. V. Sumarokov, and A. P. Brodyanski, J. Phys.: Condens. Matt. **3**, 3855 (1991).
- [9] A. P. Brodyanski, V. V. Sumarokov, Yu. A. Freiman, and A. Jezowski, Low Temp. Phys. **19**, 368 (1993).

- 
- [10] Yu. A. Freiman, S. M. Tretyak, A. Jezowski, and R. J. Hemley, J. Low Temp. Phys. **113**, 723 (1998); J. Low Temp. Phys. **122**, 537 (2001); J. Low Temp. Phys. **126**, 703 (2002)
- [11] Yu. A. Freiman, S. M. Tretyak, T. N. Antsygina, and R. J. Hemley, J. Low Temp. Phys. **133**, 251 (2003).
- [12] Yu. A. Freiman, S. M. Tretyak, T. N. Antsygina, and R. J. Hemley, J. Low Temp. Phys. **134**, 535 (2004)
- [13] E. Artacho, F. Ynduráin, B. Pajot, R. Ramírez, C. P. Herrero, L. I. Khirunen, K. M. Itoh, and E. E. Haller, Phys. Rev. B **56**, 3820 (1997).
- [14] H. Shima and T. Nakayama, Phys. Rev. B **71**, 155210 (2005).
- [15] H. Shima and T. Nakayama, Physica B **376**, 157 (2006).
- [16] M. Gienger, M. Glaser, and K. Lassmann, Solid State Commun. **86**, 285 (1993).
- [17] W. Wegener, C. Bostoen and G. Coddens, J. Phys. Condens. Matter **2**, 3177 (1990).
- [18] G. J. Kearley, H. G. Büttner, F. Fillaux, and M. F. Lautié, Physica B **226**, 199 (1996).
- [19] P. Vorderwisch, S. Hautecler, G. J. Kearley, and F. Kubanek, Chem. Phys. **261**, 157 (2000).
- [20] W. Press, J. Chem. Phys. **56**, 2597 (1972).
- [21] C. Gutt, B. Asmussen, W. Press, C. Merkl, H. Casalta, J. Greinert, G. Bohrmann, J. S. Tse, and A. Hüller, Europhys. Lett. **48**, 269 (1999).

- 
- [22] O. Rogalsky, P. Vorderwisch, A. Hüller, and S. Hautecler, J. Chem. Phys. **116**, 1063 (2002).
- [23] A. Würger, Phys. Rev. Lett. **88**, 063002 (2002).
- [24] C. Gutt, W. Press, A. Hüller, J. S. Tse, and H. Casalta, J. Chem. Phys. **114**, 4160 (2001).
- [25] S. Szymański, J. Chem. Phys. **111**, 288 (1999).
- [26] T. Ratayczyk and S. Szymanski, J. Chem. Phys. **123**, 204509 (2005); J. Chem. Phys. **127**, 184504 (2007).
- [27] V. M. Rozenbaum and V. M. Ogenko, Sov. Phys. Solid State **30**, 1753 (1988).
- [28] V. M. Rozenbaum, V. M. Ogenko, and A. A. Chuiko, Sov. Phys. Usp **34**, 883 (1991).
- [29] J. K. Gimzewski, C. Joachim, R. R. Schlittler, V. Langlais, H. Tang, and I. Johannsen, Science **281**, 531 (1998).
- [30] N. Koumura, R. W. J. Zijlstra, R. A. van Delden, N. Harada, and B. L. Feringa, Nature **401**, 152 (1999).
- [31] V. Bermudez, N. Capron, T. Gase, F. G. Gatti, F. Kajzar, D. A. Leigh, F. Zerbetto and S. Zhang, Nature **406**, 608 (2000).
- [32] W. R. Browne and B. L. Feringa, Nature Nanotechnology **1**, 25 (2006).
- [33] C. Manzano, W.-H. Soe, H. S. Wong, F. Ample, A. Gourdon, N. Chandrasekhar, and C. Joachim, Nature Materials **8**, 576 (2009)
-

- 
- [34] I. Sh. Averbukh and R. Arvieu, Phys. Rev. Lett. **87**, 163601 (2001).
- [35] C. E. Creffield, G. Hur, and T. S. Monteiro, Phys. Rev. Lett. **96**, 024103 (2006).
- [36] C. E. Creffield, S. Fishman, and T. S. Monteiro, Phys. Rev. E **73**, 066202 (2006).
- [37] M. Lepers, V. Zehnlé, and J. C. Garreau, Phys. Rev. A **77**, 043628 (2008). See references therein.
- [38] A. Romanelli, Phys. Rev. A **80**, 022102 (2009).
- [39] F. L. Moore, J. C. Robinson, C. F. Bharucha, B. Sundaram, and M. G. Raizen, Phys. Rev. Lett. **75**, 4598 (1995).
- [40] S. Schlunk, M. B. D’Arcy, S. A. Gardiner, and G. S. Summy, Phys. Rev. Lett. **90**, 124102 (2003).
- [41] C. Ryu, M. F. Andersen, A. Vaziri, M. B. D’Arcy, J. M. Grossmann, K. Helmer-son, and W. D. Phillips, Phys. Rev. Lett. **96**, 160403 (2006).
- [42] J. F. Kanem, S. Maneshi, M. Partlow, M. Spanner, and A. M. Steinberg, Phys. Rev. Lett. **98**, 083004 (2007).
- [43] S. Sachdev, *Quantum Phase Transitions* (Cambridge University Press, Cambridge-UK, 2001).
- [44] A. Dutta and J. K. Bhattacharjee, Phys. Rev. B **58**, 6378 (1998); A. Dutta and J. K. Bhattacharjee, Phys. Rev. B **64**, 184106 (2001).
- [45] A. Campa, A. Giansanti, D. Mukamel, and S. Ruffo, Physica A **365**, 120 (2006).

- 
- [46] T. Vojta and R. Sknepnek, Phys. Rev. B **74**, 094415 (2006).
- [47] S. Sachdev and T. Senthil, Ann. Phys. **251**, 76 (1996).
- [48] A. Auerbach, *Interacting Electrons and Quantum Magnetism* (Springer-Verlag, New York, 1998).
- [49] C. J. Hamer, J. B. Kogut, and L. Susskind, Phys. Rev. D, **19**, 3091 (1979).
- [50] F. D. M. Haldane, Phys. Lett. A **93**, 464 (1983); F. D. M. Haldane, Phys. Rev. Lett. **50**, 1153 (1983).
- [51] R. Shankar and N. Read, Nucl. Phys. B **336**, 457 (1990).
- [52] T. T. Wu and C. N. Yang, Nucl. Phys. B **107**, 365 (1976).
- [53] A. Imambekov, M. Lukin, and E. Demler, Phys. Rev. Lett. **93**, 120405 (2004).
- [54] T. P. Polak and T. K. Kopeć, Phys. Rev. B **76**, 094503 (2007); T. P. Kopeć, Phys. Rev. B **76**, 054518 (2004)
- [55] F. Alet and E. S. Sorensen, Phys. Rev. E **67**, 015701(R) (2003).
- [56] M. Levin and X.-G. Wen, Phys. Rev. B **73**, 035122 (2006).
- [57] K. Takano, K. Kubo, and H. Sakamoto, J. Phys.: Condens. Matter **8**, 6405 (1996).
- [58] K. Hida, K. Takano, and H. Suzuki, J. Phys. Soc. Jpn. **78**, 084716 (2009).
- [59] R. R. Montenegro-Filho and M. D. Coutinho-Filho, Phys. Rev. B **78**, 014418 (2008).



- 
- [60] H. Niggemann, G. Uimin, and J. Zittartz, J. Phys.: Condens. Matter **9**, 9031 (1997); K. Okamoto, T. Tonegawa, Y. Takahashi, and M. Kaburagi, J. Phys.: Condens. Matter **11**, 10485 (1999); K. Sano and K. Takano, J. Phys. Soc. Jpn. **69**, 2710 (2000); H.-J. Mikeska and C. Luckmann Phys. Rev. B **77**, 054405 (2008); .
- [61] K. Okamoto, T. Tonegawa, and M. Kaburagi, J. Phys.: Condens. Matter **15**, 5979 (2003).
- [62] N. B. Ivanov, J. Richter, and J. Schulenburg, Phys. Rev. B **79**, 104412 (2009).
- [63] C. Lanczos, J. Res. Natl. Bur. Stand. **45**, 255 (1950).
- [64] S. R. White, Phys. Rev. B **48**, 10345 (1993); U. Schollwöck, Rev. Mod. Phys. **77**, 259 (2005).
- [65] H. Kikuchi, Y. Fujii, M. Chiba, S. Mitsudo, T. Idehara, T. Tonegawa, K. Okamoto, T. Sakai, T. Kuwai, and H. Ohta, Phys. Rev. Lett. **94**, 227201 (2005); H. H. Fu, K. L. Yao, and Z. L. Liu, Phys. Rev. B **73**, 104454 (2006); Y.-C. Li, J. Appl. Phys. **102**, 113907 (2007); K. C. Rule, A. U. B. Wolter, S. Süllow, D. A. Tennant, A. Brühl, S. Köhler, B. Wolf, M. Lang, and J. Schreuer, Phys. Rev. Lett. **100**, 117202 (2008); F. Aimo, S. Krämer, M. Klanjšek, M. Horvatić, C. Berthier, and H. Kikuchi, Phys. Rev. Lett. **102**, 127205 (2009).
- [66] M. Matsuda, K. Kakurai, A. A. Belik, M. Azuma, M. Takano, and M. Fujita, Phys. Rev. B **71**, 144411 (2005).
- [67] B. Gu and G. Su, Phys. Rev. B **75**, 174437 (2007).

- 
- [68] Y. Hosokoshi, K. Katoh, Y. Nakazawa, H. Nakano, and K. Inoue, J. Am. Chem. Soc. **123**, 7921 (2001).
- [69] For a review see: M. D. Coutinho-Filho, R. R. Montenegro-Filho, E. P. Raposo, C. Vitoriano, and M. H. Oliveira, J. Braz. Chem. Soc. **19**, 232 (2008).
- [70] A. M. S. Macêdo, M. C. dos Santos, M. D. Coutinho-Filho, and C. A. Macêdo, Phys. Rev. Lett. **74**, 1851 (1995); G.-S. Tian and T.-H. Lin, Phys. Rev. B **53**, 8196 (1996); E. P. Raposo and M. D. Coutinho-Filho, Phys. Rev. Lett. **78**, 4853 (1997); E. P. Raposo and M. D. Coutinho-Filho, Phys. Rev. B **59**, 14384 (1999)..
- [71] G. Sierra, M. A. Martín-Delgado, S. R. White, D. J. Scalapino and J. Dukelsky, Phys. Rev. B **59**, 7973 (1999).
- [72] C. Vitoriano, M. D. Coutinho-Filho, and E. P. Raposo, J. Phys. A: Math. Gen. **35**, 9049 (2002);
- [73] F. C. Alcaraz and A. L. Malvezzi, J. Phys. A: Math. Gen. **30**, 767 (1997); M. A. Martín-Delgado, J. Rodriguez-Laguna, and G. Sierra, Phys. Rev. B **72**, 104435 (2005).
- [74] C. Vitoriano, F. B. de Brito, E. P. Raposo, and M. D. Coutinho-Filho, *Mol. Cryst. Liq. Cryst.* **374**, 185 (2002); S. Yamamoto and J. Ohara, Phys. Rev. B **76**, 014409 (2007).
- [75] R. R. Montenegro-Filho and M. D. Coutinho-Filho, Physica A **357**, 173 (2005).
- [76] M. H. Oliveira, M. D. Coutinho-Filho, and E. P. Raposo, Phys. Rev. B **72**, 214420 (2005).
-

- 
- [77] R. R. Montenegro-Filho and M. D. Coutinho-Filho, Phys. Rev. B **74**, 125117 (2006), and references therein.
- [78] F. A. N. Santos and M. D. Coutinho-Filho, Phys. Rev. E **80**, 031123 (2009).
- [79] M. H. Oliveira, E. P. Raposo, and M. D. Coutinho-Filho, Phys. Rev. B **80**, 205119 (2009).
- [80] H. B. Callen, *Thermodynamics and an Introduction to Thermostatistics* (John Wiley & Sons Inc, New York-NY, 1985); R. P. Feynman, *Statistical Mechanics—A Set of Lectures* (The Benjamin Cummings Publishing Company Inc, Reading-MA, 1972).
- [81] C. S. O. Yokoi, M. D. Coutinho-Filho, and S. R. Salinas, Phys. Rev. B **24**, 4047 (1981).
- [82] *Numerical Recipes Inc: The Art of Scientific Computing* (Cambridge University Press, Cambridge-UK, 1992).
- [83] E. H. Lieb and D. Mattis, J. Math. Phys. **3**, 749 (1962).
- [84] A. Ederlyi (editor), *Higher Transcendental Functions (Bateman Project)* (McGraw-Hill Book Company Inc, New York-NY, 1953).
- [85] J. P. Renard, M. Verdaguer, L. P. Regnault, W. A. C. Erkelens, J. Rossat-Mignot, J. Ribas, W. G. Stirling, and C. Vettier, J. Appl. Phys. **63**, 3538 (1988).
- [86] N. D. Mermin and H. Wagner, Phys. Rev. Lett. **17**, 1133 (1966).

- 
- [87] A. Daoud, A. B. Salah, C. Chappert, J.-P. Renard, A. Cheick-Rouhou, T. Duc, and M. Verdaguer, Phys. Rev. B **33**, 6253 (1986).
- [88] J. S. Miller, J. C. Calabrese, H. Rommelmann, S. R. Chittipeddi, J. H. Zhang, M. R. William, and M. R. Epstein, J. Am. Chem. Soc. **109**, 769 (1987).
- [89] A. Das, G. M. Rosair, M. S. El Fallah, J. Ribas, and S. Mitra, Inorg. Chem. **45**, 3301 (2006).
- [90] M. Tamura, Y. Nakazawa, D. Shiomi, K. Nozawa, Y. Hosokoshi, M. Ishikawa, M. Takahashi, and M. Kinoshita, Chem. Phys. Lett. **186**, 401 (1991); M. Takahashi, P. Turek, Y. Nakasawa, M. Tamura, K. Nozawa, D. Shiomi, M. Ishiwawa, M. Kinoshita, Phys. Rev. Lett. **67**, 746 (1991).
- [91] Y. Pei, O. Kahn, and J. Sletten, J. Am. Chem. Soc. **108**, 3143 (1986).
- [92] O. Kahn, in *Molecular Magnetism*, (Wiley-VCH 1993).
- [93] A. Gleizes and M. Verdaguer, J. Am. Chem. Soc. **103**, 7373 (1981).
- [94] M. Verdaguer, A. Gleizes, J.-P. Renard, and J. Seiden, Phys. Rev. B **29**, 5144 (1984).
- [95] A. Gleizes and M. Verdaguer, J. Am. Chem. Soc. **106**, 3727 (1984).
- [96] A. Mosset, J. Galy, E. Coronado, M. Drillon, and D. Beltran, J. Am. Chem. Soc. **106**, 2864 (1984); E. Coronado, M. Drillon, P. R. Nugteren, L. J. de Jongh, D. Beltran, and R. Georges, J. Am. Chem. Soc. **111**, 3874 (1989).
- [97] Y. Pei, M. Verdaguer, O. Kahn, J. Sletten, and J.-P. Renard, J. Am. Chem. Soc. **108**, 7428 (1986); Y. Pei, O. Kahn, J. Sletten, J.-P. Renard, R. Georges,

- J-C. Gianduzzo, J. Curely, and Q. Xu, *Inorg. Chem.* **27**, 47 (1988); Y. Pei, K. Nakatani, O. Kahn, J. Sletten, and J.-P. Renard, *Inorg. Chem.* **28**, 3170 (1989).
- [98] P.J. van Koningsbruggen, O. Kahn, K. Nakatani, Y. Pei, J-P. Renard, M. Drillon, and P. Legoll, *Inorg. Chem.* **29**, 3325 (1990).
- [99] J. H. Yoon, H. C. Kim, and C. S. Hong, *Inorg. Chem.* **44**, 7714 (2005).
- [100] D. Zhang, H. Wang, Y. Chen, Z.-H. Ni, L. Tian, and J. Jiang, *Inorg. Chem.* **48**, 5488 (2009).
- [101] E. F. Pedroso, C. L. M. Pereira, H. F. dos Santos, L. F. C. de Oliveira, W. C. Nunes, M. Knobel, and H. O. Sumpf, *J. Mag. Mag. Mat.* **320**, e200 (2008).
- [102] O. Khan, E. Bakalbassis, C. Mathonière, M. Hagiwara, K. Katsumata, and L. Ouahab, *Inorg. Chem.* **36**, 1530 (1997).
- [103] J.-P. Costes, G. Novitchi, S. Shova, F. Dahan, B. Donnadieu, and J.-P. Tuchagues, *Inorg. Chem.* **43**, 7792 (2005).
- [104] E. Coronado, J. R. Galán-Mascarós, C. J. Gómez-García, and C. Mastí-Gastaldo, *Inorg. Chem.* **44**, 6197 (2005).
- [105] D. Zhang, H. Wang, L. Tian, H.-Z. Kou, J. Jiang, and Z.-H. Ni, *Chrystal Growth & Design.* **9**, 3989 (2009).
- [106] H. Miyasaka, M. Julve, M. Yamashita, and R. Clérac, *Inorg. Chem.* **48**, 3420 (2009).

- [107] A. Caneschi, D. Gatteschi, J. Laugier and P. Rey, J. Am. Chem. Soc. **109**, 2191 (1987); C. I. Cabello, A. Caneschi, R. L. Carlin, D. Gatteschi, P. Rey, and R. Sessoli, Inorg. Chem. **29**, 2582 (1990).
- [108] A. Caneschi, D. Gatteschi, J.-P. Renard, P. Rey, and R. Sessoli, Inorg. Chem. **28**, 2940 (1989).
- [109] A. Caneschi, D. Gatteschi, P. Rey, R. Sessoli, Inorg. Chem. **27**, 1756 (1988); A. Caneschi, D. Gatteschi, J. P. Renard, P. Rey, and R. Sessoli, Inorg. Chem., **28**, 3314 (1989); A. Caneschi, D. Gatteschi, P. Rey, and R. Sessoli, Inorg. Chem. **30**, 3936 (1991); A. Caneschi, D. Gatteschi, and R. Sessoli, Inorg. Chem. **32**, 4612 (1993).
- [110] A. Caneschi, D. Gatteschi, N. Laloti, R. Sessoli, L. Sorace, V. Tangoulis, and A. Vindigni, Chem. Eur. J. **8**, 286 (2002).
- [111] K. Fegy, D. Luneau, E. Belorizky, M. Novac, J.-L. Tholence, C. Paulsen, T. Ohm, and P. Rey, Inorg. Chem. **37**, 4524 (1998).
- [112] D. Luneau and P. Rey, Coord. Chem. Rev. **249**, 2591 (2005).
- [113] D. Luneau, C. Stroh, J. Cano, and R. Ziessel, Inorg. Chem. **44**, 633 (2005).
- [114] A. Zheludev, V. Barone, M. Bonnet, B. Delley, A. Grand, E. Ressouche, P. Rey, R. Subra, and J. Schweizer, J. Am. Chem. Soc. **116**, 2019 (1994).
- [115] M. Minguet, D. Luneau, E. Lhotel, V. Villar, C. Paulsen, D. B. Amabilino, and J. Veciana, Angew. Chem. Int. Ed. **41**, 586 (2002); M. Minguet, D. Luneau, C. Paulsen, E. Lhotel, A. Gorski, J. Waluk, D. B. Amabilino, and J. Veciana, Polyhedron **22**, 2349 (2003).

- 
- [116] L. R. Walker, R. E. Dietz, K. Andres, and S. Darack, Sol. State. Comm. **11**, 593 (1972).
- [117] C. M. Wynn, M. A. Gîrtu, W. B. Brinckerhoff, K.-I. Sugiura, J. S. Miller, and A. J. Epstein, Chem. Mater. **9**, 2156 (1997).
- [118] S. Ostrovsky, W. Haase, M. Drillon, and P. Panissod, Phys. Rev. B **64**, 134418 (2001).
- [119] A. Morello, F. L. Mettes, F. Luis, J. F. Fernández, J. Krzystek, G. Aromí, G. Christou, and L. J. de Jongh, Phys. Rev. Lett. **90**, 017206 (2003).
- [120] M. Evangelisti, A. Candini, A. Ghirri, M. Affronte, G. W. Powell, I. A. Gass, P. A. Wood, S. Parsons, E. K. Brechin, D. Collison, and S. L. Heath, Phys. Rev. Lett. **97**, 167202 (2006).
- [121] E. Lhotel, V. Simonet, E. Ressouche, B. Canals, D. B. Amabilino, C. Sporer, D. Luneau, J. Veciana, and C. Paulsen, Phys. Rev. B **75**, 104429 (2007).
- [122] E. Belorizky and P. Rey, Mol. Phys. **75**, 563 (1992).
- [123] R. Sessoli, D. Gatteschi, A. Caneschi, and M. A. Novak, Nature **365**, 141 (1993).
- [124] L. Thomas, F. Lioni, R. Ballou, R. Sessoli, D. Gatteschi, and B. Barbara, Nature **383**, 145 (1996).
- [125] E. Lhotel, D. B. Amabilino, C. Sporer, D. Luneau, J. Veciana, and C. Paulsen, Phys. Rev. B **77**, 064416 (2008).
- [126] W. Wernsdorfer and R. Sessoli, Science **284**, 133 (1999).

- 
- [127] R. J. Glauber, J. Math. Phys. **4**, 294 (1963).
- [128] A. Caneschi, D. Gatteschi, N. Lalioti, C. Sangregorio, R. Sessoli, G. Venturi, A. Vindigni, A. Rettori, M. G. Pini, and M. A. Novak, Angew. Chem. Int. Ed. **9**, 40 (2001).
- [129] C. Coulon, R. Clérac, L. Lecren, W. Wernsdorfer, and H. Miyasaka, Phys. Rev. B **69**, 132408 (2004).
- [130] W. Wernsdorfer, R. Clérac, C. Coulon, L. Lecren, and H. Miyasaka, Phys. Rev. Lett. **95**, 237203 (2005).
- [131] N. Ishii, Y. Okamura, S. Chiba, T. Nogami, T. Ishida, J. Am. Chem. Soc. **130**, 24 (2008).
- [132] R. Sessoli, Angew. Chem. Int. Ed. **47**, 5508 (2008).
- [133] M. E. Fisher, Am. J. Phys. **32**, 343 (1964).
- [134] J. C. Bonner and M. E. Fisher, Phys. Rev. A **135**, 640 (1964).
- [135] H. W. BLöte, Physica **79B**, 427 (1975).
- [136] P. W. Anderson, Phys. Rev. **86**, 694 (1952).
- [137] R. Kubo, Phys. Rev. **87**, 568 (1952).
- [138] G. A. Baker, H. E. Gilbert, J. Eve, and G. S. Rushbrooke, Phys. Rev. **164**, 800 (1974).
- [139] J. Kondo and K. Yamaji, Prog. Theor. Phys. Rev. **47**, 807 (1972).
- [140] H. W. BLöte, J. Appl. Phys. **50**, 7401 (1979).



- [141] J. Seiden, J. Phys. **44**, L947 (1983).
- [142] M. Drillon, J. C. Gianduzzo, and E. Coronado, Phys. Lett. Chem. **96A**, 413 (1983); M. Drillon, E. Coronado, R. Georges, J. C. Gianduzzo, and J. Curely, Phys. Rev. B **40**, 10992 (1989).
- [143] S. Pati, S. Ramasesha, and D. Sen, Phys. Rev. B **55**, 8894 (1997).
- [144] S. Pati, S. Ramasesha, and D. Sen, J. Phys.: Condens. Matter **9**, 8707 (1997).
- [145] S. Yamamoto, S. Brehmer, and H.-J. Mikeska, Phys. Rev. B **57**, 13610 (1998); S. Yamamoto, T. Fukui, and T. Sakai, and H.-J. Mikeska, Eur. Phys. J. B **15**, 211 (2000).
- [146] S. Yamamoto, Phys. Rev. B **59**, 1024 (1999).
- [147] M. Takahashi, Phys. Rev. Lett. **58**, 168 (1987).
- [148] M. Takahashi, Phys. Rev. B **40**, 2494 (1989).
- [149] S. Yamamoto and T. Fukui, Phys. Rev. B **57**, R14008 (1998). An attempt to include spin-wave interactions has been made by S. Yamamoto, T. Fukui, K. Maisinger, and U. Schollwöck, J. Phys.: Condens. Matter **10**, 11033 (1998).
- [150] J. Jaklič, P. Prelovšek, Phys. Rev. B **49**, R50065 (1994); J. Jaklič, P. Prelovšek, Adv. Phys., **49**, 1 (2000).
- [151] T. Nakanishi and S. Yamamoto, Phys. Rev. B **65**, 214418 (2002).
- [152] S. A. Salinas, *Introdução à Física Estatística* (Edusp - Editora da Universidade de São Paulo, São Paulo (SP), 1999).

- 
- [153] H. Bethe, Z. Phys. **71**, 205 (1931).
- [154] M. Takahashi, Prog. Theor. Phys. **46**, 401 (1971).
- [155] A. S. F. Tenório, R. R. Montenegro-Filho, and M. D. Coutinho-Filho, Phys. Rev. B **80**, 054409 (2009).